Revised Version

Eur. Phys. J. direct C5 (1999) 1-65
DESY 97-138

Inclusive Single- and Dijet Rates in Next-to-Leading Order QCD for $\gamma^* p$ and $\gamma^*\gamma$ Collisions

B. Pötter

II. Institut für Theoretische Physik,* Universität Hamburg, Luruper Chaussee 149, D-22761 Hamburg, Germany; e-mail: poetter@mppmu.mpg.de

Abstract. We present one- and two-jet inclusive cross sections for $\gamma^*\gamma$ scattering and virtual photoproduction in ep collisions. The hard cross sections are calculated in next-to-leading order QCD. Soft and collinear singularities are extracted using the phase-space-slicing method. The initial state singularity of the virtual photon depends logarithmically its' virtuality. This logarithm is large and has to be absorbed into the parton distribution function of the virtual photon. We define for this purpose an $\overline{\rm MS}$ factorization scheme similar to the real photon case. We numerically study the dependence of the inclusive cross sections on the transverse energies and rapidities of the outgoing jets and on the photon virtuality. The ratio of the resolved to the direct cross section in ep collisions is compared to ZEUS data.

PACS: 12.38.Bx, 12.38.-t, 13.87.-9, 14.70.Bh

1 Introduction

The topic of this work is the structure of the virtual photon as it can be determined in jet production in high energy collisions. In particular, we will study electron proton scattering as is explored at HERA and the scattering of virtual on real photons as is possible at e^+e^- colliders.

In the parton model [1] a hadron is thought to consist of point-like particles that can be identified mainly with the valence quarks. The valence quarks are surrounded by a sea of virtual quarks and are bound by gluons. These particles obey the laws of Quantum Chromodynamics (QCD) which is a non-abelian SU(3) gauge theory [2]. Hadrons are usually probed in high energy scattering experiments. These experiments involve contributions from a wide range of scales. An important property of QCD is its asymptotic freedom [3], which states that the coupling between quarks and gluons vanishes for asymptotically small distances. Factorization theorems allow a separation of the short and the long distance contributions of the high energy scattering (for reviews on this subject see [4, 5]). This permits the application of perturbative QCD to calculate the hard part of the cross section. The contributions from long distances are parametrized by the parton distribution functions (PDF's).

*Supported by Bundesministerium für Forschung und Technologie, Bonn, Germany, under Contract 05 7 HH 92P (0), and by EEC Program *Human Capital and Mobility* through Network *Physics at High Energy Colliders* under Contract CHRX–CT93–0357 (DG12 COMA).

At the HERA collider at DESY, the scattering of leptons on protons produces jets with large transverse energies E_T. The ZEUS and H1 collaborations have observed an important fraction of events at small virtualities $P^2 \simeq 0$ of the exchanged photon [6, 7]. The lepton is only weakly deflected in these so-called photoproduction events, so that it escapes unobserved in the beam direction. The momentum spread and the slight off-shellness of the photons that are radiated by the lepton, is described by the Weizsäcker-Williams formula [8], where the photons are assumed to be real ($P^2 = 0$). The exchange of the other electroweak gauge boson, Z^0, is largely suppressed for photoproduction and can be neglected. The transverse energy E_T serves as the large scale in photoproduction, which allows a perturbative calculation of the hard part of the scattering. In leading order (LO) two different processes can be identified in the hard cross section. In the *direct* interaction, the photon couples as a point-like particle to the partons from the proton, leading to the Compton scattering and the photon-gluon fusion subprocesses. In the *resolved* interaction, the photon acts as a source of partons, which can interact with the partons from the proton. The resolved photon is described by the photon PDF. For quasi-real photons with virtuality $P^2 \simeq 0$ the parton content is constrained reasonably well by data from deep-inelastic $\gamma^*\gamma$ scattering [9, 10]. Both LO processes produce two outgoing jets with large E_T. Studies of photoproduction events with two jets in the final state at HERA have shown that both, the direct and the resolved processes are present for photons with very small virtuality $P^2 \simeq 0$ [6, 7]. Comparisons between theoretical predictions for dijet photoproduction rates and the data from [6, 7] have been done in [11, 12, 13].

For the comparison between the data on jet cross sections and the theoretical predictions in [11, 12, 13], the hard part of the scattering has been calculated in next-to-leading order (NLO) QCD. In NLO, one encounters inital and final state singularities, due to collinear and soft radiation of partons in the initial or final state. There are two reasons for performing NLO calculations, which are far more cumbersome than the LO ones. First, one wishes to reduce the unphysical scale dependences. Second, only in NLO can one sensibly implement a jet algorithm, which is needed for a comparison between theory and experiment. However, the above discussed distinction between direct and resolved photoproduction becomes ambiguous in NLO. When two-jet events are observed in an experiment, a disposition of energy near the beam pipe of the detector in the forward region of the photon can be attributed either to the photon remnant of a resolved photon or to a collinear final state particle from the direct interaction. The collinear particle in the NLO direct cross section produces a large contribution that has to be subtracted and combined with the LO resolved term. This introduces a dependence of the photon PDF on the factorization scale M_γ. The factorization scale determines the part of the NLO direct contribution, which has to be absorbed into the resolved contribution. The M_γ dependences of the remaining NLO direct and the LO resolved contribution coming from the photon PDF cancel to a large extent. This cancellation has been demonstrated and analyzed numerically in [13, 14, 15] for real photoproduction (see [16] for related work).

Information complementary to the ep collision experiments from HERA can

be obtained from e^+e^- colliders. Assuming the two leptons to emit quasi-real photons that are both described by the Weizsäcker-Williams approximation, one effectively has $\gamma\gamma$ scattering. Both photons can be point-like or act as a source of partons. Three cases can be distinguished, according to the different contributions to the cross section [17]. The interaction of a direct with a resolved photon is denoted as the single resolved (SR) contribution. Interactions, where both photons are resolved are called double-resolved (DR) contributions. These two cases are also encountered in ep scattering, where the one resolved photon has to be substituted by the proton. In addition to these possibilities, also both photons can interact directly in $\gamma\gamma$ scattering, which gives the direct (D) contribution. The region of high center of mass energies is of special interest for obtaining information beyond the low E_T region that is determined by soft physics. This has been measured at LEP [18] and TRISTAN [19]. Comparison of the data in [19] with theoretical predictions using similar methods as those employed in [14] can be found in [13, 20, 21] for real photons.

Recently, data has been presented by the ZEUS [23] and the H1 [24] collaborations for electron-proton collisions involving photons with small, but not-vanishing P^2 that allow a test of the virtual photon structure. So far, there has only been one measurement of the virtual photon structure function from the PLUTO collaboration at the PETRA e^+e^- collider [25]. In [26] we made a comparison of theoretical NLO predictions for γ^*p inclusive jet production with data from [23], by extending the methods used in [11, 12]. This extension will be described in detail in this work. Some theoretical studies of inclusive γ^*p cross sections in LO have been presented in [27, 28, 29]. We also include the case of $\gamma^*\gamma$ scattering that will become important at LEP2 [30], which is an extension of the work from [20, 21].

Since the partonic subprocesses of ep and $\gamma^*\gamma$ scattering are very similar, we will take over the notation 'SR' and 'DR' from the $\gamma\gamma$ case to ep scattering to simplify the discussion. In ep scattering, the SR component denotes the contribution, where the virtual photon is directly interacting with the partons from the proton, whereas in the DR component the resolved photon interacts with the partons from the proton.

The extension from real to virtual photoproduction is done by taking the Weizsäcker-Williams formula to describe the momentum spread of the virtual photon, but keeping P^2 fixed, not integrating over the region of small P^2 and not assuming $P^2 = 0$. This is described by the unintegrated Weizsäcker-Williams formula. In the hard process, the matrix elements for finite P^2 have to be taken. The matrix elements and the initial and final state singularities for the SR contribution with $P^2 \neq 0$ have been calculated in [31, 32] in connection with deep-inelastic ep scattering (DIS) at HERA, where P^2 is large. Since we consider P^2 to be finite, the photon initial state singularities encountered in real photoproduction do not occur. Instead, when integrating over the phase-space of the final state particles, a logarithm of the type $\ln(P^2/E_T^2)$ occurs. In DIS this logarithm is small, since P^2 is of the order of E_T^2, and thus has not to be considered separately. In virtual photoproduction though, P^2 is small and the logarithm gives a large contribution. This large term has to be subtracted from the SR hard cross section, where the virtual photon is direct, and combined with the resolved

virtual photon from the DR contribution. This introduces a dependence of the virtual photon PDF on the factorization scale M_γ, just as in the case of real photons. The cancellation of the M_γ scale dependences of the NLO direct and resolved contributions must hold also for virtual photoproduction with $P^2 \neq 0$. This has been worked out in [26] and will be studied numerically in this work.

The D contribution is needed for the direct interaction of one real and one virtual photon in $\gamma^*\gamma$ reactions. The initial and final state corrections for the D contribution are calculated here for the first time. For the real photon, the singularities are handled as discussed in [13, 21]. For the virtual photon, the procedure is equivalent to the one described for the SR contribution in ep scattering.

The theoretical calculation of the resolved cross sections requires the parton distribution functions of real and virtual photons. Several parametrizations of the parton contents of the real photon are available in the literature by now [33, 34, 35] and seem to be consistent with dijet production data in ep scattering [13, 14]. For virtual photons theoretical models have been constructed that describe the evolution with the scale Q^2 of the parton distributions and the input distributions at scale Q_0 with changing P^2 [27, 36, 37]. However, these virtual photon PDF's are not available in a form that parametrizes the Q^2 evolution in NLO. Only the LO parametrizations for the virtual photon are given in [36, 37].

The outline of this work is as follows. In section 2 we will discuss the general structure of factorization and renormalization for NLO corrections. Section 3 contains a calculation of the LO and NLO partonic cross sections for the D, SR, and DR contributions with a virtual photon. We recall the virtual corrections to the Born cross sections and present the inital and final state singularities, using the phase-space-slicing method. The DR contribution has been calculated in [13] and will be considered only briefly. The parton distribution function of the virtual photon is discussed in section 4. Section 5 contains numerical results for inclusive single- and dijet production in ep scattering. Several numerical tests will be presented and the available data is compared with our theoretical predictions. Section 6 gives theoretical results for $\gamma^*\gamma$ collisions with the kinematics of LEP2. Finally we present a summary and an outlook in section 7. The appendix contains the analytic results for virtual, initial, and final state corrections.

2 General Structure of the Hadronic Cross Sections

The key to using perturbative QCD is the idea of factorization. It states that a cross section is a convolution of different factors that each depend only on physics relevant at one momentum scale. In this section we explain how factorization shows up in the hadronic cross sections we use in this work. Especially we will discuss the divergences appearing in a NLO calculation of the perturbative hard cross section and explain how these divergences are factorized and absorbed by a redefinition of the PDF's involved in each process. The general procedure described in this section will be applied to the specific partonic NLO cross sections that are calculated in section 3.

2.1 Factorization of Hard and Soft Regions

The physical cross sections considered in this work have a general structure, where the long-distance and short-distance parts are separated. The hadronic cross section $d\sigma^H$ of a process is given by a convolution of the hard cross section $d\sigma_{ab}$ and the PDF's $f_{a/A}(x_a)$ and $f_{b/B}(x_b)$:

$$d\sigma^H = \sum_{a,b} \int dx_a dx_b f_{a/A}(x_a) d\sigma_{ab} f_{b/B}(x_b) \quad . \tag{1}$$

In general, the PDF $f_{i/A}(x)$ of a hadron A gives the probability of finding a parton i (quark or gluon) with momentumfraction x within the hadron. It cannot be calculated perturbatively and has to be fixed by measurement. The partons from the PDF are thought to interact in a hard process involving a large scale that allows to make use of the asymptotic freedom of QCD [3], i.e. the vanishing of the coupling between the partons for asymptotically small distances. For a large scale μ, the QCD coupling constant $g(\mu)$ behaves as $g(\mu) \sim 1/\ln(\mu/\Lambda_{QCD})$ and a perturbative expansion of the hard cross section in the strong coupling constant can be applied. The hard process in (1) is described by the *partonic* cross section

$$d\sigma_{ab} = \frac{1}{2x_a x_b s} |\mathcal{M}_{ab}|^2 d\mathrm{PS}^{(n)} \quad , \tag{2}$$

where $2x_a x_b s$ is the flux factor, $|\mathcal{M}_{ab}|^2$ are the partonic matrix elements and $d\mathrm{PS}^{(n)}$ represents the phase space of the n final state particles of the subprocess. In the final state we are interested in jets for which suitable jet definitions have to be defined in order to go from the partonic level to observable quantities. We will come back to this in section 5. The general structure of the cross sections discussed in this work is indicated in Fig. 1. For the case of ep scattering, A

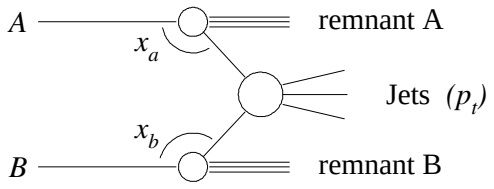

Fig. 1. Factorization of hard and soft processes in the hadronic cross section.

will be a lepton, that radiates a virtual photon and B will be a proton. The remnant A will stem from the resolved virtual photon, whereas the remnant B comes from the proton. In the case of $\gamma^*\gamma$ scattering, A is a virtual and B a real photon. They can both have a hadronic structure, leading to the remnants A and B. The different subprocesses, encountered in these two cases are explained in section 3.

2.2 NLO Corrections

The matrix elements of the partonic cross section (2) can be calculated by summing up all Feynman diagrams to a given order. We will be interested in processes with two initial and at least two final state particles. The calculation of the LO contributions is straightforward. In NLO several difficulties are encountered. We have to distinguish the virtual corrections to the $2 \to 2$ partonic processes, which contain self energy and vertex corrections, and the real corrections, which stem from the radiation of an additional real parton from the $2 \to 2$ processes, leading to $2 \to 3$ processes. Both these contributions contain characteristic divergences.

As an example for a $2 \to 3$ process the Feynman diagrams for the amplitudes of the Born subprocess $q\bar{q} \to q\bar{q}$ and the $\mathcal{O}(\alpha_s)$ correction containing a real gluon emission are drawn in Fig. 2. We consider a parton with momentum p_a emitted

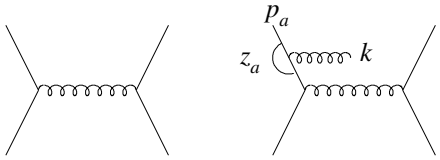

Fig. 2. Partonic cross section: Born graph and real gluon emission.

from a resolved photon. Taking k to be the momentum of the outgoing gluon, the Feynman diagram contains a propagator of the form

$$G \sim \frac{1}{(p_a - k)^2} \equiv \frac{1}{M^2} \quad . \tag{3}$$

In the limit of massless quarks, the propagator diverges in certain regions of phase space. The denominator

$$M^2 = (p_a - k)^2 = -2p_a k = -2|p_a||k|(1 - \cos\theta) \quad , \tag{4}$$

where θ is the angle between the gluon and the parton, vanishes if $\cos\theta = 1$ (*collinear* divergence) and if $|k| = 0$ (*soft* divergence). Both, the collinear and soft divergences are infra-red (IR) divergences that can be regularized in the dimensional regularization scheme [38, 39]. In this scheme $n = 4 - 2\epsilon$ dimensions are chosen for the phase space integration, so that the singularities appear in poles like $1/\epsilon$ and $1/\epsilon^2$. After the poles have been removed the limit $\epsilon \to 0$ is taken and the four-dimensional result is obtained. The singularity shown in Fig. 2 is due to the radiation of a gluon in the initial state and is thus called an *initial state singularity*. In addition to these, *final state singularities* occur, when a parton is collinear or soft in the final state.

The virtual corrections involve loop integrals over internal momenta, that lead to ultra-violet (UV) and IR divergences. These divergences can be extracted, as the real corrections, in the dimensional regularization scheme as poles in $1/\epsilon$ and $1/\epsilon^2$. The UV divergences are removed completely by adding a counter term to the QCD Lagrangian, where the singularities are absorbed by a renormalization of the quark charge, quark field, and gluon field.

When the virtual and the real contributions are added, the IR divergences cancel partly, leaving only initial state singularities. It can be proven that in the remaining hard cross section the short distance finite parts and the long distance singular parts factorize [4, 5]. One defines a bare partonic cross section $d\sigma$, that is calculable in perturbative QCD, a renormalized finite partonic cross section $d\bar{\sigma}$ and transition functions $\Gamma_{i\leftarrow j}$ so that [40]

$$d\sigma_{ij}(s) = \sum_{k,l} \int dz_a dz_b \Gamma_{i\leftarrow k}(z_a, \mu_A) d\bar{\sigma}_{kl}(z_a z_b s, \mu_A, \mu_B) \Gamma_{j\leftarrow l}(z_b, \mu_B) \quad . \tag{5}$$

The variables $z_a, z_b \in [0,1]$ give the momentum fraction of p_a, p_b in the propagator after a parton is radiated as can be seen in Fig. 2. The singular terms are absorbed into the transition functions in such a way that the renormalized cross section is finite. This absorption depends on the scales μ_A and μ_B, which are the factorization scales for the hadrons A and B, respectively. To obtain a hadronic cross section, which is free of divergent parts, one needs renormalized PDF's $\bar{f}$, which are defined as

$$\begin{aligned} \bar{f}_{iA}(\eta_a, \mu_A) &\equiv \int_0^1 \int_0^1 dx dz f_{jA}(x) \Gamma_{i\leftarrow j}(z_a, \mu_A) \delta(\eta_a - x_a z_a) \\ &= \int_{\eta_a}^1 \frac{dz_a}{z_a} \, f_{jA}\left(\frac{\eta_a}{z_a}\right) \Gamma_{i\leftarrow j}(z_a, \mu_A) \quad . \end{aligned} \tag{6}$$

As one sees, the factorization scale dependence of the transition functions leads to a scale dependence of the renormalized PDF's. The factorization of the hard and soft parts in the partonic cross section is pictured in Fig. 3 for the case of a resolved photon with the subprocess depicted in Fig. 2. The factorization

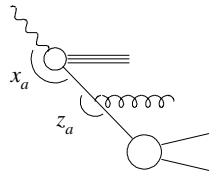

Fig. 3. The factorization theorem for the singular part of the partonic cross section.

scales μ_A and μ_B define what is to be understood as the hard and the soft part of the cross section. Referring to equation (3), M^2 gives the off-shellness of the propagator in the initial state of the partonic cross section. Interactions with $M^2 < \mu_A$ are described with help of the PDF of hadron A, whereas for $M^2 \geq \mu_F$ one can apply perturbative QCD and calculate the partonic cross section.

Using the definitions of the renormalized quantities, the IR safe hadronic cross section reads

$$d\sigma^H(s) = \sum_{k,l} \int d\eta_a d\eta_b \bar{f}_{kA}(\eta_a, \mu_A) d\bar{\sigma}_{kl}(\eta_a \eta_b s, \mu_A, \mu_B) \bar{f}_{lB}(\eta_b, \mu_B) \quad , \tag{7}$$

where the variables $\eta_a, \eta_b \in [0,1]$ are defined as $\eta_a = x_a z_a$ and $\eta_b = x_b z_b$. The connection between the IR safe and the bare hadronic cross sections can be easily seen, by inserting the definition of the renormalized PDF's (6) into (7) and performing the integrations over the delta functions, making use of the definition (5). The factorization scale dependences of the renormalized partonic cross section and the PDF's cancel to a large extend. The transition functions that connect the renormalized partonic cross section and the PDF are, however, not unique in NLO and arbitrary finite parts can be shifted from the PDF's to the renormalized partonic cross section. Therefore one has to define a factorization scheme to be used for a consistent calculation. Commonly used schemes are the DIS [41] and the $\overline{\text{MS}}$ [42] schemes.

To extract the renormalized from the unrenormalized quantities, one assumes $d\bar{\sigma}, d\sigma$ and the transition functions to have perturbative expansions in α_s [40]:

$$d\bar{\sigma}(s) = \sum_n^\infty \left(\frac{\alpha_s}{2\pi}\right)^n d\bar{\sigma}^{(n)}(s) \tag{8}$$

$$d\sigma(s) = \sum_n^\infty \left(\frac{\alpha_s}{2\pi}\right)^n d\sigma^{(n)}(s) \tag{9}$$

$$\Gamma_{i\leftarrow k}(z) = \delta_{ik}\delta(1-z) + \sum_{n=1}^\infty \left(\frac{\alpha_s}{2\pi}\right)^n \Gamma^{(n)}_{i\leftarrow k}(z) \tag{10}$$

The LO contributions are understood to be the $n = 0$th order contributions. For the DR partonic cross section it is of order $\mathcal{O}(\alpha_s^2)$, for the SR contribution is of order $\mathcal{O}(\alpha\alpha_s)$ and for the D contribution it is of order $\mathcal{O}(\alpha^2)$. Inserting the expansions (8)–(10) into (5) gives up to $\mathcal{O}(\alpha_s)$

$$\begin{aligned} d\sigma^{(0)}_{ij}(s) + \frac{\alpha_s}{2\pi} d\sigma^{(1)}_{ij}(s) &= d\bar{\sigma}^{(0)}_{ij}(s) + \frac{\alpha_s}{2\pi}\Bigg[d\bar{\sigma}^{(1)}_{ij}(s,\mu_A,\mu_B) \\ &+ \sum_k \int dz_1\ \Gamma^{(1)}_{i\leftarrow k}(z_1,\mu_A) d\bar{\sigma}^{(0)}_{kj}(z_1 s) \\ &+ \sum_k \int dz_2\ d\bar{\sigma}^{(0)}_{ik}(z_2 s)\Gamma^{(1)}_{k\leftarrow j}(z_2,\mu_B)\Bigg] \quad . \end{aligned} \tag{11}$$

Comparing the left hand and the right hand side in LO gives $d\bar{\sigma}^{(0)} = d\sigma^{(0)}$. The NLO correction is obtained by comparing the left hand and right hand side to order α_s and rearranging the terms:

$$d\bar{\sigma}^{(1)}_{ij} = d\sigma^{(1)}_{ij} - \sum_k \int dz_1 \Gamma^{(1)}_{i\leftarrow k} d\sigma^{(0)}_{kj} - \sum_k \int dz_2 \Gamma^{(1)}_{i\leftarrow k} d\sigma^{(0)}_{kj} \quad . \tag{12}$$

Thus the prescription for subtracting the singular parts from the bare cross section is simple: the singularities are removed by a convolution of the finite Born cross section with the singular $\mathcal{O}(\alpha_s)$ transition functions.

As we have seen, the PDF's acquire a dependence on the factorization scales. The evolution of the PDF's with the scale are predicted in perturbative QCD

by the DGLAP evolution equations [43, 44, 45]. This is the following set of integro-differential equations:

$$\frac{df_i(x,Q^2)}{d\ln Q^2} = \sum_i \int_x^1 \frac{dz}{z} P_{i\leftarrow j}(z,\alpha_s(Q^2)) f_j\left(\frac{x}{z},Q^2\right) \quad . \tag{13}$$

Here, Q^2 is a general scale, and $P_{ij}(z)$ are the splitting functions that represent a process in which a parton with momentum fraction x radiates a parton with momentum fraction $(1-z)x$ and continues with momentum fraction xz. The splitting functions can be expanded in powers of the strong coupling constant with $\alpha_s \equiv g^2/4\pi$:

$$P_{i\leftarrow j}(z,\alpha_s) = \frac{\alpha_s}{2\pi} P^{(0)}_{i\leftarrow j}(z) + \left(\frac{\alpha_s}{2\pi}\right)^2 P^{(1)}_{i\leftarrow j}(z) + \ldots \tag{14}$$

The evolution equations (13) predict the PDF's at a higher scale once they are fixed at some input scale Q_0^2.

2.3 Factorization for the Photon

In the previous section we have described, how the absorption of the singularities works in the case, when A and B are hadrons or resolved photons. For the direct photon one additional complication has to be taken into account.

As mentioned in the introduction, in LO the photon gives rise to direct and resolved contributions in the hadronic cross section. In NLO, the creation of a collinear $q\bar{q}$-pair in the initial state leads to initial state singularities in the direct contribution. The only place for these singularities to be absorbed is the PDF of the resolved photon. This leads to a point-like term in evolution equations of the the photon PDF [46, 47]. A subtraction procedure for the real photon that is consistent with the evolution of the photon PDF has been worked out in [48].

For the virtual photon, one actually has no real singularity, since the virtuality P^2 regularizes the divergence. Integrating over the phase space of the $q\bar{q}$-pair in the initial state leads to a logarithmic dependence on P^2, namely $\ln(P^2/Q^2)$, where Q^2 is the hard scale of the process. This logarithm becomes large for $P^2 \ll Q^2$ and is absorbed into the PDF in much the same way as described in [48]. This leads to an inhomogeneous term in the PDF of the virtual photon, which differs somewhat from the point-like term in the case of the real photon. This will be described in more detail in section 4, where the construction of the virtual photon PDF is explained.

3 Partonic Cross Sections

In this more technical section, we proceed with a computation of the perturbatively calculable partonic cross sections. The partonic cross sections contributing to ep and $\gamma^*\gamma$ scattering are very similar and will therefore be treated together in this section. Both hadronic cross sections contain single resolved (SR) contributions, in which the virtual photon couples directly to the subprocess and

double resolved (DR) contributions, in which the virtual photon is resolved. In ep scattering the virtual photon and its partonic content interact with the partons of the proton, whereas in $\gamma^*\gamma$ scattering they interact with the parton content of the real photon. In addition to the SR and DR contribution, in $\gamma^*\gamma$ scattering one encounters the direct (D) interaction of both photons.

After an introduction to the notation of the various relevant subprocesses, we give the formulæ for the Born and virtual contributions. Then we explain the phase-space slicing method as a tool to separate singular regions of phase space in the partonic cross section, so that we can calculate the singular parts of the real final and initial state corrections. The results from [31] for the SR contributions are recalled for completeness and consistency. The DR contributions can be found in [13] and will be considered only briefly.

3.1 Notation

For the calculation of hadronic cross sections in sections 5 and 6, we will have to calculate the matrix elements for the various partonic cross sections in LO and in NLO. In LO the D contribution is of $\mathcal{O}(\alpha^2)$, the SR contribution is of $\mathcal{O}(\alpha\alpha_s)$ and the DR contribution is of $\mathcal{O}(\alpha_s^2)$. In NLO the D, SR and DR contributions are of one order higher in α_s. Since the partonic cross sections have to be convoluted with the PDF's of the photon, which are of order α/α_s in the high energy limit [46], the different contributions will turn out to be of the same order. The matrix elements $|\mathcal{M}|^2$ from equation (2) are obtained by taking the trace of the hadron tensor that corresponds to each subprocess. We define $H \equiv -g_{\mu\nu}H^{\mu\nu}$. The Born contributions are labeled H_B, the virtual corrections are H_V, and the real corrections are H_R.

First, we have collected the definition of the LO Born matrix elements in Tab. 1. The matrix elements for incoming anti-quarks are the same as those for quarks and only give a factor 2 in the sum over all contributions in the hadronic cross section. This holds also for the contributions in the other tables. Of special interest in this work will be the NLO corrections to the Born matrix elements for processes involving a virtual photon. These are the D and SR contributions, that are collected in Tab. 2. The SR contributions with one virtual photon have been

Table 1. Definition of the LO matrix elements.

D and SR Processes	DR Contributions	
$B_1 = H_B(\gamma^*\gamma \to q\bar{q})$	$B_4 = H_B(qq' \to qq')$	$B_9 = H_B(q\bar{q} \to gg)$
$B_2 = H_B(\gamma^* q \to qg)$	$B_5 = H_B(q\bar{q}' \to q\bar{q}')$	$B_{10} = H_B(qg \to qg)$
$B_3 = H_B(\gamma^* g \to q\bar{q})$	$B_6 = H_B(qq \to qq)$	$B_{11} = H_B(gg \to q\bar{q})$
	$B_7 = H_B(q\bar{q} \to q'\bar{q}')$	$B_{12} = H_B(gg \to gg)$
	$B_8 = H_B(q\bar{q} \to q\bar{q})$	

Table 2. Definition of the NLO matrix elements for the D and SR processes.

Virtual Corrections $2 \to 2$	Real Corrections $2 \to 3$	
$V_1 = H_V(\gamma^*\gamma \to q\bar{q})$	$H_1 = H_R(\gamma^*\gamma \to q\bar{q}g)$	$H_4 = H_R(\gamma^* q \to qq\bar{q})$
$V_2 = H_V(\gamma^* q \to qg)$	$H_2 = H_R(\gamma^* q \to qgg)$	$H_5 = H_R(\gamma^* g \to q\bar{q}g)$
$V_3 = H_V(\gamma^* g \to q\bar{q})$	$H_3 = H_R(\gamma^* q \to qq'\bar{q}')$	

Table 3. Definition of the NLO matrix elements for the DR contribution.

Virtual Corrections $2 \to 2$	Real Corrections $2 \to 3$	
$V_4 = H_V(qq' \to qq')$	$H_6 = H_R(qq' \to qq'g)$	$H_7 = H_R(q\bar{q}' \to q\bar{q}'g)$
$V_5 = H_V(q\bar{q}' \to q\bar{q}')$	$H_8 = H_R(qq \to qqg)$	$H_9 = H_R(q\bar{q} \to q'\bar{q}'g)$
$V_6 = H_V(qq \to qq)$	$H_{10} = H_R(q\bar{q} \to q\bar{q}g)$	$H_{11} = H_R(qg \to qq'\bar{q}')$
$V_7 = H_V(q\bar{q} \to q'\bar{q}')$	$H_{12} = H_R(qg \to qq\bar{q})$	$H_{13} = H_R(q\bar{q} \to ggg)$
$V_8 = H_V(q\bar{q} \to q\bar{q})$	$H_{14} = H_R(qg \to qgg)$	$H_{15} = H_R(gg \to q\bar{q}g)$
$V_9 = H_V(q\bar{q} \to gg)$	$H_{16} = H_R(gg \to ggg)$	
$V_{10} = H_V(qg \to qg)$		
$V_{11} = H_V(gg \to q\bar{q})$		
$V_{12} = H_V(gg \to gg)$		

studied by several authors [31, 32], the D and SR contributions for real photons can be found in [13], whereas the D contributions with one virtual photon have only been studied in this work, yet.

Because of their importance, we show in Fig. 4 the classes of matrix elements as collected in Tab. 2 explicitly. We also show the definition of the momenta which will be used throughout this work for all three, i.e. D, SR and DR, contributions. In Tab. 3 the matrix elements of the NLO processes for the DR case are collected. These matrix elements have been calculated in [49] and the integrations over the singular regions of phase space where performed in [13].

3.2 The Two-Body Processes

For the $2 \to 2$ processes we use the Mandelstam variables

$$s \;=\; (p_a + p_b)^2 = (p_1 + p_2)^2 \quad ,$$

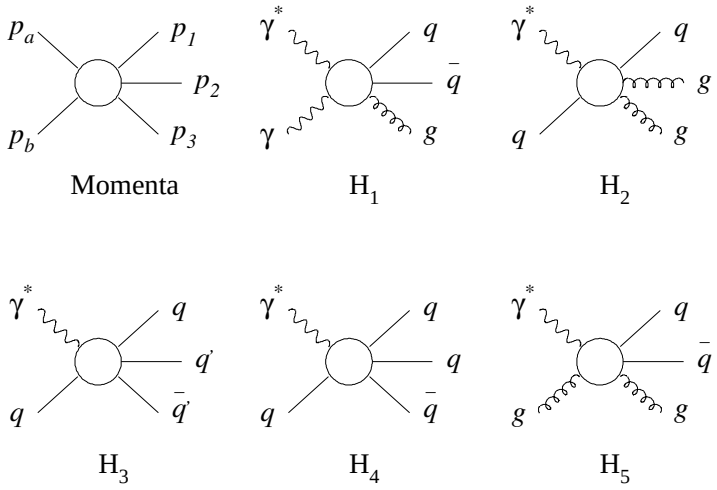

Fig. 4. Notation of the different processes involving one virtual photon.

$$\begin{aligned} t &= (p_a - p_1)^2 = (p_b - p_2)^2 \quad , \\ u &= (p_a - p_2)^2 = (p_b - p_1)^2 \quad . \end{aligned} \tag{15}$$

Note, that in the D and SR case, $p_a = q$ with $P^2 \equiv -q^2$. In the D case p_b is a real photon, in the SR and DR cases p_b is a massless parton. The partonic cross section is given by the flux factor, the two-particle phase space and the matrix elements:

$$d\sigma(ij \to \text{jets}) = \frac{1}{2s} H(ij \to \text{jets}) d\text{PS}^{(2)} \quad . \tag{16}$$

The two-particle phase space is given by

$$d\text{PS}^{(2)} = \frac{1}{\Gamma(1-\epsilon)} \left(\frac{4\pi}{s}\right)^{\epsilon} [z(1-z)]^{-\epsilon} \frac{dz}{8\pi} \quad , \tag{17}$$

where $z \equiv (p_b p_1)/(p_a p_b)$. Expressed by the Mandelstam variables, the phase space reads

$$d\text{PS}^{(2)} = \frac{1}{\Gamma(1-\epsilon)} \left(\frac{4\pi}{stu}\right)^{\epsilon} (s + P^2)^{-1+2\epsilon} \frac{dt}{8\pi} \quad , \tag{18}$$

if the particle $p_a = q$ has mass $-P^2$. This is valid for the D and SR case. In the DR case all partons are massless, so we substitute $P^2 = 0$ and the phase space reduces to

$$d\text{PS}^{(2)} = \frac{1}{\Gamma(1-\epsilon)} \left(\frac{4\pi s}{tu}\right)^{\epsilon} \frac{dt}{8\pi s} \quad . \tag{19}$$

The Born matrix elements for the D and SR case read, using the notation of Tab. 1,

$$B_1 = (16\pi^2\alpha^2)\ (Q_i^4 8N_C)\ T_\gamma(s,t,u) \quad , \tag{20}$$

$$B_2 = -(16\pi^2\alpha\alpha_s)\ (Q_i^2 2C_F)\ T_\gamma(u,t,s) \quad , \tag{21}$$

$$B_3 = (16\pi^2\alpha\alpha_s)\ (Q_i^2)\ T_\gamma(s,t,u) \quad , \tag{22}$$

where the definition of $T_\gamma(s,t,u)$ can be found in the appendix, section 8.1. The Born matrix elements for the DR case are given by

$$B_4 = (16\pi^2\alpha_s^2)\ \tfrac{1}{4N_C^2}\ T_1(s,t,u) \quad , \tag{23}$$

$$B_5 = (16\pi^2\alpha_s^2)\ \tfrac{1}{4N_C^2}\ T_1(u,t,s) \quad , \tag{24}$$

$$B_6 = (16\pi^2\alpha_s^2)\ \tfrac{1}{2}\tfrac{1}{4N_C^2}\ [T_1(s,t,u)+T_1(s,u,t)+T_2(s,t,u)] \quad , \tag{25}$$

$$B_7 = (16\pi^2\alpha_s^2)\ \tfrac{1}{4N_C^2}\ T_1(u,s,t) \quad , \tag{26}$$

$$B_8 = (16\pi^2\alpha_s^2)\ \tfrac{1}{4N_C^2}\ [T_1(u,t,s)+T_1(u,s,t)+T_2(u,t,s)] \quad , \tag{27}$$

$$B_9 = (16\pi^2\alpha_s^2)\ \tfrac{1}{2}\tfrac{1}{4N_C^2}\ T_3(s,t,u) \quad , \tag{28}$$

$$B_{10} = -(16\pi^2\alpha_s^2)\ \tfrac{1}{8N_C^2C_F}\ T_3(t,s,u) \quad , \tag{29}$$

$$B_{11} = (16\pi^2\alpha_s^2)\ \tfrac{1}{16N_C^2C_F}\ T_3(s,t,u) \quad , \tag{30}$$

$$B_{12} = (16\pi^2\alpha_s^2)\ \tfrac{1}{2}\tfrac{1}{16N_C^2C_F}\ T_4(s,t,u) \quad . \tag{31}$$

The factors 1/2 in some of the expressions are symmetry factors for two identical particles in the final state. The definitions of the matrix elements $T_1,\ldots,T_4$ can again be found in the appendix 8.1.

The virtual corrections for the SR case are calculated by multiplying the one-loop diagrams for $\gamma^*\gamma \to q\bar{q}$, $\gamma^*q \to gq$ and $\gamma^*g \to q\bar{q}$ with the corresponding Born diagrams, which leads to an extra factor α_s in the matrix elements. The virtual corrections V_2 and V_3 are well known for quite some years from the processes $e^+e^- \to q\bar{q}g$ [53, 54]. They are achieved by crossing from the known matrix elements [31]. The contribution V_1 for the D case can be inferred from the SR case by considering the contribution $H_V(\gamma^*g \to q\bar{q})$. Only the parts which have no gluon self-coupling are taken into account and the color factors have to be adjusted appropriately. To compare the singular structure of the virtual corrections with those from the real corrections, we write down the final result for the D and SR case in the form

$$V_1 = 16\pi^2\frac{\alpha^2\alpha_s}{2\pi}\left(\frac{4\pi\mu^2}{s}\right)^\epsilon \frac{\Gamma(1-\epsilon)}{\Gamma(1-2\epsilon)}E_3 \quad , \tag{32}$$

$$\begin{aligned} V_2 &= 16\pi^2\frac{\alpha\alpha_s^2}{2\pi}2(1-\epsilon)\left(\frac{4\pi\mu^2}{s}\right)^\epsilon \frac{\Gamma(1-\epsilon)}{\Gamma(1-2\epsilon)}\left[C_F^2E_1-\frac{1}{2}N_CC_FE_2\right. \\ &+ \left.\frac{1}{\epsilon}\left(\frac{1}{3}N_f-\frac{11}{6}N_C\right)C_FT_\gamma(s,t,u)\right] \quad , \end{aligned} \tag{33}$$

$$\begin{aligned} V_3 &= 16\pi^2\frac{\alpha\alpha_s^2}{2\pi}\left(\frac{4\pi\mu^2}{s}\right)^\epsilon \frac{\Gamma(1-\epsilon)}{\Gamma(1-2\epsilon)}\left[C_FE_3-\frac{1}{2}N_CE_4\right. \\ &+ \left.\frac{1}{\epsilon}\left(\frac{1}{3}N_f-\frac{11}{6}N_C\right)T_\gamma(s,u,t)\right] \quad . \end{aligned} \tag{34}$$

Terms of order $\mathcal{O}(\epsilon)$ have been neglected. The expressions $E_1,\ldots,E_4$ are given in the appendix 8.2. In the DR case, the Born processes $B_4,\ldots,B_{12}$ have to be multiplied by the corresponding one-loop processes. The results can be found in [13]. They are given by $V_4,\ldots,V_{12}$ in [22].

3.3 Phase-Space-Slicing Method

As discussed in the section 2, the partonic $2 \to 3$ corrections are singular in certain regions of phase space. One possibility is to integrate the hard cross section over the complete phase space in n dimensions and to obtain analytical results for the integrated matrix elements. We choose a somewhat different method in this work. We separate the singular regions of phase space from the finite regions by inserting an invariant mass cutt-off y_c into the integration, symbolically

$$\int_0^1 d\mathrm{PS}^{(3)} |\mathcal{M}_{2\to 3}|^2 = \int_0^{y_c} d\mathrm{PS}^{(3)} |\mathcal{M}_{2\to 3}|^2 + \int_{y_c}^1 d\mathrm{PS}^{(3)} |\mathcal{M}_{2\to 3}|^2 \quad . \tag{35}$$

The first integral on the right hand side of this equation contains the singular region of phase space and is integrated analytically in $n = 4 - 2\epsilon$ space time dimensions. If the cut-off y_c is chosen appropriately small, this singular phase space separates into a $2 \to 2$ phase space $d\mathrm{PS}^{(2)}$ that will be kept and a remaining part $d\mathrm{PS}^{(r)}$ that is integrated out together with the matrix elements. For small y_c various approximations can be applied to the matrix elements, so that the integration of the matrix elements over $d\mathrm{PS}^{(r)}$ is simplified considerably as will become evident in sections 3.4–3.6. The non-singular second term on the right hand side of (35) is integrated numerically, opening the possibility to adopt a wide range of jet definitions and experimental cuts. This flexibility allows a detailed comparison between theory and experiment. Of course, the dependences of the first and the second contribution on the parameter y_c should compensate, leaving a result independent of y_c, since the cut-off has no physical significance. This also provides a strong test of the results, which will be described in section 5. The method described here is referred to as the phase-space-slicing (PSS) method [50].

An important step in the application of the PSS method is the separation of the two-body phase space from the singular part, $d\mathrm{PS}^{(3)} \to d\mathrm{PS}^{(2)} d\mathrm{PS}^{(r)}$. This separation is different for the three cases encountered in this work, which are singularities in the final state, in the initial state for massless particles and in the initial state for a massive virtual photon. In the next two subsections we will provide the formulæ that serve as a basis for the calculation of the singular parts of the partonic cross sections in sections 3.4–3.6.

3.3.1 Singularities in the Final and in the Massless Initial State We consider the splitting for a phase space containing one massive particle p_a with mass $P^2 = -p_a^2$. In general, the $2 \to 3$ phase space in n dimensions is given by [51]

$$d\mathrm{PS}^{(3)} = \frac{d^{n-1}p_1}{2E_1(2\pi)^{n-1}} \frac{d^{n-1}p_2}{2E_2(2\pi)^{n-1}} \frac{d^{n-1}p_3}{2E_3(2\pi)^{n-1}} (2\pi)^n \delta^n(p_b + q - p_1 - p_2 - p_3) \quad . \tag{36}$$

It is useful to introduce the following irreducible set of invariants:

$$s_0 = 2p_a p_b - P^2, \qquad t_1 = -2p_b p_1,$$

$$s_1 = 2p_1p_2, \qquad t_2 = -2p_ap_3 - P^2, \qquad (37)$$
$$s_2 = 2p_2p_3.$$

These five invariants are pictured in Fig. 5 on the left. The separation pictured on the right of Fig. 5 is achieved by inserting [52]

$$1 = \int \frac{ds_2}{2\pi} \int \frac{d^{n-1}p_{23}}{(2\pi)^{n-1}2E_{23}} \delta^{(n)}(p_{23} - p_2 - p_3)(2\pi)^n \qquad (38)$$

into (36), where the definition $s_2 = p_{23}^2 = (p_2+p_3)^2$ is used and E_{23} is the energy of this intermediate particle. One obtains

$$\begin{aligned} d\mathrm{PS}^{(3)} &= \frac{ds_2}{2\pi} \left\{ \frac{d^{n-1}p_1}{2E_1(2\pi)^{n-1}} \frac{d^{n-1}p_{23}}{2E_{23}(2\pi)^{n-1}} \delta^n(p_a + p_b - p_1 - p_{23})(2\pi)^n \right\} \\ &\times \left\{ \frac{d^{n-1}p_2}{2E_2(2\pi)^{n-1}} \frac{d^{n-1}p_3}{2E_3(2\pi)^{n-1}} \delta^n(p_{23} - p_2 - p_3)(2\pi)^n \right\} \quad . \end{aligned} \qquad (39)$$

To perform the integration over the delta functions in (39) it is useful to define the kinematical variables in the c.m. system of the outgoing partons p_2 and p_3. The angles of the partons p_1 and p_2, p_3 with respect to the parton p_b are shown in Fig. 6. To parametrize the angles, the variables $b \equiv \frac{1}{2}(1 - \cos\theta)$ and $z_1 \equiv (p_bp_1)/(p_ap_b)$ are used. After integrating over the delta functions and expressing the variables by z_1, b and the irreducible invariants introduced in (37), the three particle phase space in $n = 4 - 2\epsilon$ dimensions reads

$$d\mathrm{PS}^{(3)} = \frac{ds_2}{2\pi} \frac{dz_1}{64\pi^2} \frac{db}{N_b} [b(1-b)]^{-\epsilon} \frac{d\phi}{N_\phi} \frac{\sin^{-2\epsilon}\phi}{\Gamma(2-2\epsilon)} \left[\frac{16\pi^2}{s_2 z_1 (s_0(1-z_1) - s_2)} \right]^\epsilon \quad , \qquad (40)$$

with the normalization constants

$$N_b = \int_0^1 db[b(1-b)]^{-\epsilon} = \frac{\Gamma^2(1-\epsilon)}{\Gamma(2-2\epsilon)} \quad \text{and} \quad N_\phi = \int_0^\pi d\phi \sin^{-2\epsilon}\phi = \frac{4^\epsilon \pi \Gamma(1-2\epsilon)}{\Gamma^2(1-\epsilon)} \quad . \qquad (41)$$

For singularities in the final state the invariants s_2 and b will vanish, whereas for the singularities in the initial state of the massless particle p_b the invariant t_1 and therefore z_1 will vanish.

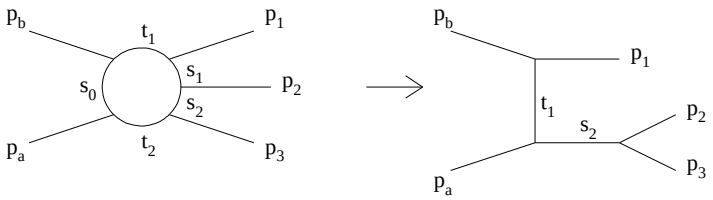

Fig. 5. Separation of the three particle phase space.

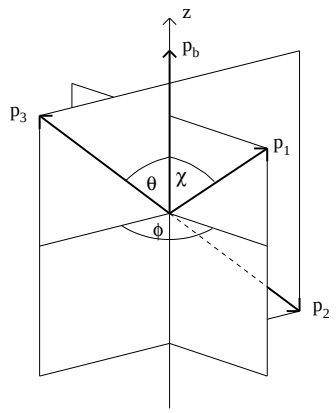

Fig. 6. The three particle final state in the c.m. system of the particles p_2 and p_3.

3.3.2 Singularities in the Initial State of a Virtual Photon For this case, the mass $P^2 = -p_a^2$ of the photon with momentum p_a serves as a regulator for the integration. Therefore, the phase space (36) can be calculated in $n = 4$ dimensions. We introduce the five invariants

$$\begin{aligned} s_0 &= 2p_a p_b - P^2, & t_1 &= -2p_b p_3, \\ s_1 &= 2p_1 p_2, & t_2 &= -2p_a p_1 - P^2, \\ s_2 &= 2p_2 p_3, \end{aligned} \tag{42}$$

and separate the phase space analogously to the case discussed above by inserting (38) into (36). Again we move to the c.m. frame of the particles p_2 and p_3 and define the variable $b \equiv \frac{1}{2}(1-\cos\theta)$, but now θ is defined as the angle between p_a and p_3. The singularities occur for $t_2 \to 0$, which we parametrize by the variable $z_2 \equiv (p_a p_3)/(p_a p_b)$. It is obvious from the definition of t_2 that the variable z_2 vanishes only for $P^2 \to 0$. After integrating over the delta functions, the result is simply

$$d\mathrm{PS}^{(3)} = \frac{d\phi}{\pi}\frac{ds_2}{2\pi}\frac{dz_2}{8\pi}\frac{db}{8\pi} \quad . \tag{43}$$

3.4 Final State Singularities

The singularities in the final state appear when the invariant s_2 in equation (37) becomes on-mass-shell. We define the variable $r \equiv s_2/s_0$ and consider the limit $r \to 0$. We start by considering the D and SR cases, for which we define the two-body Mandelstam variables as

$$\begin{aligned} s &= (p_b+q)^2 = 2p_b q - P^2, \quad , \\ t &= (p_b-p_1)^2 = -2p_b p_1 \quad , \\ u &= (p_b-p_{23})^2 = -2p_b p_{23} \quad . \end{aligned} \tag{44}$$

In the limit $r \to 0$ the five invariants (37) reduce to these variables, with $s_0 \to s$ and $t_1 \to t$. The definitions of s, t and u are only unique in the limit $r \to 0$. In the limit $s_2 \to 0$ the phase space (40) separates according to $d\mathrm{PS}^{(3)} = d\mathrm{PS}^{(2)} d\mathrm{PS}^{(r)}$ with

$$d\mathrm{PS}^{(r)} = \frac{\Gamma(1-\epsilon)}{\Gamma(2-2\epsilon)} \frac{d\phi}{N_\phi} \sin^{-2\epsilon}\phi \left(\frac{4\pi}{s}\right)^{\epsilon} \frac{s}{16\pi^2} G_F(r) dr r^{-\epsilon} \frac{db}{N_b} [b(1-b)]^{-\epsilon} \quad (45)$$

where

$$G_F(r) = \left[1 - \frac{r}{(1-z)}\right]^{-\epsilon} = 1 + \mathcal{O}(r) \quad . \quad (46)$$

The two-body phase space $d\mathrm{PS}^{(2)}$ is given by equation (18). The limits of integration in $d\mathrm{PS}^{(r)}$ are given by $r \in [0, -t/(s+P^2)], b \in [0,1]$ and $\phi \in [0, \pi]$. The invariant s_2 is integrated up to $s_2 \leq y_c s_0$, which restricts the range of r to $0 \leq r \leq \min[-t/(s+P^2), y_c] \equiv y_F$.

We have now achieved the separation of the phase space and have to integrate the matrix elements over the region $d\mathrm{PS}^{(r)}$. Therefore the $2 \to 3$ matrix elements $H_1, \ldots H_5$ are expressed by the variables s, t, u, r, b and ϕ in the limit $r \to 0$, which leads to approximated matrix elements with final state singularities $H_{F1}, \ldots, H_{F5}$ [31]. A difficulty arises for those squared matrix elements that contain real gluons. In that case more than one invariant can vanish in a propagator, so that the different classes of singularities, such as initial and final state singularities, are not properly separated. The separation is achieved by partially fractioning the matrix elements.

After the matrix elements have been partially fractioned and approximated in the limit $r \to 0$, the integration over the singular region of phase space yields

$$\int d\mathrm{PS}^{(r)} H_{Fi} = 8\pi \left(\frac{4\pi\mu^2}{s}\right)^{\epsilon} \frac{\Gamma(1-\epsilon)}{\Gamma(1-2\epsilon)} (1-\epsilon) F_i + \mathcal{O}(\epsilon) \quad . \quad (47)$$

The final results for $F_1, \ldots, F_5$ are listed in appendix 8.3. They contain the IR collinear and soft singularities that cancel against those of the virtual corrections. It is essential that the singular terms are proportional to the LO matrix elements T_γ and that the variables s, t and u defined in (44) correspond to the two-body variables in the above discussed limit. The contributions $F_2, \ldots, F_5$ have been calculated in [31]. The final state correction F_1 of the D contribution can be derived from F_5 by keeping only the abelian part and adjusting the color factor. One can compare the singularities for the case of direct real photons as stated in [22] with the ones given in appendix 8.3. The real photon contributions $F_1, \ldots, F_5$ in [22] follow from the contributions $F_1, \ldots, F_5$ in this work by taking the limit $P^2 \to 0$, so that $t + u = -s$.

Turning to the resolved photon case, the phase space is obtained from the formula (45) by substituting $q \to p_a$ with $p_a^2 = 0$, so that $s = 2p_a p_b$. The two-body variables in the resolved case are given by

$$s = 2p_a p_b, \qquad t = -2p_b p_1, \qquad u = -2p_b p_{23} \quad . \quad (48)$$

Note, that the two-body phase space for the DR case is given by equation (19) of section 3.2. Expressing the matrix elements for the resolved processes

$H_6, \ldots, H_{16}$ as classified in Tab. 3 through the variables s, t, u, r, b and ϕ yields the matrix elements containing final state singularities $H_{F6}, \ldots, H_{F16}$ [13, 22]. The integral over the singular phase space is the same as in equation (47). The final state corrections for the resolved case $F_6, \ldots, F_{16}$ will not be stated here again since they can be found in [22].

3.5 Initial State Singularities for Massless Particles

We turn to the discussion of the initial state singularities for particles with zero mass. This includes the photon initial state singularity for the real photon for the D case, the parton initial state singularities in the SR case and the parton initial state singularities in the DR case. We start with the SR case, from which the others can be inferred.

3.5.1 Parton Initial State Singularities in the SR Case In the SR case parton initial state singularities arise for the incoming particle p_b. The incoming particle p_a is the virtual photon with $p_a = q$ and $P^2 = -q^2$. Using the notation of section 3.3.1, the singularities appear when the invariant t_1 becomes on-mass-shell, i.e. for $z_1 \to 0$. The invariant s_2 does not vanish in the case of initial state singularities but rather defines the partonic c.m. energy of the corresponding two-body process. We define the new variable

$$z_b \equiv \frac{p_2 p_3}{q p_b} = \frac{s_2}{s_0 + P^2} \in [\eta_b, 1] \quad , \tag{49}$$

that gives the fraction of the momentum p_b that participates in the subprocess after a particle has been radiated in the initial state. The variable η_b is given by $\eta_b = x_b z_b$. We define the two-body variables as

$$\begin{aligned} s &= (p_2 + p_3)^2 = 2 p_2 p_3 \quad , \\ t &= (z_b p_b - p_2)^2 = -2 z_b p_b p_2 \quad , \\ u &= (z_b p_b - p_3)^2 = -2 z_b p_b p_3 \quad . \end{aligned} \tag{50}$$

In the limit $z \to 0$ the variable s_2 reduces to s. In the same limit the phase space (40) separates according to $d\mathrm{PS}^{(3)} = d\mathrm{PS}^{(2)} d\mathrm{PS}^{(r)}$, where

$$\begin{aligned} d\mathrm{PS}^{(r)} &= \frac{1}{\Gamma(1-\epsilon)} \frac{d\phi}{N_\phi} \sin^{-2\epsilon}\phi \left(\frac{4\pi}{s}\right)^{\epsilon} \frac{s}{16\pi^2} G_I(z_1) \\ &\times \; dz_1 z_1^{-\epsilon} \frac{dz_b}{z_b} \left(\frac{1-z_b}{z_b} - \frac{P^2}{s}\right)^{-\epsilon} \left(1 + \frac{P^2(1-z_b)}{z_b(z_b s - (1-z_b)P^2)}\right)^{1-\epsilon} \end{aligned} \tag{51}$$

with

$$G_I(z_1) = \left[1 - z_1 \frac{s - z_b P^2}{s(1-z_b) - z_b P^2}\right]^{-\epsilon} = 1 + \mathcal{O}(z_1) \quad . \tag{52}$$

The two-body phase space is given by equation (18). The integration over $d\mathrm{PS}^{(r)}$ with $z_1 \in [0, -u/(s+P^2)]$, $z_b \in [\eta_b, 1]$ and $\phi \in [0, \pi]$ is restricted to the singular region of z_1 in the range $0 \le z_1 \le \min\{-u/(s+P^2), y_c\} \equiv y_I$.

Expressing the matrix elements for the direct photon case, listed in Tab. 2, with the variables s, t, u, z_1, z_b, b and ϕ and taking the limit $z_1 \to 0$, one obtains the matrix elements $H^b_{I2}, \ldots, H^b_{I5}$ [31] that contain initial state singularities on the parton side B. These are integrated according to

$$\int d\mathrm{PS}^{(r)} H^b_{Ii} = \int\limits_{\eta_b}^{1} \frac{dz_b}{z_b} 8\pi \left(\frac{4\pi\mu^2}{s}\right)^{\epsilon} \frac{\Gamma(1-\epsilon)}{\Gamma(1-2\epsilon)} (1-\epsilon) I^b_i + \mathcal{O}(\epsilon) \quad . \tag{53}$$

where results for $I^b_2, \ldots, I^b_5$ are written down in appendix 8.4. They can also be found in [31]. Apart from the two-body variables s, t, u and the cut-off y_I, they still depend on the integration variable z_b. The results for the I^b_i contain IR singularities proportional to $1/\epsilon^2$ that cancel against the corresponding singularities in the virtual corrections. The remaining singular parts are proportional to $1/\epsilon$ and to the Altarelli-Parisi kernels in four dimensions. These are removed by a redefinition of the PDF's that are the source of particle p_b, which can be a hadron or a resolved photon. The redefinition, as explained in section 2.2, is achieved by equation (6) for the PDF's, introducing the factorization scale (M_b) dependence through the transition functions $\Gamma^{(1)}_{i\leftarrow j}$:

$$\bar{f}_{iB}(\eta_b, M_b^2) = \int\limits_{\eta_b}^{1} \frac{dz_b}{z_b} \left(\delta_{ij}\delta(1-z_b) + \frac{\alpha_s}{2\pi}\Gamma^{(1)}_{i\leftarrow j}(z_b, M_b^2)\right) f_{jB}\left(\frac{\eta_b}{z_b}\right) \quad . \tag{54}$$

Here $f_{jB}\left(\frac{\eta_b}{z_b}\right)$ is the PDF of hadron B in LO before absorption of the collinear singularities. The NLO transition functions are given by

$$\Gamma^{(1)}_{i\leftarrow j}(z_b, M_b^2) = -\frac{1}{\epsilon} P_{i\leftarrow j}(z_b) \frac{\Gamma(1-\epsilon)}{\Gamma(1-2\epsilon)} \left(\frac{4\pi\mu^2}{M_b^2}\right)^{\epsilon} + C_{ij}(z_b) \tag{55}$$

with $C_{ij} = 0$ in the $\overline{\mathrm{MS}}$ scheme. The renormalized partonic cross section $d\bar{\sigma}(\gamma^* i \to$ jets) for parton initial state singularities is calculated from the unrenormalized cross section $d\sigma$ by

$$d\bar{\sigma}(\gamma^* i \to \mathrm{jets}) = d\sigma(\gamma^* i \to \mathrm{jets}) - \frac{\alpha_s}{2\pi} \sum_j \int dz_b \Gamma^{(1)}_{i\leftarrow j}(z_b, M_b^2) d\sigma^B(\gamma^* j \to \mathrm{jets}) \quad . \tag{56}$$

The $d\sigma^B$'s denote the Born level partonic cross sections that can be found in section 3.2. The factor $4\pi\mu^2/M_b^2$ in equation (55) is combined with the factor $4\pi\mu^2/s$ in equation (53) and leads to a factorization scale dependent term of the form

$$-\frac{1}{\epsilon} P_{i\leftarrow j}(z_b) \left[\left(\frac{4\pi\mu^2}{s}\right)^{\epsilon} - \left(\frac{4\pi\mu^2}{M_b^2}\right)^{\epsilon}\right] = -P_{i\leftarrow j}(z_b) \ln\left(\frac{M_b^2}{s}\right) \quad . \tag{57}$$

In this way, the subtracted partonic cross section will depend on the scale M_b^2, as does the PDF of the hadron B, f_{iB}.

3.5.2 Real Photon Initial State Singularities in the D Case In the D case the direct real photon can split into a $q\bar{q}$ pair that gives rise to a collinear singularity if the partons are emitted parallel. The calculation proceeds along the lines that have been described for the parton initial state singularities in the previous section 3.5.1. The two-body variables are defined as in equations (50). The phase space separation as well as the formula (53) for the integration over the singular regions remains unchanged. For the singular matrix element $H^b_{I1} = H^b_I(\gamma^*\gamma \to q\bar{q}g)$ we have

$$\int d\mathrm{PS}^{(r)} H^b_{I1} = \int\limits_{\eta_b}^{1} \frac{dz_b}{z_b} 8\pi \left(\frac{4\pi\mu^2}{s}\right)^{\epsilon} \frac{\Gamma(1-\epsilon)}{\Gamma(1-2\epsilon)} (1-\epsilon) I^b_1 + \mathcal{O}(\epsilon) \quad , \tag{58}$$

where I^b_1 is stated in the appendix 8.4. As remarked for the virtual and final state corrections, the initial state correction for the D case can be infered from the SR case with an incoming gluon instead of the real photon by dropping the non-abelian terms and adjusting the color factor. The singularity appearing in I^b_1 is proportional to the splitting function $P_{q\leftarrow\gamma}(z_b)$ given in appendix 8.1. This function appears in the evolution equation of the PDF of the real photon as an inhomogeneous (so-called point-like) term, as will be explained in more detail in section 4. Therefore, the photon initial state singularities can be absorbed into the real photon PDF, according to the procedure given in [48]. We define the renormalized PDF $\bar{f}_{qe}$ of a quark q in the electron as

$$\bar{f}_{qe}(\eta_b, M_b^2) = \int\limits_{\eta_b}^{1} \frac{dz_b}{z_b} \left(\delta_{q\gamma}\delta(1-z_b) + \frac{\alpha_s}{2\pi}\Gamma^{(1)}_{q\leftarrow\gamma}(z_b, M_b^2)\right) f_{\gamma e}\left(\frac{\eta_b}{z_b}\right) \quad . \tag{59}$$

The NLO transition functions are given by

$$\Gamma^{(1)}_{q\leftarrow\gamma}(z_b, M_b^2) = -\frac{1}{\epsilon} P_{q\leftarrow\gamma}(z_b) \frac{\Gamma(1-\epsilon)}{\Gamma(1-2\epsilon)} \left(\frac{4\pi\mu^2}{M_b^2}\right)^{\epsilon} + C_{q\gamma}(z_b) \tag{60}$$

with $C_{q\gamma} = 0$ in the $\overline{\mathrm{MS}}$ scheme. In the discussed order, $P_{g\leftarrow\gamma}(z) = 0$. The partonic cross section $d\bar{\sigma}(\gamma^*\gamma \to \text{jets})$ for the photon initial state singularity is calculated from the unrenormalized cross section $d\sigma$ by

$$d\bar{\sigma}(\gamma^*\gamma \to \text{jets}) = d\sigma(\gamma^*\gamma \to \text{jets}) - \frac{\alpha_s}{2\pi} \int dz_b \Gamma^{(1)}_{q\leftarrow\gamma}(z_b, M_b^2) d\sigma^B(\gamma^* q \to \text{jets}) \quad . \tag{61}$$

The cross section $d\sigma^B$ contains the LO virtual photon-parton scattering matrix element B_2 given in section 3.2. The dependence of the real photon PDF on the factorization scale enters in the same way as discussed for the SR case, section 3.4.1.

3.5.3 Parton Initial State Singularities in the DR Case The calculation of the initial state singularities for the DR case is very similar to the calculations shown for the SR case, only now both incoming partons are massless. The

calculations for the partons p_a and p_b yield identical results and thus we have to consider these singularities only once. The singularities occur in the region $z_1 \to 0$. The formula for the phase space separation is obtained from equation (51) by substituting $q \to p_a$ with $p_a^2 = P^2 = 0$, so that $s = 2z_b p_a p_b$. With these substitutions, the phase space (51) reduces to

$$d\mathrm{PS}^{(r)} = \frac{1}{\Gamma(1-\epsilon)} \frac{d\phi}{N_\phi} \sin^{-2\epsilon}\phi \left(\frac{4\pi}{s}\right)^{\epsilon} \frac{s}{16\pi^2} G_I(z_1) dz_1 z_1^{-\epsilon} \frac{dz_b}{z_b} \left(\frac{1-z_b}{z_b}\right)^{-\epsilon} \tag{62}$$

with

$$G_I(z_1) = \left[1 - \frac{z_1}{1-z_b}\right]^{-\epsilon} = 1 + \mathcal{O}(z_1) \quad . \tag{63}$$

The two-body phase space in the case of initial state singularities is given by (19). Expressing the resolved matrix elements $H_6, \ldots, H_{16}$ with the variables s, t, u, z_1, z_b, b and ϕ in the limit $z_1 \to 0$ leads to the resolved matrix elements containing initial state singularities $H_{J_6}, \ldots, H_{J_{16}}$ [13, 22]. These are integrated similar to equation (53), leading to the results $J_6, \ldots, J_{16}$. These are not stated here, they can be found in [13, 22]. The initial state singularities on the proton side $J_6, \ldots, J_{16}$ are given by $R_6^a, \ldots R_{16}^a$ in [22]. The cancellation of the poles from the real and virtual corrections proceeds as in the SR case discussed above. The remaining poles in $1/\epsilon$ are proportional to the Altarelli-Parisi kernels and are absorbed into the PDF's of the hadrons A and B that emit the particles p_a and p_b.

3.6 Initial State Singularities for the Virtual Photon

The initial state singularities described in the previous section were extracted and handled in the dimensional regularization scheme, i.e. in $d = 4 - 2\epsilon$ dimensions. In the case of the real photon this is necessary, because the real photon is massless. The singular terms are proportional to a simple pole in ϵ multiplied by the splitting function $P_{q \leftarrow \gamma}$. These initial state singularities are absorbed into the PDF of the real photon. The NLO correction for the direct virtual photon becomes singular only in the limit $P^2 \to 0$. After integrating the phase space up to the invariant cut-off y_c, the logarithm $\ln(P^2/s)$ will occur that becomes large in the limit of small P^2. The logarithm has to be absorbed into the PDF of the virtual photon, instead of the $1/\epsilon$ poles in the real photon case.

To show the subtraction of the logarithm explicitly, we start by defining the two-body variables for the virtual photon initial state singularities. They are given by

$$\begin{aligned} s &= (p_2 + p_3)^2 = 2p_2p_3 \quad , \\ t &= (p_b - p_2)^2 = -2p_bp_2 \quad , \\ u &= (p_b - p_3)^2 = -2p_bp_3 \quad . \end{aligned} \tag{64}$$

We define the variable z_a as

$$z_a \equiv \frac{p_2 p_3}{q p_b} = \frac{s_2}{s_0 + P^2} \in [\eta_a, 1] \tag{65}$$

with $\eta_a = x_a z_a$. It gives the momentum fraction of the three-body c.m. energy that participates in the two-body process. The definition of the three-body variables is given in section 3.3.2, equation (42). As mentioned above, the mass P^2 regularizes the initial state singularities of the virtual photon. The singular terms appear in the case $t_2 \to 0$ in (42), which corresponds to $z_2 \to 0$ for $P^2 \to 0$. For $z_2 \to 0$ the phase space (43) separates according to $d\mathrm{PS}^{(3)} = d\mathrm{PS}^{(2)} d\mathrm{PS}^{(r)}$, with

$$d\mathrm{PS}^{(r)} = \frac{s}{16\pi^2}\frac{d\phi}{\pi}\frac{dz_a}{z_a}dz_2 \qquad \text{and} \qquad d\mathrm{PS}^{(2)} = \frac{1}{8\pi}\,\frac{dt}{s+P^2} \quad . \tag{66}$$

The limits of integration are given by $z_2 \in [0, -t/(s+P^2)]$, $z_a \in [\eta_a, 1]$ and $\phi \in [0, \pi]$. Since the integration of z_2 is restricted to the singular region we define the integration range for z_2 by $0 \le z_2 \le \min\{-t/(s+P^2), y_c\} \equiv y_J$.

Expressing the matrix elements for the direct photon case, listed in Tab. 2, with the help of the variables s, t, u, z_2, z_b, b and ϕ and taking the limit $z_2 \to 0$, we obtain matrix elements $H^a_{I1}, \ldots, H^a_{I5}$ that contain the initial state singularities on the virtual photon side. These are integrated according to

$$\int d\mathrm{PS}^{(r)} H^a_{Ii} = \int\limits_{\eta_a}^{1} \frac{dz_a}{z_a} 8\pi I^a_i \quad . \tag{67}$$

The results for $I^a_1, \ldots, I^a_5$ are collected in appendix 8.5. They contain the singularities for the D and SR contributions. Apart from s, t, u and y_J, the results also depend on the integration variable z_a. All five expressions $I^a_1, \ldots, I^a_5$ contain the term

$$M(P^2) = \frac{1}{2N_C} P_{q\leftarrow\gamma}(z_a) \ln\left(1 + \frac{y_J s}{z_a P^2}\right) \tag{68}$$

which is large for $P^2 \ll s$ and singular for $P^2 = 0$ as expected. The large contribution has to be subtracted and absorbed into the PDF of the virtual photon. Here, we have the same freedom as in the case of the real photon, as has been described above for the D case. Finite parts can be shifted from the PDF to the direct cross section and vice versa.

However, the virtual photon PDF's used later on in this work are constructed in a scheme similar to the $\overline{\mathrm{MS}}$ scheme for real photons and we have to use the same scheme to obtain consistent results. Therefore, we subtract those terms that will yield the $\overline{\mathrm{MS}}$ scheme of the real photon in the limit $P^2 \to 0$. In order to make the comparison with the case of the real photon possible, we state here the singular parts of the expressions $I^a_1, \ldots I^a_5$, that appear for the real photon in $d = 4 - 2\epsilon$ dimensions. They are given by [14]

$$M = -\frac{1}{\epsilon}\frac{1}{2N_C} P_{q\leftarrow\gamma}(z_a) + \frac{1}{2N_C} P_{q\leftarrow\gamma}(z_a) \ln\left(\frac{(1-z_a)}{z_a} y_J\right) + \frac{1}{2} \quad . \tag{69}$$

The characteristic singularity proportional to $1/\epsilon$ is subtracted by absorbing the transition function

$$\Gamma^{(1)}_{q\leftarrow\gamma}(z_a, M^2_\gamma) = -\frac{1}{\epsilon} P_{q\leftarrow\gamma}(z_a) \frac{\Gamma(1-\epsilon)}{\Gamma(1-2\epsilon)} \left(\frac{4\pi\mu^2}{M^2_\gamma}\right)^{\epsilon} \tag{70}$$

into the PDF of the real photon. This subtraction produces a factorization scale dependence of the photon PDF and gives the finite contributions to the cross section. The expression remaining after the absorption is, in the $\overline{\text{MS}}$ scheme:

$$M_{\overline{MS}} = -\frac{1}{2N_C} P_{q\leftarrow\gamma}(z_a) \ln\left(\frac{M_\gamma^2 z_a}{y_J s(1-z_a)}\right) + \frac{1}{2} \quad . \tag{71}$$

In order to obtain the same finite terms in $M(P^2)$ from equation (68) in the limit $P^2 \to 0$ for the virtual photon case, we absorb the transition function

$$\Gamma^{(1)}_{q\leftarrow\gamma^*}(z_a, M_\gamma^2, P^2) = \ln\left(\frac{M_\gamma^2}{P^2(1-z_a)}\right) P_{q\leftarrow\gamma}(z_a) - N_C \tag{72}$$

into the PDF of the virtual photon. This leaves the finite term

$$M_{\overline{MS}}(P^2) = -\frac{1}{2N_C} P_{q\leftarrow\gamma}(z_a) \ln\left(\frac{M_\gamma^2 z_a}{(z_a P^2 + y_J s)(1-z_a)}\right) + \frac{1}{2} \quad , \tag{73}$$

that reduces to the expression $M_{\overline{MS}}$ in (71) for real photons in the limit $P^2 \to 0$. We therefore call this form of factorization the $\overline{\text{MS}}$ factorization for virtual photons.

4 Parton Distribution Function of the Photon

As mentioned in the introduction and worked out in section 3, the photon produces a $q\bar{q}$-pair in the initial state of the NLO direct contribution that leads to a large logarithm for virtual photons and a singularity for real photons. These terms have to be absorbed into the PDF of the virtual and real resolved photons, respectively, leading to a point-like term in the evolution equations of the photon PDF's. In this section, we wish to introduce the PDF of the real and the virtual photon.

After a general discussion of the origin of the photon structure, we define the structure function and the PDF of the real photon. The evolution equations will be explained and the differences to the proton will be pointed out. A discussion of the formalism for the virtual photon PDF resembling the formalism for the real photon follows. Finally, we compare two parametrizations of the virtual photon PDF which we use in our computations.

4.1 Origin of the Photon Structure

The photon is the elementary gauge boson of QED. However one knows from soft low energy γp reactions, that a photon can behave like a hadron. If the time of the interaction between the proton and the photon is much smaller than the fluctuation time t_f of the $q\bar{q}$-pair, the pair will interact with the proton rather than with the photon itself and will give rise to a hadronic structure of the

photon. The fluctuation time for high energy photons with virtuality P^2 can be estimated from the uncertainty principle by [55]

$$t_f = \frac{2q_0}{P^2 + m_{q\bar{q}}^2} \quad , \tag{74}$$

where q_0 is the energy of the photon and $m_{q\bar{q}}$ is the mass of the pair. As P^2 increases, t_f becomes smaller, giving back the photon its structureless character. Thus, one can identify the direct photon, which interacts directly as a structureless object, and the resolved photon, which has a hadronic structure.

At this point it is important to further distinguish the possible configurations of the $q\bar{q}$-pair which yield different contributions to the resolved photon. The photon can create a large size, asymmetric configuration with small transverse momentum k_T that gives rise to soft non-perturbative effects and a small size, symmetric configuration with large k_T that yields hard, perturbative interactions [56]. The soft part will behave more like a hadron and it will therefore be called the *hadronic* part of the resolved photon, whereas the hard part behaves more like a point-like photon and will therefore be called the *point-like* part. A possible physics interpretation of the soft part of the resolved photon is the fluctuation of the $q\bar{q}$-pair into a vector-meson with $m_{q\bar{q}} \simeq m_V$, which is described by the vector-meson dominance (VMD) model [57]. The coupling of the photon to the vector-meson $\frac{4\pi}{f_V^2}$ has been predicted by the VMD model, giving

$$\frac{f_\rho^2}{4\pi} : \frac{f_\omega^2}{4\pi} : \frac{f_\varphi^2}{4\pi} = 9 : 1 : 7 \quad . \tag{75}$$

These ratios have been confirmed by measurements of the reaction $e^+e^- \rightarrow$ hadrons.

We have introduced the distinction between direct and resolved photons, but this distinction is unambiguous only in LO. In NLO the direct and resolved parts of the photon become intermixed through the point-like part of the resolved photon. A possibility to distinguish between the direct and the resolved photon interaction has been suggested by Levy [56]. Consider photon-gluon fusion as shown in Fig. 7. The diagram on the left is usually denoted as a direct process

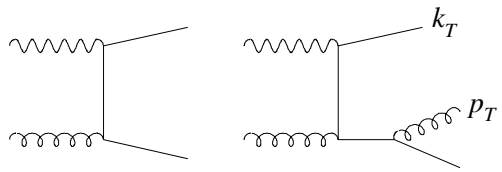

Fig. 7. Direct and resolved photon processes for photon-gluon fusion.

in LO. The diagram on the right describes the fluctuation of the photon into a $q\bar{q}$ pair with a given k_T followed by the interaction of one of the partons with a gluon, which produces a final state with some p_T. If $k_T \ll p_T$, the process can

be called a resolved interaction. For $k_T \gg p_T$ the p_T is too small for the final state partons to form two separate jets, so the diagram looks like the diagram on the left und thus can be considered as a direct interaction. For large P^2 it is more likely that $k_T \gg p_T$ so that the direct component is dominant. For low P^2 the resolved part will be more dominant.

4.2 Parton Distribution Functions of the Real Photon

The structure of the real photon has been analyzed in the process $e\gamma \to eX$, depicted in Fig. 8. We define $x \equiv Q^2/(Q^2+W^2)$ with $Q^2 = -q^2$ and $P^2 = -p^2$, where W is the c.m. energy of the $\gamma^*\gamma$ system and $y \equiv (pq)/(pk)$. Denoting the longitudinal polarization state of the photon as l and the transversal one as t, we can define photon structure functions

$$F_1^\gamma = \frac{Q^2}{4\pi\alpha}\frac{1}{2x}\sigma_{tt} \quad , \tag{76}$$

$$F_2^\gamma = \frac{Q^2}{4\pi\alpha}(\sigma_{tt}+\sigma_{lt}) \quad . \tag{77}$$

Using these definitions, the cross section for $e\gamma$ scattering can be written as

$$\frac{d\sigma(e\gamma \to eX)}{dxdy} = \frac{4\pi\alpha s}{Q^4}\left[(1-y)F_2^\gamma + xy^2F_1^\gamma\right] \quad . \tag{78}$$

This is in complete analogy to the DIS ep reaction. The difference to the case of ep scattering lies in the fact that the photon structure function can be calculated perturbatively in the limit of large Q^2. This is not possible for the proton structure function. The photon structure function is computable in the quark-parton model (QPM) from the box diagram $\gamma^*\gamma \to q\bar{q}$ and gives in LO in the limit $m_{q_i}^2 \ll Q^2$, where m_{q_i} are the quark masses, [59, 60, 61]

$$F_2^{\gamma,pl} = \sum_{i=1}^{N_f} x q_i^\gamma(x,Q^2) \tag{79}$$

with

$$q_i^\gamma(x,Q^2) = 3e_{q_i}^2\frac{\alpha}{2\pi}\left\{[x^2+(1-x)^2]\ln\frac{Q^2(1-x)}{m_{q_i}^2 x} + 8x(1-x) - 1\right\} \quad . \tag{80}$$

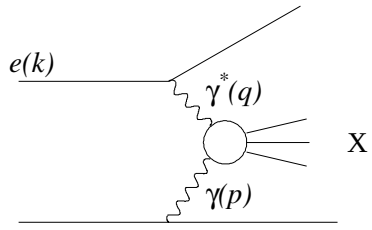

Fig. 8. Single-tag DIS $e\gamma$ experiment.

The function q_i^γ can be interpreted as the PDF of the quark in the photon, in analogy to the proton case.

The QPM result can be modified substantially by QCD effects, such as multiple gluon radiation ladder diagrams. In the limit of large Q^2 these kind of corrections where shown to be exactly calculable in LO [46] and NLO [47]. The result is of the form

$$F_2^{\gamma,asymp} = \alpha \left[\frac{a(x)}{\alpha_s(Q^2)} + b(x) \right] \quad , \tag{81}$$

where $a(x)$ is the LO and $b(x)$ the NLO result. Unfortunately $F_2^{\gamma,asymp}$ becomes negative for small values of x, which cannot be true, since the photon structure function is measurable. The problem cannot be cured by adding the VMD contributions that have been mentioned in the previous section, since this non-perturbative contribution is expected to be well-behaved. Therefore it is not possible to compute the photon structure function by perturbation theory alone.

To handle the problems of the photon structure function, Glück and Reya [62] have suggested to formally add all contributions to the photon structure, namely the QPM, their QCD corrections and the VMD contributions into a single photon structure function $F_2^\gamma = \sum_i x q_i^\gamma(x, Q^2)$ and fix the quark distributions at some input scale Q_0^2 in analogy to the proton case. Then the photonic parton densities at different values of Q^2 follow from the inhomogeneous evolution equations, that are in LO

$$\frac{dq_i^\gamma}{dt} = h^{box} + \frac{\alpha_s}{2\pi} \int_x^1 \frac{dz}{z} \left[P_{q \leftarrow q}\left(\frac{x}{z}\right) q_i^\gamma + P_{g \leftarrow q}\left(\frac{x}{z}\right) g^\gamma \right] \tag{82}$$

$$\frac{dg^\gamma}{dt} = \frac{\alpha_s}{2\pi} \int_x^1 \frac{dz}{z} \left[P_{q \leftarrow g}\left(\frac{x}{z}\right) q_i^\gamma + P_{g \leftarrow g}\left(\frac{x}{z}\right) g^\gamma \right] \quad . \tag{83}$$

Here, $t \equiv \ln(Q^2/\Lambda^2)$ and the inhomogeneity is given by

$$h^{box} = 3 e_{q_i}^2 \frac{\alpha}{2\pi} [x^2 + (1-x)^2] \quad . \tag{84}$$

The solution of the homogeneous equations is similar to the solution of the DGLAP equations for hadrons and can therefore be called $F_2^{\gamma,had}$. The particular solution of the inhomogeneous equation is due to the inhomogeneity that stems from the point-like coupling of the photons to the quarks and can therefore be called $F_2^{\gamma,pl}$. The general solution of the inhomogeneous evolution equations for the photon is thus given by

$$F_2^\gamma = F_2^{\gamma,had} + F_2^{\gamma,pl} \quad . \tag{85}$$

This equation allows one to speak about the hadronic and the point-like part of the photon structure function.

The measurement of the photon structure function is not as easy as for the proton case. Due to limited detector acceptance, the measured hadronic energy is not equal to the total hadronic energy, so that the photon energy is

not determined well, which leads to large systematic errors. In addition, the structure function F_2^γ is small and the cross section (78) is suppressed by $1/Q^4$, which leads to large statistical errors. In spite of these difficulties, the photon structure has been measured for various values of Q^2. In Fig. 9 all existing data for F_2^γ is presented as a function of x for different values of Q^2 (taken from [58]).

One important difference in the behaviour of the proton and the photon structure functions is that F_2^γ manifests strong scaling violation even in LO without gluon radiation included. It is positive in the whole x region. Furthermore, F_2^γ should be large at large x due to the point-like part of the photon structure function, while the structure function of the proton is small at large x. Predictions from several parametrizations for the PDF of the real photon (solid curve [33], dashed curve [34], dotted curve [37]) are also shown in Fig. 9.

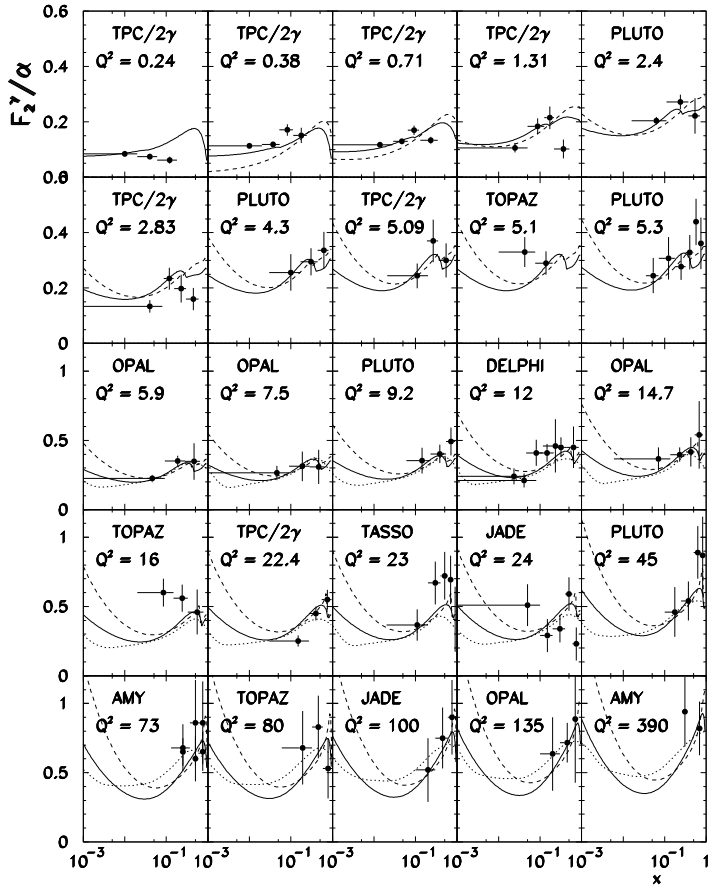

Fig. 9. Compilation [10] of all existing data on F_2^γ in comparison to predictions of the PDF parametrizations in [33, 34, 37].

4.3 Parton Distribution Functions of the Virtual Photon

We now turn to a discussion of the virtual photon structure. Some old data from the PLUTO collaboration [25] exist, which show the structure function of a target photon with virtuality $P^2 \simeq 0.4$ GeV^2 at $Q^2 \simeq 5$ GeV^2. At HERA information about the structure of the virtual photon has been obtained by two different methods [23, 24]. One was by tagging photons with a mean virtuality of $P^2 \simeq 10^{-5}$ GeV^2 with the electron calorimeter of the luminosity system. Another method was to use the beam-pipe calorimeter to tagg photons with a range in virtuality of $0.1 < P^2 < 0.6$ GeV^2. The ratio of the resolved to the direct contribution can be plotted as a function of the photon virtuality P^2, where an experimental definition of the direct and the resolved part of the cross section has to be given. We will come back to this data in section 5, where we calculate one- and two-jet cross sections in NLO for ep scattering under HERA conditions. We will compare the ratios as defined in the experiment with our theoretical predictions.

Here, we concentrate on the construction of the PDF's for a virtual photon. First, we state the LO QPM result for virtual photons, which substitutes the result (80) for real photons. The virtuality P^2 serves as a regulator in this case and in the limit $\Lambda^2 \ll P^2 \ll Q^2$ one obtains [59, 60, 61]

$$q_i^{\gamma^*}(x,Q^2) = 3e_{q_i}^2 \frac{\alpha}{2\pi}\left\{[x^2+(1-x)^2]\ln\frac{Q^2}{x^2P^2} + 6x(1-x) - 2\right\} \quad . \tag{86}$$

The evolution equations in Q^2 for virtual photons and the resulting PDF's are exactly calculable in perturbative QCD in a limited range of photon virtuality, $\Lambda^2 \ll P^2 \ll Q^2$ [60, 61]. The PDF's of the real photon are known for the region $P^2 \ll \Lambda^2$, as described in section 4.2. At HERA, though, the intermediate region $P^2 \simeq \Lambda^2$ is of special interest, as has been noted above. The aim of Glück, Reya and Stratmann (GRS) in [36] and Schuler and Sjöstrand (SaS) in [37] was to construct PDF's for virtual photons, that are valid in the whole P^2-region, i.e. $0 \le P^2 \le Q^2$. We explain the constructions of these PDF's in the following.

4.3.1 The PDF's of GRS Glück, Reya and Stratmann have used for their construction a VMD inspired interpolation between the PDF's of real photons and those valid at $P^2 \gg \Lambda^2$ [36], since the PDF's $f_i^\gamma(x,Q^2,P^2)$ obey evolution equations similar to those of the real photon. The question therefore reduces to finding appropriate boundary conditions at $Q^2 = P^2$. Defining

$$\eta(P^2) \equiv \frac{m_\rho^4}{(m_\rho^2+P^2)^2} \quad , \tag{87}$$

where $m_\rho^2 = (0.77)^2$ GeV^2 refers to some effective mass in the vector-meson propagator, PDF's valid for all values of P^2 are defined as

$$f^{\gamma^*}(x,Q^2=P^2,P^2) = \eta(P^2) f_{had}^{\gamma^*}(x,P^2) + [1-\eta(P^2)] f_{pl}^{\gamma^*}(x,P^2) \quad . \tag{88}$$

In this formula, the perturbatively calculable pointlike part $f_{pl}^{\gamma^*}$ is given by the function $q_i^{\gamma^*}(x,Q^2=P^2)$ from equation (86) and $g^{\gamma^*}(x,Q^2=P^2) = 0$ in NLO.

For a LO construction, $f_{pl}^{\gamma^*}(x, Q^2 = P^2) = 0$. These results are for the DIS_γ scheme [33], which is connected to the $\overline{\mathrm{MS}}$-scheme via the transformations

$$\begin{aligned} q_{DIS_\gamma}^{\gamma^*} &= q_{\overline{MS}}^{\gamma^*} + q_i^\gamma(x, Q^2 = m_i^2) \\ g_{DIS_\gamma}^{\gamma^*} &= g_{\overline{MS}}^{\gamma^*} \quad , \end{aligned} \tag{89}$$

where $q_i^\gamma(x, Q^2)$ is given by (80). These transformations are valid only for the NLO distributions, whereas the LO distributions are equal in both schemes. The reason for introducing the DIS_γ scheme was that the differences between the LO and the NLO result are small. The hadronic, non-perturbative input is given by

$$f_{had}^{\gamma^*}(x, P^2) = \kappa \frac{4\pi\alpha}{f_\rho^2} \times \begin{cases} f^\pi(x, P^2) & , \quad P^2 > \mu^2 \\ f^\pi(x, \mu^2) & , \quad 0 \le P^2 \le \mu^2 \end{cases} \tag{90}$$

where $\mu_{LO}^2 = 0.25\,\mathrm{GeV}^2$ and $\mu_{NLO}^2 = 0.3\,\mathrm{GeV}^2$. The function $\kappa(4\pi\alpha/f_\rho^2) f^\pi(x, \mu^2)$ is just the prescription for the boundary conditions at input scale $Q^2 = \mu^2$ for real photons. As one observes,

$$\eta(P^2 = 0) = 1 \qquad \text{and} \qquad 1 - \eta(P^2 \gg \Lambda^2) \to 1 \quad . \tag{91}$$

Thus, the usual real photon PDF is regained for $P^2 = 0$, whereas the perturbatively calculable part dominates for $P^2 \gg \Lambda^2$. The number of flavors is set to $N_f = 3$. The heavy quark sector $(c, b, \ldots)$ is supposed to be added as predicted by perturbation theory of fixed order with no active c and b quarks in the proton and photon PDF's. In LO this amounts to adding the processes $\gamma^* g \to c\bar{c}$ and $\gamma^* g \to b\bar{b}$ to the cross section, keeping $m_c, m_b \neq 0$.

In [27] GRS have provided PDF's of the virtual photon in a parametrized form in LO that can be conveniently used for numerical calculations. The input scale is $Q_0 = 0.5$ GeV and the restriction $P^2 \le Q^2/5$ is implemented as to fulfill the condition $P^2 \ll Q^2$. We show the x-distribution for the up-quark at a scale of $Q^2 = 50\ \mathrm{GeV}^2$ for three different values of P^2, namely $P^2 = 0, 1$ and $5\ \mathrm{GeV}^2$ in Fig. 10 a. As one observes, the distribution decreases with increasing P^2. For $P^2 = 0$ the real photon PDF of Glück, Reya, Vogt [33] is reproduced exactly and the curves fall on top of each other. The use of the $\overline{\mathrm{MS}}$ scheme for the LO distributions has to be explained. The authors GRS and SaS both give distributions in the DIS_γ scheme, but their schemes differ slightly. SaS actually also give $\overline{\mathrm{MS}}$ distributions. In order to make the results comparable, we treat the distributions of GRS formally as in NLO and use the transformation equations (89) also for the GRS LO distributions.

It should be mentioned, that GRS have calculated NLO distributions in [27]. Distinct differences occur for larger P^2 and $x > 10^{-3}$ which is mainly due to the different NLO perturbative boundary condition at $P^2 = Q^2$, which does not exist for the real photon structure function.

4.3.2 The PDF's of SaS Schuler and Sjöstrand represent the solution of the inhomogeneous evolution equations of the real photon as a sum of a perturbative

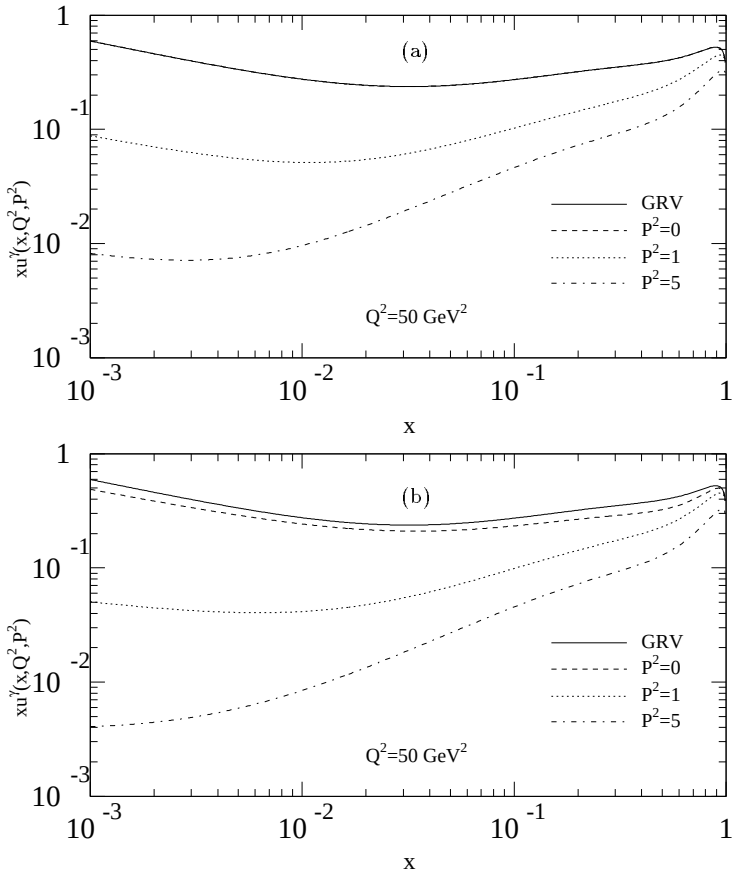

Fig. 10. (a) The GRS LO prediction in the $\overline{\rm MS}$ scheme for the up-distribution of a virtual photon at $Q^2 = 50\,\mathrm{GeV}^2$ and various fixed values of P^2. For comparison, the LO prediction of GRV for a real photon [33] is shown, which lies exactly on top of the PDF of GRS for $P^2 = 0$; (b) SaS1M PDF's.

and a non-perturbative term [37]

$$f^{\gamma}(x,Q^2) = \sum_V \frac{4\pi\alpha}{f_V^2} f^{\gamma,VMD}(x,Q^2;Q_0^2) + \frac{\alpha}{2\pi}\sum_i 2e_{q_i}^2 \int_{Q_0^2}^{Q^2} \frac{dk^2}{k^2} f^{\gamma,q\bar{q}}(x,Q^2;k^2) \quad . \tag{92}$$

Here, $Q_0^2 \geq \Lambda^2$ is the input scale for the non-perturbative solution $f^{\gamma,VMD}$ of the homogeneous evolution equations, which can be interpreted as a fluctuation of the real photon into vector-mesons. The second term represents the anomalous perturbative solutions of the $\gamma \to q\bar{q}$ fluctuations, where k^2 is the virtuality of the $q\bar{q}$-pair, which has a continuous spectrum. As noted above, the evolution equations of the PDF's of the virtual photon can be exactly calculated in the range $Q_0^2 \ll P^2 \ll Q^2$. For real photons in the region of $P^2 \ll Q_0^2$, the PDF's

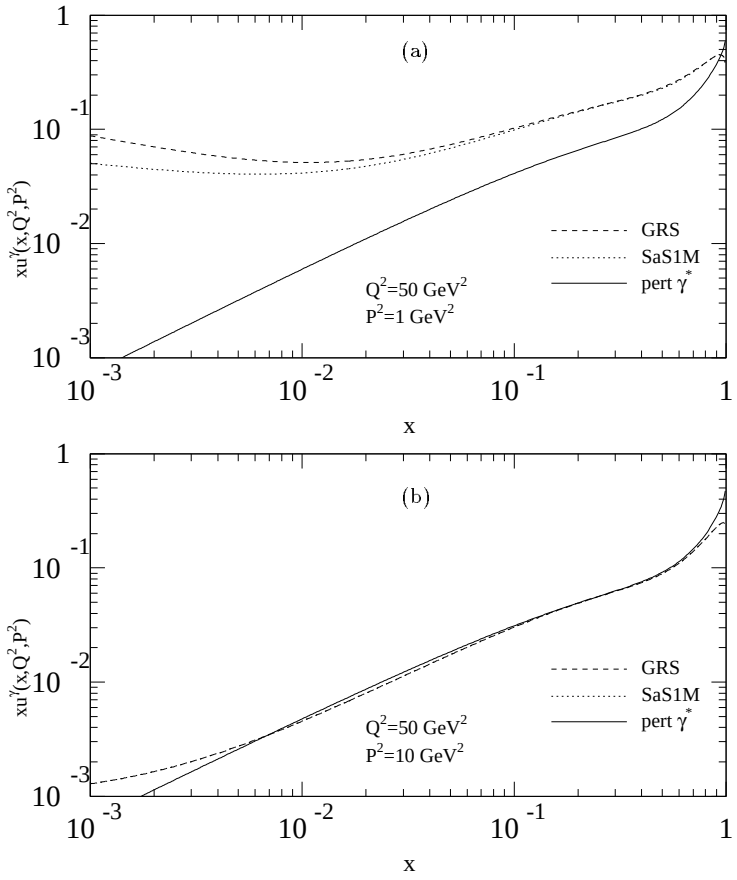

Fig. 11. (a) Comparison between the GRS and SaS1M LO predictions for the up-distribution of a virtual photon at $Q^2 = 50$ GeV^2 and $P^2 = 1.0$ GeV^2 and the purely perturbative contribution in the $\overline{\rm MS}$ scheme; (b) $P^2 = 10$ GeV^2. The distribution for GRS lies exactly atop of the SaS1M curve.

are given by equation (92). To obtain results valid for the whole P^2 region, SaS make use of the dispersion relation

$$f^{\gamma^*}(x,Q^2,P^2) = \frac{\alpha}{2\pi}\sum_i 2e_{q_i}^2 \int_0^{Q^2} \frac{dk^2}{k^2}\left(\frac{k^2}{k^2+P^2}\right)^2 f^{\gamma,q\bar{q}}(x,Q^2;k^2) \quad . \qquad (93)$$

This model provides the correct behaviour for both $P^2 \to 0$ and the above described perturbative region. Now, the region of low k^2 can be associated with the discrete set of vector-mesons, so that by introducing the cut-off Q_0^2 in the k^2-integration SaS obtain [37]

$$f^{\gamma^*}(x,Q^2,P^2) \quad = \quad \sum_V \frac{4\pi\alpha}{f_V^2}\left(\frac{m_V^2}{m_V^2+P^2}\right)^2 f^{\gamma,VMD}(x,Q^2;\tilde{Q}_0^2)$$

$$+ \quad \frac{\alpha}{2\pi} \sum_i 2e_{q_i}^2 \int_{Q_0^2}^{Q^2} \frac{dk^2}{k^2} \left(\frac{k^2}{k^2 + P^2} \right)^2 f^{\gamma, q\bar{q}}(x, Q^2; k^2) \quad . (94)$$

These parton distributions are the solutions of the inhomogeneous evolution equations of the virtual photon. Note, that the input scale for the VMD PDF's has been shifted from $Q_0^2 \to \tilde{Q}_0^2$ with $Q_0^2 < \tilde{Q}_0^2$. This is motivated by a study of the evolution equations in [63], which shows that the evolution for virtual photons starts later in Q^2.

The authors SaS have provided the PDF's of the virtual photon in a parametrized form in LO for $N_f = 4$ in [37] for two different input scales, namely $Q_0 = 0.6$ GeV and $Q_0 = 2$ GeV. We will use the lower scale in this work. In contrast to the GRS parametrization, the c quark is included as a massless flavor in the PDF that undergoes the usual evolution as the other massless quarks except for a shift of the starting scale Q_0. We show the up-quark distribution in comparison to the ones obtained by GRS in Fig. 10 b for the same scale and P^2 values as in Fig. 10 a. They show roughly the same behaviour and deviate only in the small x region. For $P^2 = 0$, the GRV [33] distribution of the real photon is recovered more or less. We have used the SaS1M parametrization, which is given in the $\overline{\text{MS}}$ scheme, to make the SaS results comparable with the GRS distributions.

In section 3.5 we have calculated the part of the hard cross section for an incoming virtual photon that couples directly to the subprocess, leading to the logarithmic terms $\ln(P^2/Q^2)$. The logarithm is absorbed into the PDF of the virtual photon. As we suspect from the above discussion, the PDF of the virtual photon should reduce approximately to the perturbatively calculable contribution (72) in the region of large P^2. Thus, comparing the contribution (72) directly with the, say, up-quark distribution for virtual photons should lead to results of the same order of magnitude for large P^2. They cannot give exactly the same results, since the perturbative part of the u-quark distribution is evolved with help of the evolution equations. In Fig. 11 a, b we show the purely perturbative contribution in comparison to the u-quark distributions GRS and SaS1M at $Q^2 = 50$ GeV^2 for the two values $P^2 = 1$ GeV^2 and $P^2 = 10$ GeV^2 in the $\overline{\text{MS}}$-scheme. As one observes, the perturbative solution and the u-distribution coincide rather well for the larger P^2 value, especially in the large x range, with a slight enhancement of the perturbative curve near $x = 1$.

5 Electron-Proton Scattering at HERA

We come to an analysis of inclusive jet-rates in electron-proton scattering for slightly off-shell photons. After the introduction of the hadronic cross section, using the calculated partonic cross sections of section 3, we explain the matching of theoretical and experimental jet definitions. Afterwards, some numerical tests are discussed, and finally numerical results for one- and two-jet inclusive cross sections are given. A comparison with present HERA data is shown.

5.1 Hadronic Cross Section

We write electron-proton scattering for the production of two jets as

$$e(k) + P(p) \to e(k') + \mathrm{Jet}_1(E_{T_1}, \eta_1) + \mathrm{Jet}_2(E_{T_2}, \eta_2) + X \quad . \tag{95}$$

Here, k and p are the momenta of the incoming electron and proton, respectively, and k' is the momentum of the outgoing electron. The jets in the final state are characterized by their transverse momenta E_{T_i} and rapidities η_i, which are observables in an experimental setup. The interaction of the electron with the proton is mediated by an electroweak vector boson with four-momentum $q \equiv (k - k')$ and virtuality $P^2 \equiv (-q^2)$. The process is dominated by a photon, especially for the small virtualities under consideration. We therefore concentrate on the photon and neglect contributions from the other electroweak bosons. The phase space of the electron can be parametrized by the variables $y \equiv (pq)/(pk)$ and P^2. In the case of small virtualities $P^2 \ll q_0^2$, where q_0 is the energy of the virtual photon, y gives the momentum fraction of the electron energy E_e, carried away by the virtual photon, so $y \simeq q_0/E_e$. The c.m. energy of the hadronic system is given by $s_H = (p+k)^2$, whereas the c.m. energy of the photon-proton subsystem is $W^2 = (p+q)^2$.

We have discussed the factorization of hard and soft regions of the electron-proton cross section in section 2. The hadronic cross section $d\sigma^H$ may be written as a convolution of the hard scattering process $d\sigma_{e/k}$ with the PDF of the proton $f_{k/P}(x_b)$, where x_b is the momentum fraction of the parton from the proton:

$$d\sigma^H(s_H) = \sum_k \int dx_b \; f_{k/P}(x_b) d\sigma_{e/k}(x_b s_H) \quad . \tag{96}$$

The hard process is given by the squared matrix element $|\mathcal{M}|^2$, which has to be divided by the flux factor $2 s_H x_b$ and multiplied by the phase space of n final state particles of the subprocess and the electron, $d\mathrm{PS}^{(n+1)}$:

$$d\sigma_{e/k} = \frac{1}{4 s_H x_b} |\mathcal{M}|^2 d\mathrm{PS}^{(n+1)} \quad . \tag{97}$$

The matrix element $|\mathcal{M}|^2$ separates into the hadron tensor $H^{\mu\nu}$ and the lepton tensor $L_{\mu\nu} = 4(k_\mu k'_\nu - k'_\mu k_\nu - g_{\mu\nu} k k')$:

$$|\mathcal{M}|^2 = \frac{4\pi\alpha}{P^4} L_{\mu\nu} H^{\mu\nu} \quad . \tag{98}$$

The constant α is the electromagnetic coupling constant. The separation of the phase space into a part depending only on the electron dL and a part depending only on the final state particles of the subprocess $d\mathrm{PS}^{(n)}$ is easily achieved by inserting a delta function for the intermediate virtual photon and gives

$$d\mathrm{PS}^{(n+1)} = dL \, d\mathrm{PS}^{(n)} \qquad \text{with} \qquad dL = \frac{P^2}{16\pi^2} \frac{d\phi}{2\pi} \frac{dy dP^2}{P^2} \quad . \tag{99}$$

Here ϕ is the azimuthal angle of the outgoing electron. This degree of freedom can be integrated out, yielding

$$\frac{1}{4P^2} \int \frac{d\phi}{2\pi} L_{\mu\nu} H^{\mu\nu} = \frac{1 + (1-y)^2}{2y^2} H_g + \frac{4(1-y) + 1 + (1-y)^2}{2y^2} H_L \quad , \tag{100}$$

with the definitions $H_g \equiv -g^{\mu\nu} H_{\mu\nu}$ and $H_L \equiv (4P^2)/(s_H y)^2 p^\mu p^\nu H_{\mu\nu}$. Since we will consider the range of small photon virtualities P^2 throughout this work, the contribution H_L proportional to P^2 will be neglected. We approximate the spectrum of the virtual photons by

$$\frac{df_{\gamma/e}(y)}{dP^2} = \frac{\alpha}{2\pi} \frac{1+(1-y)^2}{y} \frac{1}{P^2} \quad , \tag{101}$$

which is the unintegrated Weizsäcker-Williams [8] formula. For later use we define the virtuality $P^2_{eff} = 0.058$ GeV^2. By inserting P^2_{eff} into the unintegrated Weizsäcker-Williams formula, we obtain the value for the Weizsäcker-Williams formula integrated in the region $P^2_{min} \leq P^2 \leq P^2_{max} = 4$ GeV^2 using the minimum photon virtuality $P^2_{min} := \frac{m_e^2 y^2}{1-y}$. In this way, we can reproduce the $P^2 \simeq 0$ results.

Defining the partonic cross section

$$d\sigma_{\gamma/k} = \frac{1}{4 x_b y s_H} H_{\gamma/k} d\mathrm{PS}^{(n)} \quad , \tag{102}$$

the hard scattering (97) integrated over the angle ϕ can be written as

$$d\sigma_{e/k} = d\sigma_{\gamma/k} df_{\gamma/e}(y) dy \quad . \tag{103}$$

As discussed in the previous section, a photon with moderate virtuality interacts with a proton not only as a point-like particle, but also via its hadronic content. The hadronic structure of the photon is described by a PDF $f_{\gamma/l}(x_a)$, introducing the new variable x_a that gives the momentum fraction of the parton from the photon. To simplify the notation, the case of a direct photon is included into the PDF of the photon via the delta function $f_{\gamma\gamma}(x_a) = \delta(1-x_a)$. Summarizing the above results, the hadronic cross section $d\sigma^H(s_H)$ may be written as a convolution of the hard scattering $d\sigma_{k/l}$ with the PDF of the photon $f_{\gamma/l}(x_a)$ and of the proton $f_{k/P}(x_b)$, multiplied by the photon spectrum $df_{\gamma/e}(y)$:

$$d\sigma^H = \sum_{k,l} \int dx_a dx_b dy \; df_{\gamma/e}(y) \; f_{\gamma/l}(x_a) d\sigma_{l/k} f_{k/P}(x_b) \quad . \tag{104}$$

The hard cross section $d\sigma_{kl}$ now describes the interactions of the partons from the photon (and the photon itself) with the partons from the proton and is given by the trace of the hadron tensor, multiplied with the phase space of the final state particles, divided by the flux factor:

$$d\sigma_{l/k} = \frac{1}{4 x_a x_b y s_H} H_{l/k} d\mathrm{PS}^{(n)} \quad . \tag{105}$$

The factorization (104) is visualized in Fig. 12.

For electron-proton scattering, the SR case, in which the virtual photon couples directly to the partons from the proton, and the DR case, in which the photon serves as a source of partons, are present. As mentioned in section 2, the matrix elements cannot be integrated over the whole region of phase space in

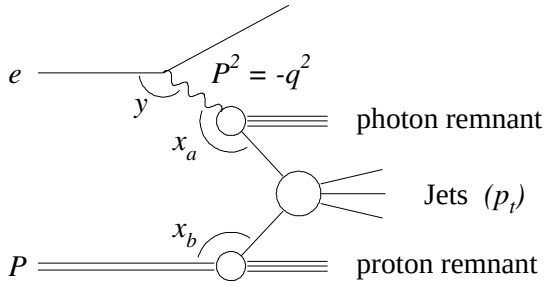

Fig. 12. Factorization of hard and soft contributions in electron-proton scattering.

NLO. A cut-off has to be introduced that separates the singular from the finite regions. The results for the integration over the singular regions were given in section 3 and the factorization of singular terms has been discussed. Although the calculation of the NLO matrix elements is straightforward, especially using algebraic programs like REDUCE [64], the results for the full matrix elements are too cumbersome to be stated here. For both, the SR and the DR cross section, we have a set of two-body contributions and a set of three-body contributions. Each set is completely finite, as all singularities have been canceled or absorbed into PDF's. Each part depends separately on the phase space slicing parameter y_c. The analytic calculations are valid only for very small y_c, since terms $\mathcal{O}(y_c)$ have been neglected in the analytic integrations. As explained in section 3.3, the two separate pieces have no physical meaning. When the two-body and three-body contributions are superimposed to yield a suitable inclusive cross section, as for example the inclusive one- or two-jet cross section, the dependence on the cut-off y_s will cancel. This has been checked explicitly and will be demonstrated in section 5.4.

We now come to the kinematics of electron-proton scattering. We first concentrate on the SR cross section, for which the kinematics is most easily treated in the c.m. system of the virtual photon and the proton, where for the three-vectors $\mathbf{p} + \mathbf{q} = \mathbf{0}$. We denote the momenta of the final state particles as p_1 and p_2, which can be expressed by their transverse momenta $E_{T_1} = E_{T_2} = E_T$ and their rapidities η_1 and η_2 in the $\gamma^* P$ c.m. system by $p_i = E_T(\cosh\eta_i, 0, 0, \sinh\eta_i)$ (remember that the azimuthal angle has been integrated out). From energy and momentum conservation one obtains

$$W = E_T(e^{-\eta_1} + e^{-\eta_2}) \quad , \tag{106}$$

$$y = \frac{W^2 + P^2}{s_H} \quad , \tag{107}$$

$$x_b = 1 + \frac{2W}{W^2 + P^2} E_T(\sinh\eta_1 + \sinh\eta_2) \quad . \tag{108}$$

The phase space, including the integration over x_b and y, can be expressed as

$$d\mathrm{PS}^{(2)} dx_b dy = \frac{W^2}{W^2+P^2} \frac{2E_T}{s_H} \frac{dE_T}{(2\pi)^2}\, d\eta_1 d\eta_2 \quad . \tag{109}$$

The Mandelstam variables s, t and u are defined as

$$\begin{aligned} s &= (p_b+q)^2 = (p_1+p_2)^2 \quad , \\ t &= (q-p_1)^2 = (p_b-p_2)^2 \quad , \\ u &= (q-p_2)^2 = (p_b-p_1)^2 \quad . \end{aligned} \tag{110}$$

In the DR case, the rapidities of the final state partons η_1' and η_2' are expressed in the c.m. system of the two partons and have to be boosted into the photonic c.m. system via

$$\eta_i = \eta_i' + \frac{1}{2} \ln x_a \qquad \text{for} \quad i = 1,2 \quad . \tag{111}$$

Inserting these transformed rapidities into the above equations (106)–(109) the correct formulæ in the case of the resolved photon for x_a, x_b, y and W, now containing η_i', are obtained. For $x_a = 1$, which defines the SR case, the two systems are identical and $\eta_i' = \eta_i$.

For a comparison with HERA data the rapidities and transverse momenta have to be transformed from the photonic c.m. system to the HERA laboratory system. The calculation of the SR and DR cross sections proceed as for real photoproduction, i.e. the transverse momentum (q_T) of the virtual photon and other small terms proportional to P^2 are neglected so that the virtual photon momentum is in the direction of the incoming electron and $q_0 = E_e y$. The transformation from the c.m. system into the HERA laboratory system is as for real photoproduction:

$$\eta_i^{lab} = \eta_i + \frac{1}{2} \ln \frac{E_p}{y E_e} \quad . \tag{112}$$

5.2 Snowmass Jet Definition

The factorization of hard and soft regions in the hadronic cross section has been discussed so far for the initial state. The non-perturbative and not calculable regions are parametrized through the PDF's of the hadron or the resolved photon. A similar problem occurs in the final state. The partons that are emitted from the subprocess cannot be observed directly due to the confinement of color charge. The hadronization of partons into single hadrons in the final state can be described, similarly to hadrons in the initial state, by fragmentation functions. Another possibility is the observation of a shower built from a large number of hadrons without resolving the specific type of hadrons emitted. One then has to define jets in order to identify the hadron showers with individual partons or their combinations from the subprocess. The combination of hadrons into jets is done by cluster algorithms, where jet definitions can be implemented. The jet definitions should fulfill a number of criteria [65], such as they should be simple to implement in theory and experiment, be well defined and yield finite cross

sections in any order of perturbation theory and give cross sections that are more or less insensitive to the hadronization processes.

Looking at the theoretical side of inclusive two-jet cross sections, in LO there is a one-to-one correspondence between the parton from the subprocess and the jet in the final state. Therefore the theory is not sensitive to any specific cluster algorithm used in the experiment. This is not sensible, because the experimental results depend strongly on the used algorithm. Only in NLO can one implement certain jet definitions on the theoretical side, because the jet can obtain a substructure due to the nearly collinear radiation of a parton in the final state.

Several jet definitions have been proposed to date, one of the first being the (ϵ, δ) criterion of Sterman and Weinberg [66] (see also [50]). We will adopt the jet definition of the Snowmass meeting [67]. According to this definition, two partons i and j are recombined, if $R_{i,J} < R$, where $R_{i,J} = \sqrt{(\eta_i - \eta_J)^2 + (\phi_i - \phi_J)^2}$ and η_J, ϕ_J are the rapidity and the azimuthal angle of the combined jet respectively, defined as

$$E_{T_J} = E_{T_1} + E_{T_2} \quad , \tag{113}$$

$$\eta_J = \frac{E_{T_1}\eta_1 + E_{T_2}\eta_2}{E_{T_J}} \quad , \tag{114}$$

$$\phi_J = \frac{E_{T_1}\phi_1 + E_{T_2}\phi_2}{E_{T_J}} \quad . \tag{115}$$

The cone-radius R is chosen as in the experimental analysis. Thus, two partons are considered as two separate jets or as a single jet depending on whether they lie outside or inside the cone with radius R around the jet momentum. In NLO, the final state may consist of two or three jets. The three-jet sample contains all three-body contributions, which do not fulfill the cone condition. The rapidities used for the cone constraint are evaluated in the HERA laboratory system.

5.3 Numerical Input

We now describe the input for the numerical calculations. We have chosen the CTEQ3M proton structure function [68] which is a NLO parametrization in the $\overline{\text{MS}}$ scheme, with $\Lambda^{(4)}_{\overline{MS}} = 239$ MeV. This Λ value is also used to calculate α_s from the two-loop formula

$$\alpha_s(\mu) = \frac{12\pi}{(33 - 2N_f)\ln\frac{\mu^2}{\Lambda^2}}\left(1 - \frac{6(153 - 19N_f)}{(33 - 2N_f)^2}\frac{\ln(\ln\frac{\mu^2}{\Lambda^2})}{\ln\frac{\mu^2}{\Lambda^2}}\right) \quad . \tag{116}$$

We use this formula for both the LO and NLO calculations. In the case of photoproduction, the scale μ is set equal to the transverse momentum of the jets, since this is the only hard scale present in the interactions. Here, $P^2 \ll E_T^2$, so that we also set $\mu = E_T$. Equivalently, the factorization scales are chosen to be $M_\gamma = M_p = E_T$.

For the PDF's of the virtual photon we choose either the GRS [36] set or the SaS1M set [37]. Both sets are given in parametrized form for all scales M_γ^2 so that they can be applied without repeating the computation of the evolution. As mentioned in section 4, both sets are given only in LO, i.e. the boundary conditions

for $P^2 = M_\gamma^2$ and the evolution equations are in LO. Since neither of the two PDF's is constrained by empirical data from scattering on a virtual photon target we consider these LO distribution functions as sufficient for our exploratory studies on jet production and treat them as if they were obtained in NLO. As noted in section 4, the heavy quarks are supposed to be added as predicted by fixed order perturbation theory with no active heavy quarks in the PDF's of the proton and the photon. Since in this section we are primarily interested in studying the sum of the direct and resolved contributions and the influence of the consistent subtractions of the NLO direct part we refrain from adding the LO or NLO cross sections for direct heavy quark production as suggested in [27, 36]. So, our investigations in connection with the GRS parametrization of the virtual photon PDF are for a model with three flavors only. For consistency we take also $N_f = 3$ in the NLO corrections and in the two-loop formula for α_s. Of course, the proton PDF has been obtained for $N_f = 4$. In comparison to the GRS parametrization, we studied the relevant cross sections also with the virtual photon PDF's of SaS [37], which are for $N_f = 4$.

The cross sections we have computed are for kinematical conditions as in the HERA experiments, for which positrons of $E_e = 27.5$ GeV which collide with protons of $E_p = 820$ GeV. To have the equivalent conditions as in the ZEUS analysis we choose the constraints $y_{min} = 0.2$ and $y_{max} = 0.8$ for the variable occuring in the unintegrated Weizäcker-Williams approximation. The cone radius is set to $R = 1$.

5.4 Numerical Tests

Since the separation of the two-body and three-body contributions with the slicing parameter y_c is a purely technical device in order to distinguish the phase space regions where the integrations are done analytically from those where they are done numerically, the sum of the two- and three-body contributions should be independent from y_c. The dependence of the two-body contributions on the slicing parameter is logarithmic, giving rise to $(\ln y_c)$- and $(\ln^2 y_c)$-terms. The parameter y_c has to be quite small to guarantee that the approximations in the analytical calculations are valid. Typically, y_c is of the order of 10^{-3}, forcing the two-body contributions to become negative, whereas the three-body cross sections are large and positive. In Fig. 13 a, b we have checked for two different values of P^2, by varying y_c between 10^{-4} and 10^{-2}, that the superimposed two- and three-body contributions are independent of y_c for the inclusive single-jet cross sections integrated over the whole kinematically allowed η region for fixed $E_T = 20$ GeV. Only the SR contribution is tested, since the insensitivity of the DR contributions on y_c has been checked in [13, 22].

Furthermore, we have explicitly checked that the SR one- and two-jet cross sections for virtual photons are in perfect agreement with the ones from real photoproduction given in [14, 13] by integrating the virtuality numerically over the region of small P^2 with $P^2_{min} \leq P^2 \leq 4\ \mathrm{GeV}^2$. The main contribution to the cross section comes from the lower integration boundary, where the dependence of the matrix elements on P^2 is small.

Both, the y_c-dependence test and the comparison with the results from [14, 13], give us confidence that our computer program for the calculation of jet

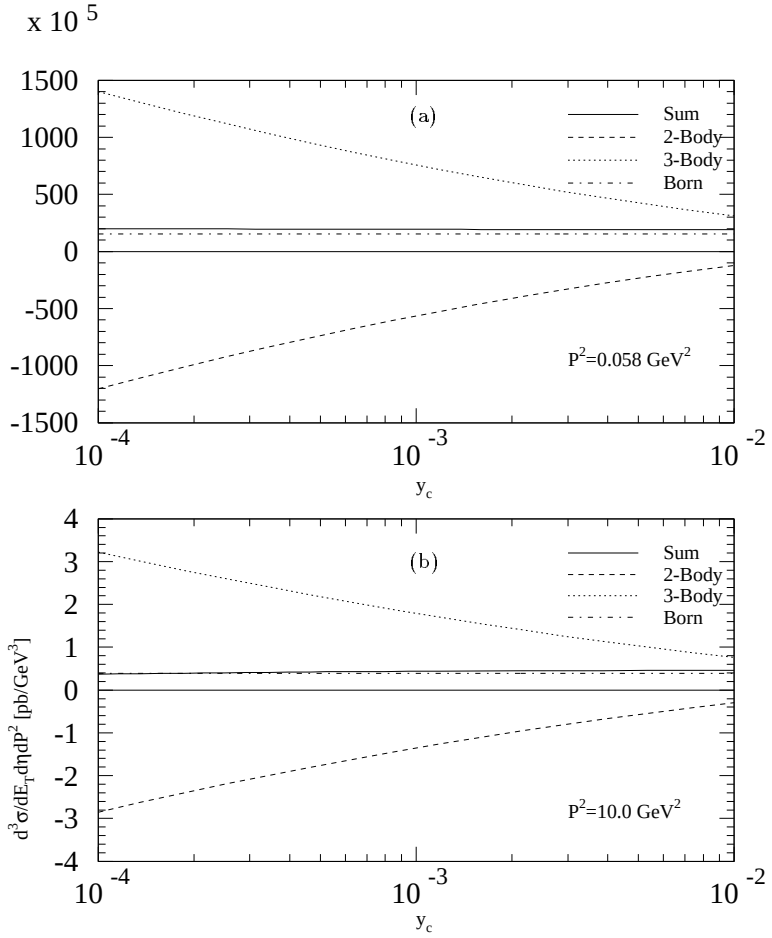

Fig. 13. (a) Single-jet inclusive cross section integrated over the physical η region for $E_T = 20$ GeV and for the virtuality $P^2 = 0.058$ GeV^2 as a function of the slicing parameter y_c. The solid line gives the sum of the two- and the three-body contributions; (b) $P^2 = 10.0$ GeV^2.

cross sections in electron-proton scattering yields reliable results. It is interesting now to study the scale dependences of the LO and NLO cross sections. The relevant scales are the renormalization scale μ, the factorization scale for the virtual photon M_γ and that for the proton M_p. Since the dependence on these scales should vanish in an all-order calculation, we expect the dependences to be reduced by going from LO to NLO.

Of special interest is the dependence of the cross section on the factorization scale M_γ, which comes from the factorization of the photon initial state singularities. The dependence is logarithmic, since terms proportional to $\ln(M_\gamma^2/P^2)$ have been subtracted from the NLO cross section for the direct virtual photon, as indicated in equation (72). The dependence of the NLO direct single-jet inclusive cross section, integrated over the region $\eta \in [-1.875, 1.125]$ for $E_T = 7$ GeV, on the parameter M_γ/E_T for two different values of P^2 is shown in Fig. 14

a, b as the dashed curve. It is compared to the resolved virtual photon contribution in LO, which gives the dotted curve. It is sufficient to use the LO matrix elements, since the main M_γ dependence of the resolved contribution stems from the dependence of the photon PDF on the negative logarithm $-\ln(M_\gamma^2/P^2)$. For the comparison we used the SaS1M parametrization of the virtual photon, which is given in the $\overline{\rm MS}$ scheme. As one can see from the Fig. 14 a, b, the dependences on the logarithms of the direct and the resolved contributions cancel rather well in the sum.

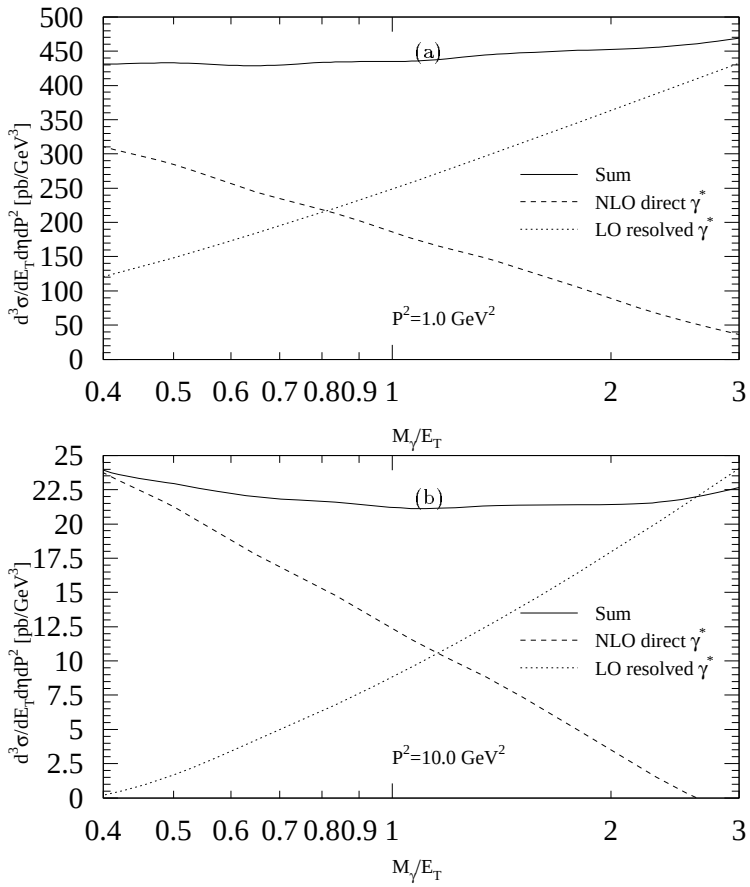

Fig. 14. (a) Single-jet inclusive cross section integrated over $\eta = [-1.875, 1.125]$ for $E_T = 7$ GeV and for the virtuality $P^2 = 1.0$ GeV^2 as a function of the scale parameter M_γ/E_T. The $\overline{\rm MS}$-SaS1M parametrization with $N_f = 4$ is chosen. The solid line gives the sum of the NLO direct and LO resolved virtual photon cross sections; (b) $P^2 = 10.0$ GeV^2.

Finally, we study the renormalization scale dependence of the NLO corrections as compared to the LO cross section. We consider only the SR contributions, since the DR have been tested and shown to have a reduced scale dependence in [13, 22]. In Fig. 15 a, b we have plotted the one-jet inclusive cross

section integrated over $\eta \in [-1.875, 1.125]$ for $E_T = 7$ GeV and $P^2 = 1, 10\,\mathrm{GeV}^2$. We have used the two-loop formula for α_s also in the LO calculation for better comparison. For $P^2 = 1\,\mathrm{GeV}^2$ the scale dependence of the NLO curve is reduced considerably. At $P^2 = 10\,\mathrm{GeV}^2$ though, the NLO cross section falls off slightly for the smaller scales below $\mu \simeq E_T$. This could be attributed to the fact, that the scale and the virtuality are of the same order in this region and the condition $P^2 \ll Q^2$ required in the construction of the virtual photon PDF begins to become violated. Actually, for a full test of the renormalization scale dependence it would be necessary to vary all scales $\mu = M_\gamma = M_p$ simultaneously, since also the structure functions are renormalization scale dependent. It is an empirical fact, that the scale dependence of the proton structure function is small. The dependence of the photon structure function on the renormalization scale is large, but this can only be accounted for by the resolved contributions. The reduced renormalization scale dependence of the sum of the direct and resolved contributions has already been demonstrated in [13, 22].

5.5 Single-Jet Inclusive Cross Sections

In this section, we present numerical results for inclusive one-jet cross sections as a function of the virtuality P^2. We choose the following notation of the curves as to make the discussion clearer: the SR cross sections shall be denoted as *Dir* (reminding of the direct character of the virtual photon), whereas the DR cross sections are labeled *Res*. In addition, the sum of the SR and DR contributions is shown and labeled *Sum*. Note, that in the case of electron-proton scattering the D component does not exist. As has been calculated in section 3, large logarithmic contributions occur for small photon virtualities for the, direct virtual photon that can be subtracted and absorbed into the PDF of the virtual photon. The SR cross sections, where these logarithmic terms have been subtracted, are specified by the index s, giving the contributions Dir_s. All plots in this section are taken from ref. [26].

We first concentrate on predictions with the PDF's of GRS. In Fig. 16 a, b, c, the results for $d^3\sigma/dE_T d\eta dP^2$ are shown as a function of E_T integrated over η in the interval $-1.125 \leq \eta \leq 1.875$, which are the boundaries employed in the ZEUS analysis [23]. We show results for the the three values of $P^2 = 0.058, 0.5$ and 1 GeV^2. For all three P^2 the cross section is dominated by the Res component at small E_T. Near $E_T = 20$ GeV the Dir_s contribution is of the same magnitude as the Res cross section. The sum of the cross sections as a function of P^2 falls off nearly uniformly in the considered E_T range with increasing P^2. This decrease is stronger for smaller E_T.

Next, we studied the η distribution of the Dir_s contribution at fixed $E_T = 7$ GeV and the same P^2 values as in Fig. 16. The results are shown in Fig. 17 a, b, c, where two approximations are shown, namely the LO cross section and the NLO cross section from [13]. There, $P^2 = 0$ everywhere, except for the unintegrated Weizsäcker-Williams approximation, which leads to a $1/P^2$ dependence. Obviously this approximation is good for $P^2 = 0.058\,\mathrm{GeV}^2$. At the larger P^2 however it overestimates the cross section and should not be used. This means that the P^2 dependence of the Dir_s part, although the strongest

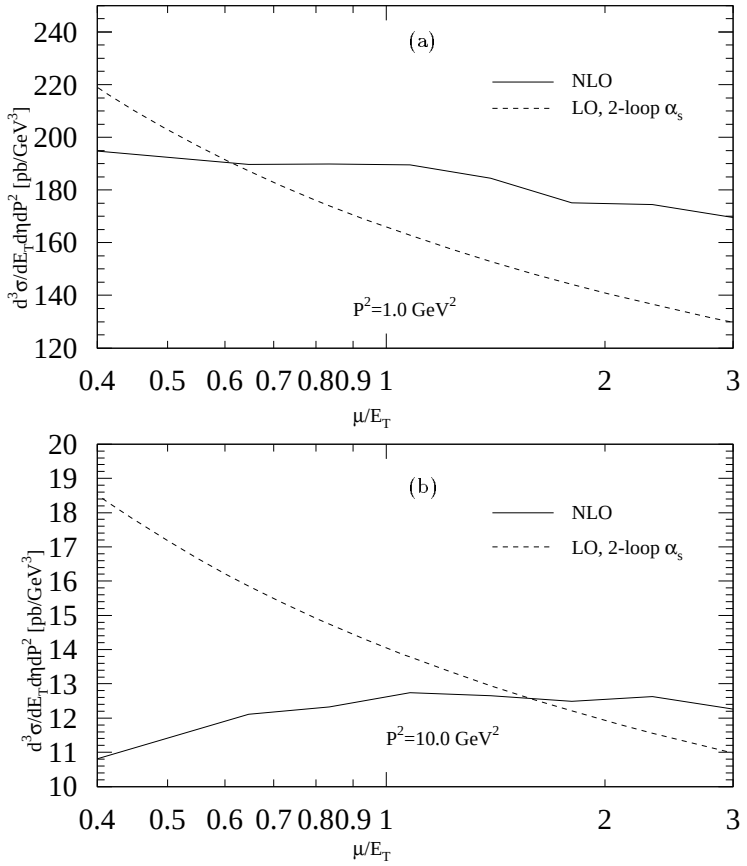

Fig. 15. (a) Single-jet inclusive cross section integrated over $\eta = [-1.875, 1.125]$ for $E_T = 7$ GeV and for the virtuality $P^2 = 1.0$ GeV^2 as a function of the scale parameter μ/E_T. The $\overline{\rm MS}$-SaS1M parametrization with $N_f = 4$ is chosen. The solid line gives the NLO direct prediction, whereas the dashed curve shows the LO cross section; (b) $P^2 = 10.0$ GeV^2.

logarithmic P^2 dependence has been subtracted, should be taken into account. In the sum of the Dir_s and Res cross sections the difference is small as long as the Res part dominates. This holds for the smaller E_T's. The LO prediction is evaluated with the same structure functions and α_s value as the NLO result. It is smaller than the NLO result, which it approaches with increasing P^2. Of course, this finding depends on the chosen value of R because the NLO cross section depends on R, whereas the LO curve does not, as we have already noted before. Estimates of the inclusive cross section with LO calculations can therefore only be trusted for large cone radii.

The results shown so far are for a model with three flavors only and therefore should not be compared to the experimental data except when the contribution from the charm quark is added at least in LO. A more realistic approach is to use the photon PDF's SaS1M [37] which are constructed for four flavors. In Fig. 18 a, b, c results are presented for $d^3\sigma/dE_T d\eta dP^2$ integrated over $\eta \in [-1.125, 1.875]$ as a function of E_T for $P^2 = 0.058, 0.5$ and 1.0 GeV^2. We can compare these curves with the results in Fig. 16a, b, c obtained with the PDF of GRS, where $N_f = 3$. The sum of the Dir_s and Res contributions changes by 10% to 30% in the small E_T region and approximately 50% in the large E_T region. The larger cross section for $N_f = 4$ results mainly from the Dir_s contribution. The direct component is more important for larger E_T than for smaller E_T. Therefore the increase is stronger in the large E_T region.

Of interest are also the rapidity distributions for fixed E_T. These are shown for $E_T = 7$ GeV as a function of η between $-1 \leq \eta \leq 2$ choosing $P^2 = 0.058, 1, 5$ and 9 GeV^2 in Fig. 19 a, b, c, d. We show the subtracted Dir_s cross section, the Res cross section and their sum. The Res component has its maximum shifted to positive η's in contrast to the Dir_s component, as expected. The Dir_s component decreases quite rapidly with increasing η. This stems from the subtraction of the $(\ln P^2/M_\gamma^2)$ terms as can be seen by comparison with the unsubtracted cross section, denoted Dir, in Fig. 19 a, b, c, d. The sum of the resolved and subtracted direct cross section Dir_s is more or less constant for the smaller P^2 values and decreases with increasing η for $P^2 = 5$ and 9 GeV^2.

In section 4.3 we have checked by a direct comparison, that the subtraction term (72) approximates the PDF of the photon rather well for large enough P^2. Thus, for these large virtualities we expect the unsubtracted cross section (Dir) to be the correct one, rather than the sum of the subtracted direct Dir_s and the resolved contributions, at least for small η. The larger P^2, the closer does the full direct cross section Dir approach the sum Res+Dir_s, as can be observed in Fig. 19 a, b, c, d. As we have seen in section 4.3, there still is a deviation of the pure perturbative contribution from the evolved PDF in the small x region. This corresponds to the kinematic region of large η, which is the forward direction of the proton. This deviation is evident in the Fig. 19 a, b, c, d as well; at $P^2 = 9$ GeV^2 the two cross sections differ at $\eta = 2$ by approximately 30 %. Another difference shows up in the backward direction at $\eta = -1$. In this region, which corresponds to the region in the photon PDF where the perturbative component dominates, no deviation is expected. The cause might be the neglection of the transverse momentum q_T of the virtual photon in the calculation of the Dir and Res cross sections, which becomes especially important for larger P^2. Actually,

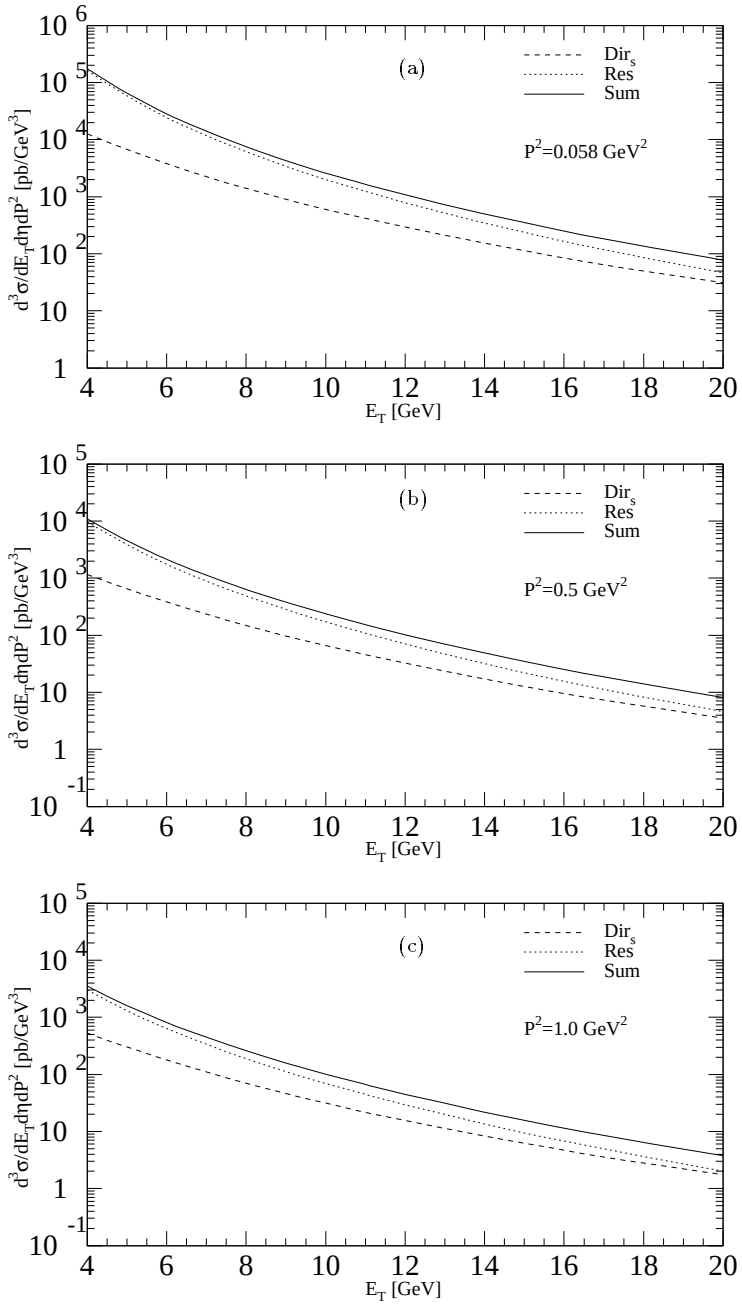

Fig. 16. (a) Single-jet inclusive cross section integrated over $\eta \in [-1.125, 1.875]$ for the virtuality $P^2 = 0.058$ GeV^2. The $\overline{\rm MS}$-GRS parametrization with $N_f = 3$ is chosen. The solid line gives the sum of the subtracted direct and the resolved term; (b) $P^2 = 0.5$ GeV^2; (c) $P^2 = 1.0$ GeV^2

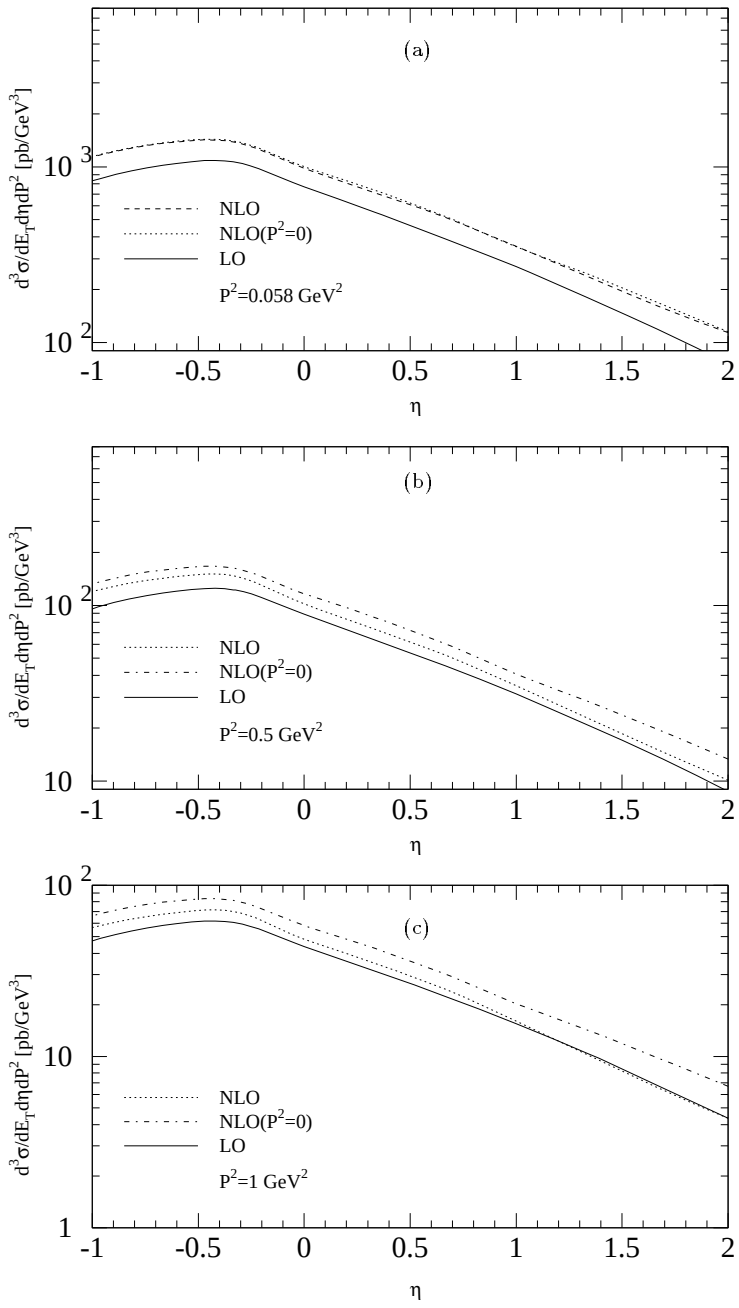

Fig. 17. (a) Single-jet inclusive cross sections for $E_T = 7$ GeV and $P^2 = 0.058$ GeV^2. The $\overline{\text{MS}}$-GRS parametrization with $N_f = 3$ is chosen. Only the SR part with subtraction (Dir$_s$) is plotted. The solid line gives the LO contribution. The dashed curve is the full NLO cross section, whereas the dotted curve gives the NLO cross section, where the NLO matrix elements have no P^2-dependence; (b) $P^2 = 0.5$ GeV^2; (c) $P^2 = 1.0$ GeV^2.

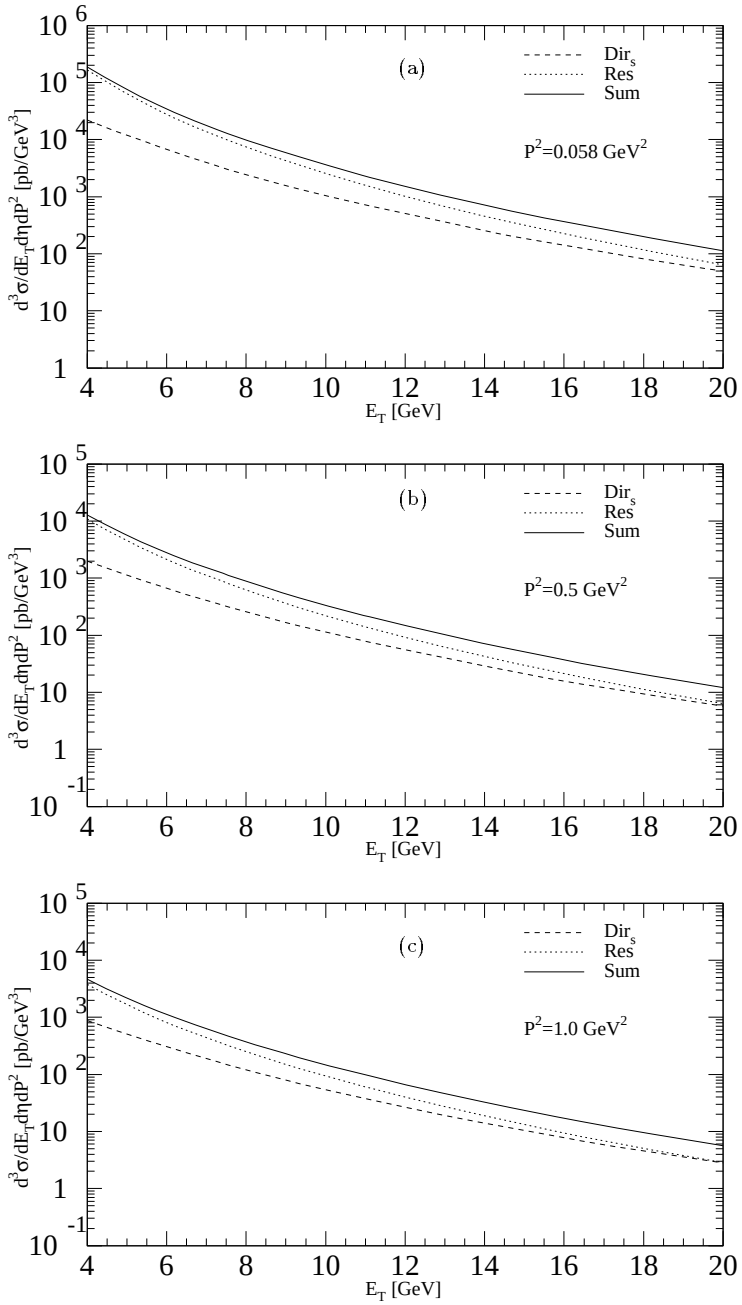

Fig. 18. (a) Single-jet inclusive cross section integrated over $\eta \in [-1.125, 1.875]$ for the virtuality $P^2 = 0.058\ \mathrm{GeV}^2$. The $\overline{\mathrm{MS}}$-SaS1M parametrization with $N_f = 4$ is chosen. The solid line gives the sum of the subtracted direct and the resolved term; (b) $P^2 = 0.5\ \mathrm{GeV}^2$; (c) $P^2 = 1.0\ \mathrm{GeV}^2$.

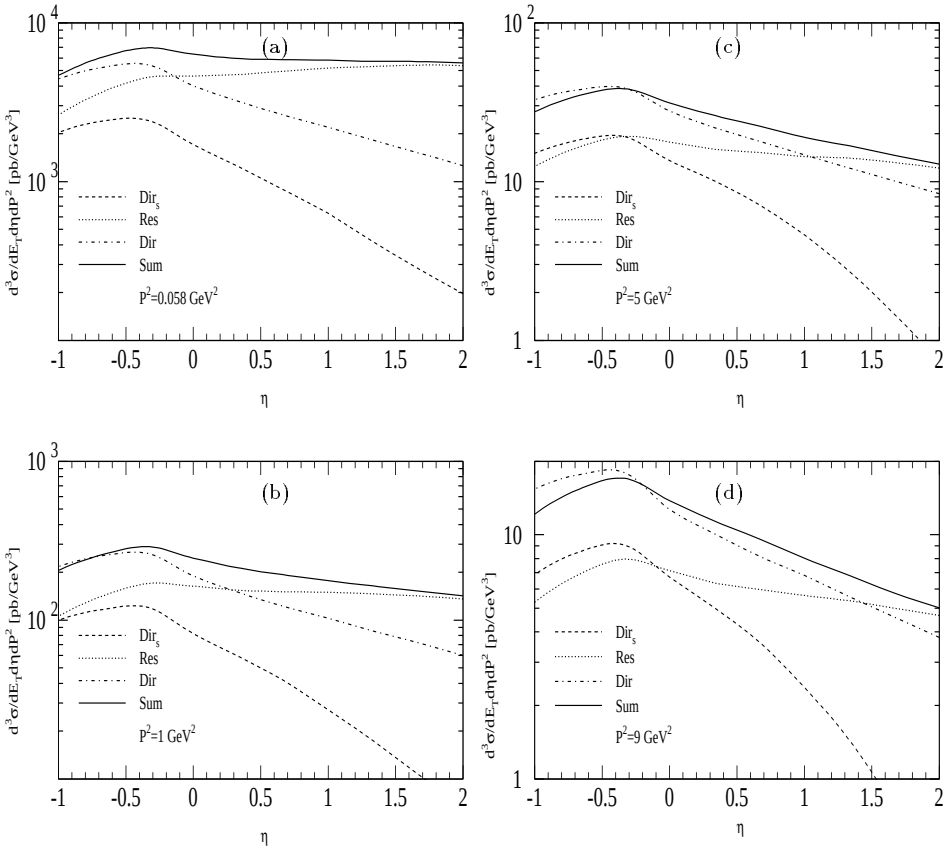

Fig. 19. (a) Comparisons of single-jet inclusive cross sections for $E_T = 7$ GeV and the virtuality $P^2 = 0.058\,\mathrm{GeV}^2$. The $\overline{\mathrm{MS}}$-SaS1M parametrization with $N_f = 4$ is chosen. The solid line gives the sum of the subtracted direct and the resolved term. The dash dotted curve is the direct contribution without subtraction; (b) $P^2 = 1\ \mathrm{GeV}^2$; (c) $P^2 = 5\ \mathrm{GeV}^2$; (c) $P^2 = 9\ \mathrm{GeV}^2$.

looking at Fig. 10 b from section 4, the purely perturbative curve, which will occur in the unsubtracted Dir component, overestimates the up-distribution at $x = 1$, which corresponds to the backward η region. So, also in this region, the sum of the Dir$_s$ and the Res components could still be a better estimate of the cross section, than the Dir component alone.

It is clear that the resolved and the direct cross sections decrease with increasing P^2 for fixed η and E_T. It is of interest to know how the ratio of Res to the Dir cross section behaves as a function of P^2. This has been analyzed in [26]. Apart from the fact that the ratios cannot be measured directly, we found a strong dependence of the ratio on the scheme chosen for the photon PDF and very large corrections when going from LO to NLO. As one can deduce from these results, it is not very sensible to compare the Dir and Res contributions directly. Rather one has to introduce a parameter that experimentally separates

Dir and Res contributions. We will introduce this parameter in the following section.

5.6 Dijet Inclusive Cross Sections

In comparison to single-jet cross sections, dijet cross sections provide a much stronger test of QCD, since they depend on one variable more. We will now present inclusive dijet cross sections $d^4\sigma/dE_T d\eta_1 d\eta_2 dP^2$ as a function of P^2. The variable E_T is defined according to [12, 13] to be the transverse momentum of the measured (trigger) jet, which has rapidity η_1. The second rapidity η_2 is associated with the second jet, where the two measured jets are those with highest E_T in the three-jet sample, i.e. $E_{T_1}, E_{T_2} > E_{T_3}$.

In principle we could predict η distributions similar to those in [12]. Since experimental data on these distributions are not expected in the near future because of limited statistics, we refrain from showing such plots here and present only the E_T distributions integrated over the interval $-1.125 < \eta_1, \eta_2 < 1.875$ following the constraints of the ZEUS analysis [23]. The results for $P^2 = 0.058, 0.5$ and 1.0 GeV^2 are shown in Fig. 20 a, b, c, where the full curve is given by the cross section $d^4\sigma/dE_T d\eta_1 d\eta_2 dP^2$ as a function of E_T integrated over η_1 and η_2 in the specified interval and for $0.2 < y < 0.8$ (the plots in this section are taken from ref. [26]). The functional dependence on E_T does not change as a function of P^2, only the absolute value of the cross section decreases with increasing P^2.

Furthermore we show the so-called *enriched* direct and resolved cross section in Fig. 20. These two contributions are defined with a cut on the variable x_γ^{obs}, which is given by

$$x_\gamma^{obs} \equiv \frac{\sum_i E_{T_i} e^{-\eta_i}}{2yE_e} \quad , \tag{117}$$

where the sum runs over the two highest E_T jets. The variable x_γ^{obs} gives the fraction of the photon energy going into the two measured jets. It is a good estimate of the theoretically defined variable x_a, that defines the fraction of the photon momentum participating in the hard interaction, see Fig. 12. For $x_a = 1$, the photon couples directly to the subprocess, whereas for $x_a < 1$ some of the photon energy goes into the production of a remnant jet, leading to resolved processes. Note, that in LO $x_a = x_\gamma^{obs}$. For experimental considerations, one defines the direct enriched contribution for $x_\gamma^{obs} > 0.75$, whereas the resolved enriched component has $x_\gamma^{obs} < 0.75$. Both enriched cross sections contain contributions from the direct and the resolved part. In Fig. 20 a, b, c the sum of the Dir and Res curves is equal to the full cross section $d^4\sigma/dE_T d\eta_1 d\eta_2 dP^2$ with no cut on x_γ^{obs}. The curves in Fig. 20 are for the GRS parton distributions in the $\overline{\text{MS}}$ scheme. As to be expected, with increasing P^2 the full cross section is more and more dominated by the Dir component, in particular at the larger E_T. This means that the cross section in $x_\gamma^{obs} < 0.75$ decreases stronger with P^2 than in the $x_\gamma^{obs} > 0.75$ region. This could be studied experimentally by measuring the ratio of the two cross sections as a function of P^2 for fixed E_T. This has not been done yet.

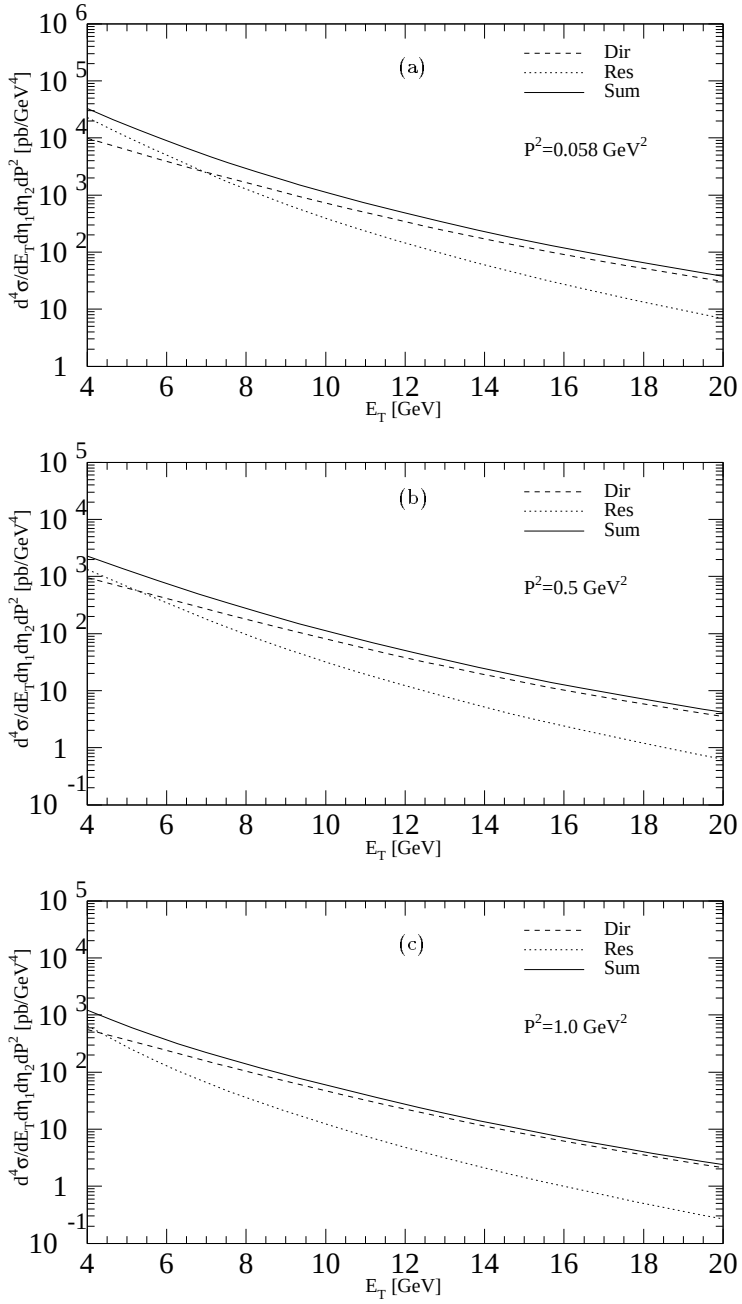

Fig. 20. (a) Dijet inclusive cross section integrated over $\eta_1, \eta_2 \in [-1.125, 1.875]$ for the virtuality $P^2 = 0.058$ GeV^2. The $\overline{\rm MS}$-GRS parametrization with $N_f = 3$ is chosen. The solid line is the sum of the direct and the resolved contribution. The dashed line is the direct-enriched contribution with $x_\gamma^{obs} > 0.75$ and the dotted curve is the resolved enriched contribution with $x_\gamma^{obs} < 0.75$; (b) $P^2 = 0.5$ GeV^2; (c) $P^2 = 1.0$ GeV^2.

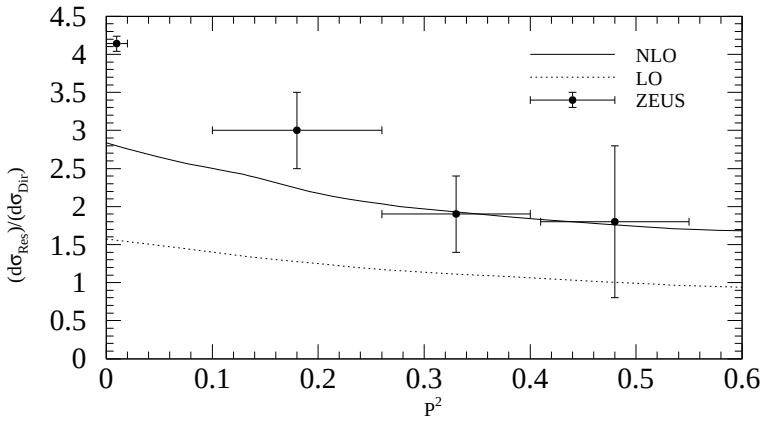

Fig. 21. The ratio of the resolved-enriched to the direct-enriched contributions as calculated in Fig. 20 a, b, c, integrated over $E_{T_1}, E_{T_2} > 4$ GeV in LO (dotted) and NLO (full) for the SaS1M parametrization with $N_f = 4$ compared with ZEUS data.

Instead, the ZEUS collaboration [23] has presented data on the ratio $r =$ Res/Dir, where Dir and Res refer to the enriched direct and resolved cross sections. The ZEUS data in [23] has actually been obtained by integrating the transverse momenta of the two-jet cross sections over the region $E_{T_1}, E_{T_2} \geq 4$ GeV and the rapidities in the range $-1.125 < \eta_1, \eta_2 < 1.875$ for various P^2-bins. With the integration cut on the transverse momenta of the two hardest jets, the transverse momentum of the unobserved jet can vanish, which is not IR safe in NLO QCD. We therefore allow the second jet to have less than 4 GeV if the third unobserved particle is soft (i.e. has a transverse momentum of less than 1 GeV) [12]. Through this procedure, a y_c dependence is avoided. We calculated the ratio r as a function of P^2 up to $P^2 = 0.6$ GeV^2 and compared it with the ZEUS [23] data in Fig. 21 in LO (dotted curve) and NLO (full curve), using the SaS1M photon PDF with $N_f = 4$ flavors. We find quite good agreement of the NLO prediction with the data points for $P^2 \geq 0.25$ GeV^2. The curve deviates from the data for $P^2 \simeq 0.2$ GeV^2, though, and even more for the point $P^2 \simeq 0$, which lies about 30% above the prediction. Surely the photoproduction data is much more precise then the other points shown in Fig. 21. For photoproduction it has been shown in [12], that the measured enriched resolved component is larger than the predicted one for a small cut in the transverse momentum. This has been attributed to additional contributions from multiple interactions with the proton remnant jet in the resolved cross section, which have not been included in the NLO calculations. This underlying event contribution is reduced for larger E_T^{min} and for cone radii smaller than 1. These problems must be present in the comparison shown here for the smallest P^2 value as well. As it seems, the underlying event contribution is also reduced by going to higher values of P^2. This could be studied more directly by measuring rapidity distributions for the

enriched resolved γ^* sample as was done for the photoproduction case [12].

6 Photon-Photon Collisions

In this section we predict inclusive jet rates for the case of photon-photon collisions in kinematic regions that will become available in LEP2 experiments. We first introduce the notation and kinematics for the hadronic cross section and then discuss some numerical results.

6.1 Jet Production Cross Section and Kinematics

To obtain a close correspondence between ep scattering discussed in the previous section and $\gamma\gamma^*$ scattering to be discussed here, we use similar notations. Thus, we deviate somewhat from the notation used in section 4. We start from electron-positron scattering for two-jet production, which may be written as

$$e^+(k_1)+e^-(k_2) \to e^+(k_1')+e^-(k_2')+\mathrm{Jet}_1(E_{T_1},\eta_1)+\mathrm{Jet}_2(E_{T_2},\eta_2)+X \quad . \tag{118}$$

We assume, that the interaction of the electrons is processed via the interaction of one quasi-real and one virtual photon, that are radiated by the electron and positron, respectively. Thus, we consider the subprocess

$$\gamma_a^*(p)+\gamma_b(q) \to \sum (\mathrm{Jet})_i + X \quad , \tag{119}$$

with $p \equiv k_1 - k_1'$ and $q \equiv k_2 - k_2'$. The electron-positron c.m. energy is given by $s_H = (k_1+k_2)^2$, whereas the $\gamma\gamma^*$ c.m. energy is given by $W^2 = (p+q)^2$. Since both, the real and the virtual photon, acquire some hadronic substructure through the resolved processes, it is not quite clear which is the probing and which is the probed photon. We therefore will not speak about target and probing photon, but simply of the real and the virtual photon. We define the virtuality of the real photon as $Q^2 \equiv -q^2$ with $Q^2 \simeq 0$ and that of the virtual photon as $P^2 \equiv -p^2$. Next, the momentum fractions of the photon in the electron and positron y_a and y_b have to be defined, which are given by

$$y_a \equiv \frac{pk_2}{k_1k_2} \qquad \text{and} \qquad y_b \equiv \frac{qk_1}{k_1k_2} \simeq \frac{E_\gamma}{E_e} \quad . \tag{120}$$

Here, E_γ is the energy of the real photon and E_e is the electron energy in the e^+e^- c.m. system.

Considering jet production, the interaction of the photons have three different parts [20, 21, 22]. First in the direct (D) contribution, both photons can interact directly, which yields the QPM box diagram in LO. The NLO QCD corrections consist of the radiation of one additional gluon in the final state and the virtual corrections. Next, the single-resolved (SR) components have to be considered, which result from the hadronic structure of either of one of the photons. Since the resolved real and the resolved virtual photon have different hadronic structures, described by different PDF's, we will specify the SR contribution of a resolved virtual photon as SR*, whereas the single resolved real photon contribution is

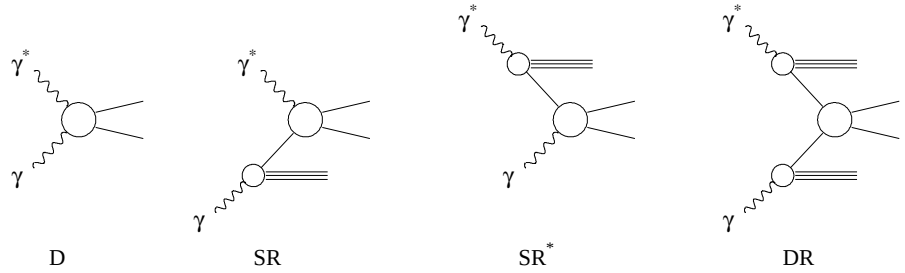

Fig. 22. The different components contributing in $\gamma\gamma^*$ scattering.

simply denoted SR. Finally, the contribution from two resolved photons is called the double-resolved (DR) contribution. The different components are pictured in Fig. 22.

The resolved photons are considered as sources for partons, which afterwards interact in a subprocess. The factorization of hard and soft regions in the e^+e^- cross section is given by

$$d\sigma(e^+e^- \to \text{jets}) = \sum_{k,l} \int dx_a dx_b \; f_{\gamma^*/l}(x_a) d\sigma_{k/l} f_{k/\gamma}(x_b) \\ df_{\gamma^*/e}(y_a) f_{\gamma/e}(y_b) dy_a dy_b \quad . \tag{121}$$

It is written as a convolution of the PDF's of the virtual and the real photons $f_{\gamma^*/l}(x_a)$ and $f_{k/\gamma}(x_b)$, respectively, with the hard partonic cross section $d\sigma_{ij}$ and the spectra of the photons, that are described by the Weizsäcker-Williams approximation. The spectrum of the real photon is integrated over the low Q^2 region from $Q^2_{min} = \frac{m_e^2 x^2}{1-x}$ to $Q^2_{max} = 4\ \text{GeV}^2$, giving

$$f_{\gamma/e}(y_b) = \frac{\alpha}{2\pi} \frac{1+(1-y_b)^2}{y_b} \ln\left(\frac{Q^2_{max}}{Q^2_{min}}\right) \quad . \tag{122}$$

The function $f_{\gamma^*/e}$ is given by equation (101). The kinematics can be described most easily in the c.m. system of the virtual photon and the electron that radiates γ_b. We start from the D case, for which from energy-momentum conservation one has

$$W = E_T(e^{-\eta_1} + e^{-\eta_2}) \quad , \tag{123}$$

$$y_a = \frac{W^2 + P^2}{s_H} \quad , \tag{124}$$

$$y_b = 1 + \frac{2W}{W^2 + P^2} E_T(\sinh\eta_1 + \sinh\eta_2) \quad . \tag{125}$$

Both variables y_a and y_b are integrated out and are included in the phase space for convenience, which gives

$$d\text{PS}^{(2)} dy_a dy_b = \frac{W^2}{W^2+P^2} \frac{E_T}{2s_H} \frac{dE_T}{(2\pi)^2} \, d\eta_1 d\eta_2 \quad . \tag{126}$$

In the SR and DR cases, the additional variables x_a and x_b have to be introduced. They give the momentum fractions of the partons in the resolved photons. We neglect the transverse momentum of the incoming virtual photon q_T as we have done in the case of electron-proton scattering, so the partons are traveling in the direction of the incoming photons. Thus the energies of the partons p_a and p_b are given by $x_a E_{\gamma^*}$ and $x_b E_\gamma$, respectively. The rapidities are boosted by

$$\eta_i' = \eta_i + \frac{1}{2}\ln(x_a x_b) \quad . \tag{127}$$

In the DR case, $x_a \neq 1$ and $x_b \neq 1$, whereas in the SR case only one of the variables x_a or x_b is less then 1.

6.2 Predictions for Inclusive Jet Rates

We now come to a presentation of numerical results for the scattering of a virtual on a real photon. First we note that the factorization and renormalization scale dependences of the D contribution is tested indirectly with the tests done in section 5.4, since the matrix elements for the D case are proportional to the abelian color class for the subprocess $\gamma g \to q\bar{q}g$ which is included in the SR case. All tests hold for each color class separately, since e.g. the cancellation and factorization of singularities holds for each color class separately. The M_γ dependence of the D and the SR* contribution compensate each other, just as for the SR and DR components, as tested in section 5.4.

For producing our plots we assume kinematical conditions that will be encountered at LEP2, where the photons are emitted by colliding electrons and positrons, both having the energy of $E_e = 83.25$ GeV. We choose the configuration, where the virtual photon travels in the positive z-direction. We focus on one-jet cross sections and do not present results on dijet rates, since the studies here have only exploratory character. For the same reason we have used only the $\overline{\text{MS}}$-GRS [36] parametrization of the photon PDF, for obtaining our results and do not consider the SaS PDF's [37]. We have implemented the PDF of GRS for both, the real and the virtual photon, since the GRS parametrization goes over into the GRV [33] parametrization for the real photon, when choosing $Q^2 = 0$. The real photon will be integrated over Q^2 using the Weizsäcker-Williams approximation for the region described before equation (122), whereas the virtual photon will have fixed P^2-values. Because of the high c.m. energies encountered at LEP2, we have set the number of flavors to $N_f = 4$, adding the contributions from photon-gluon fusion by fixed order perturbation theory. We took the value $\Lambda^{(4)}_{\overline{MS}} = 239$ MeV for the QCD scale, which is also used in the α_s two-loop formula, for which $\mu = E_T$. The factorization scales are set equal, as in the case of electron-proton scattering, with $M_\gamma = M_{\gamma^*} = E_T$. The Snowmass jet definition [67] is used as explained in section 5.

The D and SR curves presented in the following are the NLO contributions for the direct virtual photon, where the large logarithm has been subtracted and should therefore be denoted D_s and SR_s in accordance with the notation in section 5. Since we do not present curves for the unsubtracted cross sections, we suppress the index s to simplify the notation.

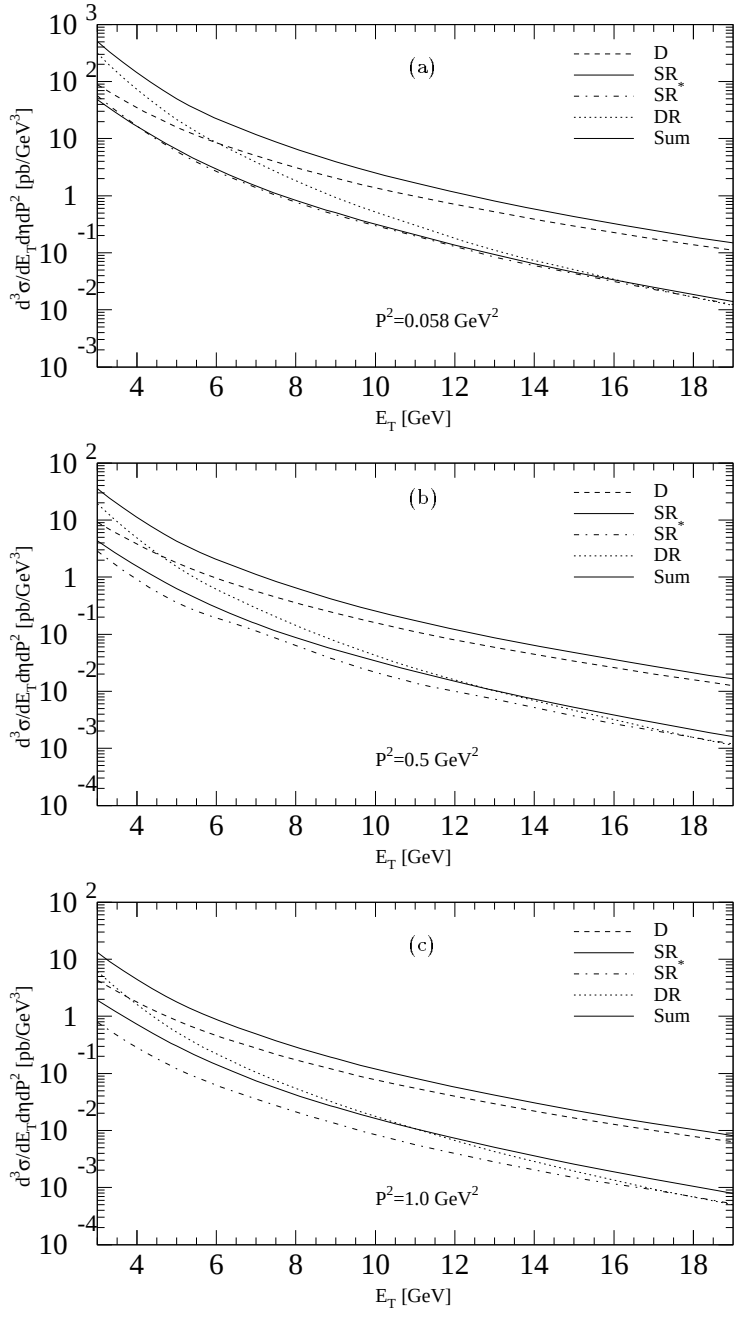

Fig. 23. (a) Single-jet inclusive cross section integrated over $\eta \in [-2, 2]$ for the virtuality $P^2 = 0.058$ GeV^2. The $\overline{\text{MS}}$-GRS parametrization with $N_f = 4$ is chosen. The upper full curve is the sum of the D, SR, SR* and the DR components; (b) $P^2 = 0.5$ GeV^2; (c) $P^2 = 1.0$ GeV^2.

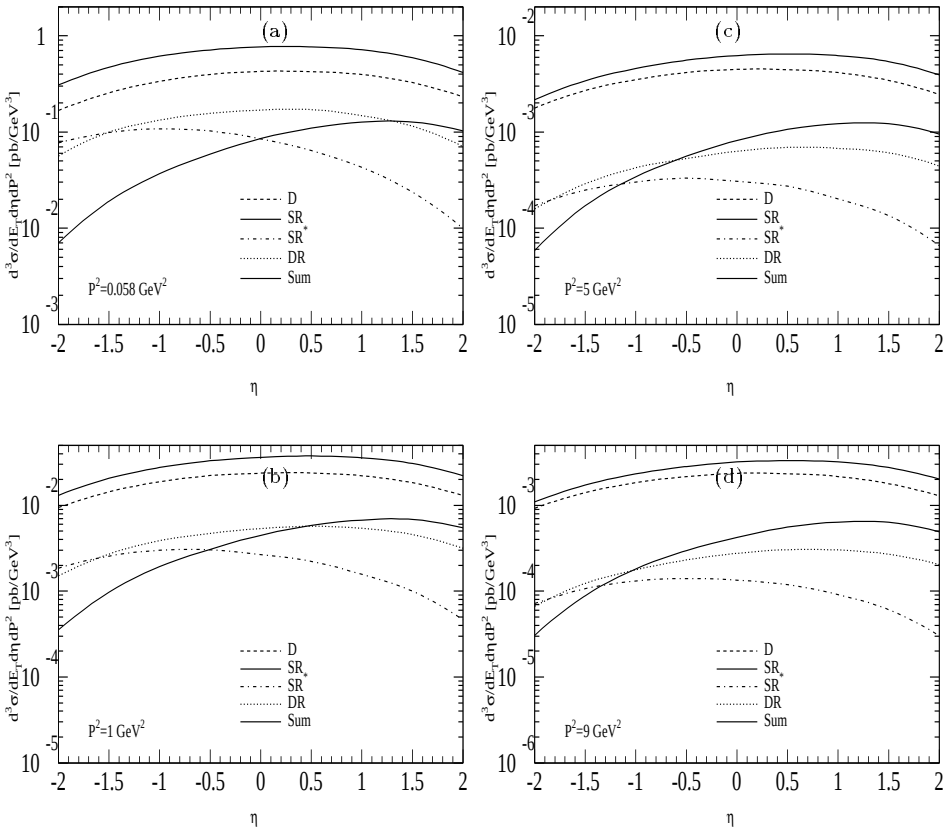

Fig. 24. (a) Single-jet inclusive cross section as a function of η for fixed $E_T = 10$ GeV and virtuality $P^2 = 0.058$ GeV^2. The $\overline{\rm MS}$-GRS parametrization with $N_f = 4$ is chosen. The upper full curve is the sum of the D, SR, SR* and the DR components; (b) $P^2 = 1$ GeV^2; (c) $P^2 = 5$ GeV^2; (d) $P^2 = 9$ GeV^2.

In Fig. 23 a, b, c the E_T spectra[1] for the virtualities $P^2 = 0.058, 0.5$ and 1.0 GeV^2 for the cross section $d^3\sigma/dE_T d\eta dP^2$ are shown, integrated over the interval $-2 \leq \eta \leq 2$, which are the boundaries being presently used at LEP1.5. As explained in section 5, the value $P^2_{eff} = 0.058$ GeV^2 is chosen as to reproduce the $P^2 \simeq 0$ case. As one can see, the SR (lower full) and SR* (dash-dotted) curves coincide in Fig. 23 a, where the real photon is approximated by the integrated Weizsäcker-Williams formula and the virtual photon has the value of P^2_{eff}. The full cross section (upper full curve) is dominated by the DR component only in the small E_T range for small P^2 values. For $P^2 = 0.5$ and 1.0 GeV^2, the DR and D contributions are of the same order around $E_T = 4$ GeV, but the DR component falls off quickly for the higher E_T's, leaving the D component as the dominant contribution. This is expected, as the resolved virtual photon

[1] I thank T. Kleinwort for the consent in using his computer program for producing the SR* and DR curves.

is important for smaller P^2 and suppressed for the larger virtualities. For the same reason, the SR* contribution falls below the SR curve when going to higher values of P^2 (remember that the resolved real photon is not suppressed by P^2). In all curves, both SR contributions do not play an important role for the full cross section. Of course, all contributions decrease with increasing P^2, so that the full cross section falls of with increasing P^2.

We turn to the η-distribution of the single-jet cross section for fixed $E_T = 10$ GeV between $-2 \leq \eta \leq 2$ for the virtualities $P^2 = 0.058, 1, 5$ and 9 GeV^2. As one sees in Fig. 24 a–d, the D and DR distributions for the lowest virtuality P^2_{eff} are almost symmetric, because of the identical energies of the incoming leptons. The SR curve falls off for negative η, whereas the SR* component is suppressed for positive η. Going to higher P^2 values, the D contribution stays more or less symmetric and dominates the full cross section, as we have already seen in Fig. 23 a, b, c for the larger E_T values. The components containing contributions from the resolved virtual photon DR and SR* fall of in the region of negative η so that they become more and more asymmetric. This is clear, since we have chosen the virtual photon to be incoming from the positive z-direction and the resolved virtual photon is falling off for higher virtualities. To observe the compensation of the $\ln(P^2/M^2_\gamma)$ term, subtracted from the direct virtual photon, with the similar but negative behavior of the resolved virtual photon, one has to compare the DR and SR, and the D and SR* components (see Fig. 22). The DR and SR contributions are of the same magnitude in the negative η region and the DR component is dominant for the larger η values, where the resolved photon is more important. We have observed these findings already for ep scattering. The same holds for the D and SR* distributions in the negative η region, only here the D component is far more dominant then the SR* one in the whole η region.

7 Summary and Outlook

We have calculated single- and dijet inclusive jet cross sections for $\gamma^* p$ and $\gamma^* \gamma$ scattering through a consistent extension of methods used in the calculation of $\gamma\gamma$ scattering and of photoproduction in ep scattering. The partonic cross sections for the considered reactions were calculated in NLO QCD using the phase-space slicing method, where a technical cut-off y_c is introduced to separate singular and finite regions of phase space. The spectrum of the real photon was approximated with the integrated, whereas the spectrum of the virtual photon was approximated by the differential Weizsäcker-Williams formula. For the resolved virtual photon contribution we used the parton distributions of the virtual photon in a LO parametrization.

For the hard cross section, we have in particular worked out the subtraction of singularities that appear when integrating the phase space over the collinear region of the virtual photon. Contrary to real photons, the singularity appearing for the virtual photon is not regulated in the dimensional regularization scheme but by the virtuality P^2 of the photon. This leads to a logarithm depending on P^2, which is absorbed into the PDF of the virtual photon. Through this procedure, the PDF becomes scheme and scale dependent. The terms remaining in the

subtracted cross section are constructed in such a way, that the corresponding real photon term is obtained in the limit $P^2 \to 0$ in the $\overline{\rm MS}$ scheme.

We have presented several tests of the numerical program [69] for the evaluation of the cross sections. We have shown, that the dependence on the slicing parameter y_c vanishes when the regulated singular and finite contributions are added. Furthermore, the factorization scale dependences of the NLO direct and the LO resolved contributions cancel to a large extend. The renormalization scale dependence was shown to be reduced in NLO compared to LO.

The jet cross sections for $\gamma^* p$ scattering were computed under HERA conditions using the Snowmass jet definition. We presented distributions in the transverse energy and rapidity of the observed jet. For very small P^2 we found good numerical agreement between real and virtual photoproduction. For the larger P^2 values, the unsubtracted direct contribution corresponding to the case of deep inelastic scattering approximates the sum of the subtracted direct and resolved contribution rather well, at least for not too large rapidities. This is in accordance with the result that the perturbatively calculable subtracted term agrees quite well with the evolved quark distributions of the virtual photon PDF in the larger x range. Differences between the unsubtracted direct and the sum of the subtracted direct and resolved components can be attributed to small differences in the subtraction term and the quark distribution and to effects from neglecting the transverse momentum of the incoming virtual photon.

Furthermore we have calculated distributions in the transverse energy for inclusive dijet cross sections. For experimental considerations the variable x_γ^{obs} has been introduced, which is used for a separation of the direct and resolved contributions. The resolved part was defined for $x_\gamma^{obs} < 0.75$, whereas the direct part was given for $x_\gamma^{obs} > 0.75$. In this way, both contributions contained non-negligible direct and resolved parts. The sum of the enriched direct and resolved curves of course showed to be independent of the value of x_γ^{obs}. As an application we have calculated the ratio of the resolved to the direct enriched cross sections, that could be compared to ZEUS data. The ratio shows significant NLO effects and is in good agreement with ZEUS data for $P^2 > 0.2$ GeV^2. For smaller virtualities the experimental data points lie above the theoretical prediction, which can be attributed to, e.g., multiple scattering between the photon and proton remnants.

The jet cross sections for $\gamma^*\gamma$ scattering were evaluated for conditions to be met at LEP2. As for ep scattering we used the Snowmass jet definition. We showed distributions in the transverse energy and the rapidity only for single inclusive cross sections with one parametrization of the virtual photon. In contrast to the ep scattering, for $\gamma^*\gamma$ scattering one additional subprocess is encountered, which is the direct interaction of the real with the virtual photon. The singularities of the real photon were regularized in the dimensional regularization scheme, whereas the virtual photon singularities have been handled as described above by subtracting the large logarithm. The direct component was shown to be the most dominant one for larger E_T. The resolved virtual photon contributions were suppressed for larger values of P^2 due to the suppression of the virtual photon PDF for larger virtualities.

Future investigations on virtual photoproduction will require more data on

single inclusive jet production at large transverse energy. A detailed dijet analysis of an infrared safe cross section such as $d^4\sigma/dE_T d\eta_1 d\eta_2 dP^2$, where the transverse energies of the two jets are not cut at exactly the same value, will provide an improved insight into the structure of the virtual photon. Furthermore, choosing a k_T-cluster-like jet definition with smaller cone radii will reduce both the uncertainties in the jet algorithm and in the underlying event. On the theoretical side, one possible improvement is the correct treatment of the transverse momentum of the incoming photon for larger P^2 including a correct transformation from the photonic c.m. frame to the HERA or LEP laboratory systems. For a consistent NLO treatment, the inclusion of NLO parton densities for the photon is necessary. These are, however, needed in a parametrized form and should also be studied in correlation with deep inelastic $e\gamma^*$ scattering data.

Acknowledgements

I thank G. Kramer for his capability to formulate clear goals for interesting research, which led to this paper. He was always supportive and helpful concerning any questions and problems I encountered during my work. Furthermore I thank the group at the II. Institute of Theoretical Physics, namely J. Binnewies, P. Büttner, M. Klasen and T. Kleinwort for a very pleasant working atmosphere. I am indebted to M. Klasen and J. Binnewies for a careful reading of this manuscript and I thank M. Klasen for his collaboration. T. Kleinwort has given me useful advice concerning details of the computer code developed during this work.

A General Definitions

To simplify the notation, we state some definitions here that will be used throughout the appendix. The Mandelstam variables s, t and u are defined in the usual way. The scale M^2 that appears in the virtual, initial and final state corrections is normally set equal to the virtuality of photon P^2, only in the photoproduction limit $P^2 \to 0$ we set $M^2 = s$. The Born terms that appear throughout this work are given by

$$T_\gamma(s,t,u) = (1-\epsilon)\left(\frac{t}{u}+\frac{u}{t}\right) - 2P^2\,\frac{s}{ut} - 2\epsilon \quad , \tag{128}$$

$$T_1(s,t,u) = 4N_C C_F\left(\frac{s^2+u^2}{t^2} - \epsilon\right) \quad , \tag{129}$$

$$T_2(s,t,u) = -8C_F(1-\epsilon)\left(\frac{s^2}{ut} - \epsilon\right) \quad , \tag{130}$$

$$T_3(s,t,u) = 4C_F(1-\epsilon)\left(\frac{2N_C C_F}{ut} - \frac{2N_C^2}{s^2}\right)(t^2+u^2-\epsilon s^2) \quad , \tag{131}$$

$$T_4(s,t,u) = 32N_C^3 C_F(1-\epsilon)^2\left(3 - \frac{ut}{s^2} - \frac{us}{t^2} - \frac{st}{u^2}\right) \quad . \tag{132}$$

For the initial state corrections the plus distribution function

$$R_+(x,z) := \left(\frac{\ln\left(x\left(\frac{1-z}{z}\right)^2\right)}{1-z} \right)_+ \tag{133}$$

is needed. As the integration over z in the initial state singularities runs from z_{min} to 1, the plus distribution function is defined as

$$R_+[g] = \int\limits_{z_{min}}^{1} dz\ R(x,z)g(z) - \int\limits_{0}^{1} dz\ R(x,z)g(1), \tag{134}$$

for any regular function $g(z)$. This leads to additional terms not given here explicitly when (134) is transformed so that both integrals are calculated in the range $[z_{min}, 1]$. The singular terms in the initial state corrections are proportional to the Altarelli-Parisi splitting functions

$$\begin{aligned}
P_{q\leftarrow\gamma}(z) &= N_C\left(1+2z(1-z)\right) \quad , & (135)\\
P_{q\leftarrow q}(z) &= C_F\left[\frac{1+z^2}{(1-z)_+} + \frac{3}{2}\delta(1-z)\right], & (136)\\
P_{g\leftarrow q}(z) &= C_F\left[\frac{1+(1-z)^2}{z}\right], & (137)\\
P_{g\leftarrow g}(z) &= 2N_C\left[\frac{1}{(1-z)_+} + \frac{1}{z} + z(1-z) - 2\right] \\
&+ \left[\frac{11}{6}N_C - \frac{N_f}{3}\right]\delta(1-z), & (138)\\
P_{q\leftarrow g}(z) &= \frac{1}{2}\left[z^2 + (1-z)^2\right]. & (139)
\end{aligned}$$

The plus functions appearing here are defined, in contrary to equation (134), in the limits $[0,1]$. In the virtual corrections the function

$$\begin{aligned}
L(x,y) &= \ln\left|\frac{x}{P^2}\right|\ln\left|\frac{y}{P^2}\right| - \ln\left|\frac{x}{P^2}\right|\ln\left|1-\frac{x}{P^2}\right| - \ln\left|\frac{y}{P^2}\right|\ln\left|1-\frac{y}{P^2}\right| \\
&- \lim_{\eta\to 0}\mathrm{Re}\left[\mathcal{L}_2\left(\frac{x}{P^2}+i\eta\right) + \mathcal{L}_2\left(\frac{y}{P^2}+i\eta\right)\right] + \frac{\pi^2}{6} \qquad (140)
\end{aligned}$$

appears [31], where $\mathcal{L}_2(x)$ is the Dilogarithm function. In the limiting case $P^2 \to 0$ one finds for $\mathcal{L}_2(x)$

$$\mathcal{L}_2\left(\frac{x}{P^2}\right) = -\frac{\pi^2}{6} - \frac{1}{2}\ln^2\left(\frac{x}{P^2}\right) \quad . \tag{141}$$

The square of the logarithm has two different values according to the sign of x:

$$\ln^2\left(\frac{x}{P^2}\right) = \begin{cases} \ln^2(-x/P^2) - \pi^2 & \text{for } x < 0 \\ \ln^2(x/P^2) & \text{for } x > 0 \end{cases} \quad . \tag{142}$$

Therefore, ones obtains the following three cases for the function $L(x,y)$ appearing in the virtual corrections of the real photon with $P^2=0$:

$$L(x,y) = \frac{\pi^2}{2} - \frac{1}{2}\ln^2\left(\frac{x}{y}\right) \quad \text{for} \quad x>0, y>0 \quad , \tag{143}$$

$$L(x,y) = \frac{3\pi^2}{2} - \frac{1}{2}\ln^2\left(\frac{x}{y}\right) \quad \text{for} \quad x<0, y<0 \quad , \tag{144}$$

$$L(x,y) = \pi^2 - \frac{1}{2}\ln^2\left(-\frac{x}{y}\right) \quad \text{for} \quad \begin{cases} x>0, y<0 \\ x<0, y>0 \end{cases} \quad . \tag{145}$$

B Virtual Corrections

In this subsection we give the explicit expressions for the virtual corrections that arise from the interference of the LO Born processes for $\gamma^*\gamma \to q\bar{q}$, $\gamma^* q \to gq$ and $\gamma^* g \to q\bar{q}$ with the corresponding one-loop amplitudes. The expressions can be found in [31]. The results depend on the two-body variables s,t and u:

$$\begin{aligned}
E_1 &= \left[-\frac{2}{\epsilon^2} + \frac{1}{\epsilon}(2\ln\frac{-u}{M^2} - 3) - \frac{\pi^2}{3} - 8 - \ln^2\frac{-u}{M^2}\right] T_\gamma(s,t,u) \\
&- 4\ln\frac{-u}{M^2}\left(\frac{2u}{s+t} + \frac{u^2}{(s+t)^2}\right) \\
&- \ln\frac{s}{M^2}\left(\frac{4u+2s}{u+t} - \frac{st}{(u+t)^2}\right) - \ln\frac{-t}{M^2}\left(\frac{4u+2t}{u+s} - \frac{st}{(u+s)^2}\right) \\
&+ 2L(-u,-s)\frac{u^2+(u+t)^2}{st} + 2L(-u,-t)\frac{u^2+(u+s)^2}{st} \\
&- \left(\frac{4u}{s+t} + \frac{u}{s+u} + \frac{u}{u+t}\right) + \left(\frac{u}{s} + \frac{u}{t} + \frac{s}{t} + \frac{t}{s}\right)
\end{aligned} \tag{146}$$

$$\begin{aligned}
E_2 &= \left[\frac{2}{\epsilon^2} + \frac{2}{\epsilon}\left(\ln\frac{-u}{M^2} - \ln\frac{s}{M^2} - \ln\frac{-t}{M^2}\right)\right] T_\gamma(s,t,u) \\
&+ \left[-\frac{\pi^2}{3} - \ln^2\frac{-u}{M^2} + \ln^2\frac{s}{M^2} + \ln^2\frac{-t}{M^2} + 2L(-s,-t)\right] T_\gamma(s,u,t) \\
&- 4\ln\frac{-u}{M^2}\left(\frac{2u}{s+t} + \frac{u^2}{(s+t)^2}\right) + \ln\frac{s}{M^2}\frac{2s}{u+t} + \ln\frac{-t}{M^2}\frac{2t}{u+s} \\
&+ 2L(-u,-s)\frac{u^2+(u+t)^2}{st} + 2L(-u,-t)\frac{u^2+(u+s)^2}{st} \\
&- 2\left(\frac{2u}{s+t} - \frac{u}{s} - \frac{u}{t} - \frac{s}{t} - \frac{t}{s}\right)
\end{aligned} \tag{147}$$

$$\begin{aligned}
E_3 &= \left[-\frac{2}{\epsilon^2} + \frac{1}{\epsilon}(2\ln\frac{s}{M^2} - 3) + \frac{2\pi^2}{3} - 8 - \ln^2\frac{s}{M^2}\right] T_\gamma(s,u,t) \\
&+ 4\ln\frac{s}{M^2}\left(\frac{2s}{u+t} + \frac{s^2}{(u+t)^2}\right) \\
&+ \ln\frac{-u}{M^2}\left(\frac{4s+2u}{s+t} - \frac{ut}{(s+t)^2}\right) + \ln\frac{-t}{M^2}\left(\frac{4s+2t}{s+u} - \frac{ut}{(s+u)^2}\right)
\end{aligned}$$

$$
\begin{aligned}
&- \quad 2L(-s,-u)\frac{s^2+(s+t)^2}{ut} - 2L(-s,-t)\frac{s^2+(s+u)^2}{ut} \\
&+ \quad \left(\frac{4s}{u+t}+\frac{s}{u+s}+\frac{s}{s+t}\right) - \left(\frac{s}{u}+\frac{s}{t}+\frac{u}{t}+\frac{t}{u}\right) \qquad (148)\\
E_4 \;&= \quad \left[\frac{2}{\epsilon^2}+\frac{2}{\epsilon}\left(\ln\frac{s}{M^2}-\ln\frac{-u}{M^2}-\ln\frac{-t}{M^2}\right)\right] T_\gamma(s,u,t) \\
&+ \quad \left[\frac{4\pi^2}{3}+\ln^2\frac{-u}{M^2}-\ln^2\frac{s}{M^2}+\ln^2\frac{-t}{M^2}+2L(-u,-t)\right] T_\gamma(s,t,u) \\
&+ \quad 4\ln\frac{s}{M^2}\left(\frac{2s}{u+t}+\frac{s^2}{(u+t)^2}\right) - \ln\frac{-u}{M^2}\frac{2u}{s+t} - \ln\frac{-t}{M^2}\frac{2t}{u+s} \\
&- \quad 2L(-s,-u)\frac{s^2+(s+t)^2}{ut} - 2L(-s,-t)\frac{s^2+(u+s)^2}{ut} \\
&+ \quad 2\left(\frac{2s}{u+t}-\frac{s}{u}-\frac{s}{t}-\frac{u}{t}-\frac{t}{u}\right) \quad . \qquad (149)
\end{aligned}
$$

C Final State Corrections

In the following we give the real final state corrections that appear when the $2 \to 3$ matrix elements are integrated over the singular region of phase space. The expressions depend on the invariant mass cut-off y_F and on the two-body variables s, t and u. Terms of order $\mathcal{O}(\epsilon)$ have been neglected. The contributions $F_2, \ldots F_5$ can be found in [31].

$$
\begin{aligned}
F_1 \;&= \quad \alpha^2\alpha_s 4 N_C C_F Q_i^4 T_\gamma(s,t,u)\left\{\frac{1}{\epsilon^2}+\frac{1}{\epsilon}\left(\frac{3}{2}-\ln\frac{s}{M^2}\right)\right. \\
&+ \quad \left.\frac{7}{2}-\frac{3}{2}\ln\frac{-y_F(t+u)}{M^2}-\ln^2\frac{-y_F(t+u)}{s}+\frac{1}{2}\ln^2\frac{s}{M^2}-\frac{\pi^2}{3}\right\} \qquad (150)\\
F_2 \;&= \quad \alpha\alpha_s^2 C_F Q_i^2 T_\gamma(t,s,u)\left\{C_F\left[\frac{1}{\epsilon^2}+\frac{1}{\epsilon}\left(\frac{3}{2}-\ln\frac{-t}{M^2}\right)\right.\right. \\
&+ \quad \left.\frac{7}{2}-\frac{3}{2}\ln\frac{-y_F(t+u)}{M^2}-\ln^2\frac{y_F(t+u)}{t}+\frac{1}{2}\ln^2\frac{-t}{M^2}-\frac{\pi^2}{3}\right] \\
&+ \quad \frac{1}{2}N_C\left[\frac{1}{\epsilon^2}-\frac{1}{\epsilon}\left(-2+\ln\frac{-st}{Q^4}+\ln\frac{-s}{t}-\frac{5}{3}\right)\right. \\
&+ \quad \ln\frac{-(t+u)}{M^2}\ln\frac{-s}{t}+\ln^2\frac{y_F(t+u)}{t}-\ln^2\frac{-y_F(t+u)}{s} \\
&- \quad \frac{1}{2}\ln^2\frac{t+u}{t}+\frac{1}{2}\ln^2\frac{-(t+u)}{s}-2\ln\frac{-y_F(t+u)}{M^2} \\
&+ \quad \ln\frac{-(t+u)}{M^2}\ln\frac{-st}{(t+u)^2}+\ln^2\frac{-(t+u)}{M^2} \\
&- \quad \ln^2\frac{y_F(t+u)}{t}-\ln^2\frac{-y_F(t+u)}{s}+\frac{1}{2}\ln^2\frac{-t-u}{s}+\frac{1}{2}\ln^2\frac{t+u}{t} \\
&- \quad \left.\left.\frac{5}{3}\ln\frac{-y_F(t+u)}{M^2}+\frac{67}{9}-\frac{2\pi^2}{3}\right]\right\} \qquad (151)
\end{aligned}
$$

$$F_3 = \alpha\alpha_s^2(N_f-1)C_F Q_i^2 T_\gamma(t,s,u)\left\{ -\frac{1}{3}\frac{1}{\epsilon} + \frac{1}{3}\ln\frac{-y_F(t+u)}{M^2} - \frac{5}{9}\right\} \quad (152)$$

$$F_4 = \alpha\alpha_s^2 C_F Q_i^2 T_\gamma(t,s,u)\left\{ -\frac{1}{3}\frac{1}{\epsilon} + \frac{1}{3}\ln\frac{-y_F(t+u)}{M^2} - \frac{5}{9}\right\} \quad (153)$$

$$\begin{aligned} F_5 = {} & \alpha\alpha_s^2 Q_i^2 T_\gamma(s,t,u)\left\{ C_F\left[\frac{1}{\epsilon^2} + \frac{1}{\epsilon}\left(\frac{3}{2} - \ln\frac{s}{M^2}\right) + \frac{7}{2} - \frac{3}{2}\ln\frac{-y_F(t+u)}{M^2}\right.\right. \\ & - \ln^2\frac{-y_F(t+u)}{s} + \frac{1}{2}\ln^2\frac{s}{M^2} - \frac{\pi^2}{3}\Big] - \frac{1}{4}N_C\left[\frac{1}{\epsilon}\ln\frac{-t}{s}\right. \\ & - \ln\frac{-(t+u)}{M^2}\ln\frac{-t}{s} + \ln^2\frac{y_F(t+u)}{t} - \ln^2\frac{-y_F(t+u)}{s} \\ & \left.\left. + \frac{1}{2}\left(\ln^2\frac{-(t+u)}{s} - \ln^2\frac{t+u}{t}\right)\right]\right\} + (t \leftrightarrow u) \end{aligned} \quad (154)$$

D Initial State Corrections for Massles Partons

Here, we state the parton initial state singularities as functions of the invariants s,t and u, the cut-off parameter y_J and the additional variable of integration z_b. Again, terms of $\mathcal{O}(\epsilon)$ have been neglect. The contributions $I_2^b, \ldots I_5^b$ can be found in [31].

$$\begin{aligned} I_1^b = {} & \alpha^2\alpha_s Q_i^4\left[-\frac{1}{\epsilon}P_{q\leftarrow\gamma}(z_b) + N_C\left\{(1-2z_b+2z_b^2)\ln\left(\frac{-(t+u)}{M^2}\frac{1-z_b}{z_b}y_I\right)\right.\right. \\ & \left.\left. + 2z_b(1-z_b)\right\}\right](1-\epsilon)C_F T_\gamma(s,t,u) \quad , \end{aligned} \quad (155)$$

$$\begin{aligned} I_2^b = {} & \alpha\alpha_s^2 Q_i^2 C_F T_\gamma(s,t,u)\left\{ C_F\left[-\frac{1}{\epsilon}\frac{1}{C_F}P_{q\leftarrow q}(z_b)\right.\right. \\ & + \delta(1-z_b)\left(\frac{1}{\epsilon^2} + \frac{1}{\epsilon}\left(-\ln\frac{-u}{M^2} + \frac{3}{2}\right) + \frac{1}{2}\ln^2\frac{-u}{M^2} + \pi^2\right) \\ & + (1-z_b)\left(1 + \ln\left(\frac{-(t+u)}{M^2}\frac{1-z_b}{z_b}y_I\right)\right) + 2R_+\left(\frac{-u}{M^2}, z_b\right) \\ & - 2\ln\left(\frac{-u}{M^2}\left(\frac{1-z_b}{z_b}\right)^2\right) - \frac{2z_b}{1-z_b}\ln\left(1 + \frac{u}{t+u}\frac{1-z_b}{y_I z_b}\right)\Big] \\ & - \frac{1}{2}N_C\left[\delta(1-z_b)\left(\frac{1}{\epsilon}\ln\frac{t}{u} + \frac{1}{2}\ln^2\frac{-u}{M^2} - \frac{1}{2}\ln^2\frac{-t}{M^2}\right) + 2R_+\left(\frac{-u}{M^2}, z_b\right)\right. \\ & - 2R_+\left(\frac{-t}{M^2}, z_b\right) - 2\ln\left(\frac{-u}{M^2}\left(\frac{1-z_b}{z_b}\right)^2\right) + 2\ln\left(\frac{-t}{M^2}\left(\frac{1-z_b}{z_b}\right)^2\right) \\ & \left.\left.\left. - \frac{2z_b}{1-z_b}\ln\left(1 + \frac{u}{t+u}\frac{1-z_b}{y_I z_b}\right) + \frac{2z_b}{1-z_b}\ln\left(1 + \frac{t}{t+u}\frac{1-z_b}{y_I z_b}\right)\right]\right\}, \end{aligned} \quad (156)$$

$$\begin{aligned} I_3^b = {} & \alpha\alpha_s^2 Q_i^2\left[-\frac{1}{\epsilon}\frac{1}{C_F}P_{g\leftarrow q}(z_b) + \frac{1}{C_F}P_{g\leftarrow q}(z_b)\ln\left(\frac{-(t+u)}{M^2}\frac{1-z_b}{z_b}y_I\right)\right. \\ & \left. - 2\frac{1-z_b}{z_b}\right]\frac{C_F}{2}T_\gamma(s,u,t), \end{aligned} \quad (157)$$

$$
\begin{aligned}
I_4^b &= (N_f-1)I_3^b, && (158)\\
I_5^b &= \alpha\alpha_s^2 Q_i^2\Bigg[-\frac{2}{\epsilon}P_{q\leftarrow g}(z_b)\\
&+ 2P_{q\leftarrow g}(z_b)\ln\left(\frac{-(t+u)}{M^2}\frac{1-z_b}{z_b}y_I\right)+1\Bigg]C_F T_\gamma(s,u,t)\\
&+ \Bigg[\frac{2}{\epsilon}\frac{1}{N_C}P_{g\leftarrow g}(z_b)+\delta(1-z_b)\Bigg(-\frac{2}{\epsilon^2}+\frac{1}{\epsilon}\left(\ln\frac{tu}{Q^4}-\frac{11}{3}+\frac{2N_f}{3N_C}\right)-2\pi^2\\
&- \frac{1}{2}\ln^2\frac{-u}{M^2}-\frac{1}{2}\ln^2\frac{-t}{M^2}\Bigg)-2R_+\left(\frac{-u}{M^2},z_b\right)-2R_+\left(\frac{-t}{M^2},z_b\right)\\
&+ 2\ln\left(\frac{-u}{M^2}\left(\frac{1-z_b}{z_b}\right)^2\right)+2\ln\left(\frac{-t}{M^2}\left(\frac{1-z_b}{z_b}\right)^2\right)\\
&+ \frac{2z_b}{1-z_b}\ln\left(1+\frac{u}{t+u}\frac{1-z_b}{y_I z_b}\right)+\frac{2z_b}{1-z_b}\ln\left(1+\frac{t}{t+u}\frac{1-z_b}{y_I z_b}\right)\\
&- 4(1+z_b^2)\frac{1-z_b}{z_b}\ln\left(\frac{-(t+u)}{M^2}\frac{1-z_b}{z_b}y_I\right)\Bigg]\left(-\frac{N_C}{4}\right)T_\gamma(s,t,u). && (159)
\end{aligned}
$$

E Initial State Corrections for the Virtual Photon

A virtual photon can decay into a $q\bar{q}$-pair. After the integration over the collinear region of phase space the Born matrix elements factorize. There are three types of Born matrix elements, namely the processes $qq' \to qq'$ (denoted by T_1), $qq \to qq$ (denoted by T_1 and T_2) and $q\bar{q} \to gg$ (denoted by T_3). The divergence is regularized by the virtuality of the photon P^2. The corrections depend on the two-body variables s, t and u, on the cut-off parameter y_J and on the additional variable of integration z_a.

$$
\begin{aligned}
I_1^a &= -2\alpha^2\alpha_s Q_i^4 M\Big[T_\gamma(t,s,u)+T_\gamma(u,s,t)\Big]\,, && (160)\\
I_2^a &= 2C_F\alpha\alpha_s^2 Q_i^2 M T_1(s,t,u)\,, && (161)\\
I_3^a &= -2\alpha\alpha_s^2 Q_i^2 M\Big[T_1(t,s,u)+T_1(u,s,t)\Big]\,, && (162)\\
I_4^a &= 4C_F\alpha\alpha_s^2 Q_i^2 M\Big[T_2(s,t,u)+T_2(t,s,u)\\
&+ \tfrac{1}{2}(T_3(s,t,u)+\text{zycl. permutations in } s,t,u)\Big]\,, && (163)\\
I_5^a &= 2C_F\alpha\alpha_s^2 Q_i^2 M\Big[T_3(s,t,u)+\text{zycl. permutations in } s,t,u\Big]\,, && (164)
\end{aligned}
$$

where

$$
M=\frac{1}{2N_C}P_{q\leftarrow\gamma}(z_a)\ln\left(1+\frac{y_J s}{z_a P^2}\right)\quad . \qquad (165)
$$

References

1. J.D. Bjorken and E.A. Paschos, Phys. Rev. 185 (1969) 1975; R.P. Feynman, Phys. Rev. Lett. 23 (1969) 1415; *Photon-Hadron Interactions* (Benjamin, New York, 1972).
2. H. Fritzsch, M. Gell-Mann, Proc. XVI Int. Conf. on High Energy Physics, eds. J.D. Jackson et al. (Chicago 1972).
3. D.J. Gross, F. Wilczek, Phys. Rev. Lett. 30 (1973) 1343;
   H.D. Politzer, Phys. Rev. Lett. 30 (1973) 1346.
4. J.C. Collins, D.E. Soper and G. Sterman in A.H. Mueller, ed., *Perturbative Quantum Chromodynamics* (World Scientific, 1989).
5. J.C. Collins and D.E. Soper, Ann. Rev. Nucl. Part. Sci. 37 (1987) 383.
6. I. Abt et al., H1 Collaboration, Phys. Lett. B314 (1993) 436; T. Ahmed et al., H1 Collaboration, Phys. Lett. B297 (1992) 205; Phys. Lett. B299 (1993) 37; S. Aid et al., H1 Collaboration, Z. Phys. C70 (1996) 17.
7. M. Derrik et al., ZEUS Collaboration, Phys. Lett. B297 (1992) 404; Phys. Lett. B322 (1994) 287; Phys. Lett B342 (1995) 417; Phys. Lett. B348 (1995) 665.
8. C.F.v. Weizsäcker, Z. Phys. 88 (1934) 612; E.J. Williams, Phys. Rev. 45 (1934) 729.
9. For a reviews see: A. Vogt, Proceedings of the Workshop on Two-Photon Physics at LEP and HERA, Lund, May 1994, eds. G. Jarlskog and L. Jönssen (Lund Univ., 1994) p. 141; T. Sjöstrand, J.K. Storrow, A. Vogt, J. Phys. G: Nucl. Part. Phys. 22 (1996) 893.
10. H. Abramowicz, Proceedings of the International Conference on High Energy Physics, Warsaw 1996 (and references therein).
11. M. Klasen, G. Kramer, Phys. Lett. B366 (1996) 385.
12. M. Klasen, G. Kramer, Z. Phys. C76 (1997) 67.
13. M. Klasen, G. Kramer, T. Kleinwort, Eur. Phys. J. direct C1 (1998) 1.
14. M. Klasen, G. Kramer, Z. Phys. C72 (1996) 107.
15. D. Bödeker, G. Kramer, S.G. Salesch, Z. Phys. C63 (1994) 471.
16. D. Bödeker, Phys. Lett. B 292 (1992) 164; Z. Phys. C59 (1993) 341.
17. M. Drees, R.M. Godbole, Nucl. Phys. B339 (1990) 355.
18. D. Buskulic et al., ALEPH Collaboration, Phys. Lett. B313 (1993) 509; R. Akers et al., OPAL Collaboration, Z. Phys. C61 (1994) 248; P. Abreu et al., DELPHI Collaboration, Z. Phys. C 62 (1994) 357.
19. H. Hayashii et al., TOPAZ Collaboration, Phys. Lett. B314 (1993) 149; B.J. Kim et al., AMY Collaboration, Phys. Lett. B325 (1994) 248.
20. T. Kleinwort, G. Kramer, Phys. Lett. B370 (1996) 141; Nucl. Phys. B477 (1996) 3.
21. T. Kleinwort, G. Kramer, Z. Phys. C75 (1997) 489.
22. T. Kleinwort, DESY 96-195, September 1996, PhD thesis.
23. N. Macdonald (ZEUS Collab.), talk at the HERAMC Workshop, WG 30, October 1998; C. Foudas (ZEUS Collab.), talk given at the Int. Conf. on QCD, Montpellier, France, July 1998.
24. C. Adloff et al., H1 Collab., Phys. Lett B415 (1997) 418; DESY 98-076 (June 1998) hep-ex/9806029, Eur. Phys. J (submitted)
25. Ch. Berger et al., PLUTO Collaboration, Phys. Lett. B142 (1984) 119.
26. M. Klasen, G. Kramer, B. Pötter, Eur. Phys. J. C1 (1998) 261.
27. M. Glück, E. Reya, M. Stratmann, Phys. Rev. D54 (1996) 5515.
28. D. de Florian, C. Garcia Canal, R. Sassot, Z. Phys. C75 (1997) 265.

29. J. Chyla, J. Cvach, proceeding of the Workshop 1995/96 on "Future Physics at HERA", eds. G. Ingelman, A. de Roeck, R. Klanner, DESY 1996, Vol. 1, p. 545.
30. Report on "$\gamma\gamma$ Physics", conveners P. Aurenche and G.A. Schuler, to appear in the proceedings of the 1995 LEP2 Physics workshop, hep-ph/96101317.
31. D. Graudenz, Phys. Rev, D19 (1994) 3291, Phys. Lett. B 256 (1992) 518
32. T. Brodkorb, E. Mirkes, Z. Phys. C66 (1995) 141.
33. M. Glück, E. Reya, A. Vogt, Phys. Rev. D46 (1992) 1973; Phys. Rev. D45 (1992) 3986.
34. L.E. Gordon, J.K. Storrow, Z. Phys. C56 (1992) 307.
35. P. Aurenche, M. Fontannaz, J.-Ph. Guilett, Z. Phys. C64 (1994) 621.
36. M. Glück, E. Reya, M. Stratmann, Phys. Rev. D51 (1995) 3220.
37. G.A. Schuler, T. Sjöstrand, Z. Phys. C68 (1995) 607; Phys. Lett. B 376 (1996) 193.
38. G. 't Hooft and M. Veltmann, Nucl. Phys. **B44** (1972) 189;
C.G. Bollini and J.J Giambiagi, Nuovo Cim. **12B** (1972) 20.
39. W.J. Marciano, Phys. Rev. **D12** (1975) 3861.
40. G. Sterman et.al., Rev. Mod. Phys. 67 (1995) 1.
41. M. Diemoz, F. Ferroni, E. Longo, G. Martinelli, Z. Phys. C39 (1988) 21.
42. G. 't Hooft, Nucl. Phys. B61 (1973) 455; W.A. Bardeen, A.J. Buras, D.W. Duke, T. Muta, Phys. Rev. D18 (1978) 3998.
43. V.N. Gribov, L.N. Lipatov, Sov. J. Nucl. Phys. 15 (1972) 438, 675.
44. Y.L. Dokshitzer, Sov. Phys. JETP 46 (1977) 641.
45. G. Altarelli and G. Parisi, Nucl. Phys. B126 (1977) 298.
46. E. Witten, Nucl. Phys. B120 (1977) 189.
47. W.A. Bardeen, A.J. Buras, Phys. Rev. D20 (1979) 166; Erratum D21 (1980) 2041.
48. R.K. Ellis, M.A. Furman, H.E. Faber, I. Hincliffe, Nucl. Phys. B173 (1980) 397.
49. R.K. Ellis, J.C. Sexton, Nucl. Phys. B269 (1986) 445.
50. G. Kramer, Springer Tracts in Mod. Phys., Vol. 102, Springer, Berlin (1984).
51. R.D. Field, *Applications of Perturbative QCD* (Addison-Wesley, 1980).
52. E. Byckling, K. Kajantie, *Particle Kinematics* (Jon Wiley, 1972).
53. R.K. Ellis, D. Ross, A.E. Terrano, Nucl. Phys. B178 (1981) 421.
54. K. Fabricius, G. Kramer, I. Schmitt, G. Schierholz, Z. Phys. C11 (1982) 315.
55. B.L. Ioffe, Phys. Lett. 30 (1969) 123.
56. A. Levy, TAUP-2349-96, hep-ex/9608009
57. J.J. Sakurai, Ann. Phys. 11 (1960) 1.
58. A. Levy, TAUP 2398-96, December 1996, lectures given in Kloster Banz, October 1995.
59. T.F. Walsh, P. Zerwas, Nucl. Phys. B41 (1972) 551; Phys. Lett. B44 (1973) 195.
60. T. Uematsu, T.F. Walsh, Phys. Lett. B101 (1981) 263; Nucl. Phys. B199 (1982) 93.
61. G. Rossi, Phys. Rev. D29 (1984) 852.
62. M. Glück, E. Reya, Phys. Rev. D28 (1983) 2749.
63. F.M. Borzumati, G.A. Schuler, Z. Phys. C58 (1993) 139.
64. A.C. Hearn, REDUCE User's Manual, Version 3.4, RAND Publication CP78 (1991).
65. S.D. Ellis, Z. Kunszt, D.E. Soper, Phys. Rev. Lett. 62 (1989) 726.
66. G. Sterman, S. Weinberg, Phys. Rev. Lett. 39 (1977) 1436.
67. J.E. Huth et al., Proc. of the 1990 DPF Summer Study on High Energy Physics, Snowmass, Colorado, edited by E.L. Berger, World Scientific, Singapore, 1992, p. 134.
68. H.L. Lai et al., CTEQ Collaboration, Phys. Rev. D51 (1995) 4763.
69. B. Pötter, Comp. Phys. Comm. 119 (1999) 45.